An Improved Measurement of the Inclusive Rate for Charmless Semileptonic Decays of B Mesons

A THESIS

PRESENTED TO THE FACULTY OF THE GRADUATE SCHOOL

OF THE UNIVERSITY OF MINNESOTA

BY

Stefan Alan Anderson

IN PARTIAL FULFILLMENT OF THE REQUIREMENTS

FOR THE DEGREE OF

DOCTOR OF PHILOSOPHY

Ronald A. Poling, Advisor

May 2002

An Improved Measurement of the Inclusive Rate for Charmless Semileptonic Decays of B Mesons

by Stefan Alan Anderson

Under the supervision of Professor Ronald A. Poling

ABSTRACT

We report the results of a study of charmless semileptonic B-meson decays made with a sample of 9.7 million $B\bar{B}$ events collected with the CLEO II and II.V detectors. An excess of $1901 \pm 122 \pm 256$ leptons in the momentum interval $2.2 - 2.6$ GeV/c is attributed to $B \to X_u \ell \nu$. To interpret this result, we use CLEO data on $B \to X_s \gamma$ and theoretical analyses based on Heavy Quark Theory to determine the fraction of $B \to X_u \ell \nu$ decays in our measured momentum interval. Combining these results with theoretical expressions for the $B \to X_u \ell \nu$ decay rate leads to a measurement of the CKM parameter $|V_{ub}|$ of $(4.08 \pm 0.34 \pm 0.44 \pm 0.24 \pm 0.16) \times 10^{-3}$, where the first two errors are experimental and the last two are from theory.

To my family.

ACKNOWLEDGEMENTS

The data used in preparing this thesis resulted from the efforts of hundreds of people. I met many wonderful individuals during my years in the CLEO collaboration. I was deeply impressed by the energy and creativity with which they overcame the many challenges of high energy physics experimentation.

A few people deserve special recognition here. Foremost among these is my thesis advisor Ron Poling. He introduced me to CLEO, and throughout the years he guided my work with patience, enthusiasm, and a great sense of humor. The energy and intellect with which he finds solutions to problems are inspirational. I hope that I can be as effective as he is in my future endeavors.

Yuichi Kubota supervised much of my work on the CLEO III RICH gas system and provided useful observations regarding most of my other projects. He has a remarkable ability to quickly distill any experimental problem to its essence. Ed Thorndike's visits to the Minnesota office provided inspiration and motivation.

The Minnesota postdocs that I worked with were both role models and great friends. They showed me how to have fun while working hard. Alex Smith was a great mentor during my work on the RICH gas system. Working with him as he conceptualized, prototyped, and completed this complicated project was an education in itself. John O'Neill provided a great deal of help with pass2 and analysis code. Any good coding habits that I have were probably learned while mimicking his work.

Valery Frolov was always willing to discuss a problem, and I came away from our conversations with many new insights.

My frequent trips to Syracuse were made bearable by the terrific RICH crew there. It was great fun to work with Sacha Kopp, Ray Mountain, and Georg Viehhauser. I thank Adam Lyon for many useful discussions and figures.

Of course, I obtained a great deal of support from my fellow graduate students. I'd like to thank Sang Joon Lee for being such a terrific office mate through the years. He never failed to show concern when things got stressful. Similarly, Tim Riehle encouraged me with the load was heavy, and his wry sense of humor was much missed after he moved on. Craig Prescott's constant presence during my first year at Wilson Lab was a great comfort. He was (literally) always just across the hall and could enjoy the humor in any situation. During an intense final year, Véronique Boisvert provided encouragement and advice. Jana and Gregg Thayer helped me prepare my all-important job talk. I thank Chris Stepaniak and Pete Zweber both for getting me away from work when necessary. I will miss the weekly poker parties. Selina Li was always ready with a cookie when one was needed.

Bobbi Eich extracted me from innumerable bureaucratic pitfalls in the physics department and graduate school. Maureen Long provided valuable help with travel considerations and thesis-defense arrangements. She and Alexander Scott came through with transparencies in a pinch.

My good friend Jon Sorbie was always happy to provide transportation and a place to sleep, regardless of the lengths of the intervals between my calls. Koreen Wallis did not hesitate to step into a difficult situation and help me and my family

when we were in need. I will always be grateful. Desirée Snyder got me to jump the gate and brave the gorge when the water was at its highest. I thank her for her courage. The Snyder and Jackson families were quick to take me in and made Central New York feel like home.

And, most importantly, my family continues to support me with their love.

TABLE OF CONTENTS

LIST OF TABLES

LIST OF FIGURES

CHAPTER 1

Introduction

Our understanding of the structure and behavior of matter has seen tremendous change in the last century. Around one hundred years ago, physicists demonstrated that ordinary matter is made of atoms. Each atom consists of an electrically charged nucleus surrounded by oppositely charged electrons. With the discovery of the electrically neutral neutron in 1932, it became apparent that the nucleus is really a bundle of neutrons and charged protons.

In the 1930's, physicists studying particles produced by cosmic-ray interactions in the upper atmosphere discovered particles not found in ordinary matter. The development of accelerators led to the discovery of many more particles in subsequent decades. These particles included the lepton (the electron and its close relatives), and the hadrons (protons, neutrons, pi mesons and many more). Physicists naturally wondered whether they were seeing matter's most fundamental components.

A model emerged in the 1960's in which most of the observed particles were constructed from more fundamental objects known as quarks. Experimental evidence for quarks became persuasive in the 1970's, and the "Standard Model" has incorporated the quarks and leptons in a framework that successfully describes many phenomena. It has been subjected to intense experimental testing ever since.

The interactions studied in this thesis involve the unstable hadrons called mesons. Mesons are combinations of one quark and one antiquark, bound together by the strong force (the same force which binds nuclei together). Mesons can decay via processes known as flavor-changing weak decays. In such decays, one quark within the meson can decay into a lighter quark, leaving a different quark-antiquark pair and additional particles formed from the energy released in the decay. The rate at which a particular meson, the B meson, decays in this fashion can be related to some of the Standard Model's fundamental parameters.

The heavy quarks in B mesons are known as bottom quarks. They can decay directly into two types of lighter quarks, the relatively heavy charm quark, and the much lighter up quark. B meson decays in which the bottom quark goes to an up quark are quite rare. While they have been observed, there is a great need for more precise measurements of their characteristics. The subject of this thesis is a new study of these bottom-quark decays that has been made with the CLEO II experiment.

1.1 The Standard Model

In the Standard Model[1] all matter is constructed from a set of fundamental particles. All but one of these particles can be classified into three groups: quarks, leptons, and mediators. The remaining particle, the Higgs boson, plays a special role in the model. Forces in the physical world are modeled as the exchange of mediators between

[1]The introduction to the Standard Model presented here is necessarily incomplete. Many excellent introductory texts on the subject are available, including those listed in Refs. [1] and [2].

members of the quark and lepton families.

Like the quarks, the leptons come in six varieties, three of which have electric charge. The lightest charged lepton is the familiar electron. It is denoted by the symbol e^- or simply e. Like all other charged fundamental particles, electrons have antiparticles that have the same mass but opposite charge. These are known as positrons and have the symbol e^+ or $\bar{e}$. Unless stated otherwise, particles and their antiparticles will be indicated by the same symbol in the remainder of this thesis. Electrons and positrons will therefore both be represented by the symbol e.

Table 1.1 lists all six leptons, along with their charges and masses [3]. The muon (μ) and the tau (τ) are more massive versions of the electron. They are unstable particles and are therefore not normally found in ordinary matter. Each charged lepton has an associated neutrino, labeled ν_e, ν_μ and ν_τ. Neutrinos are electrically neutral particles, and the Standard Model treats them as having no mass. There is growing evidence that they are massive particles, but direct measurements thus far have only been able to place upper limits on the values of their masses. All of the leptons have intrinsic angular momenta of $\frac{1}{2}\hbar$, and are therefore fermions.

Quarks come in six "flavors": up, down, charm, strange, top, and bottom. They are all fermions. Some of their properties are listed in Table 1.2. Quarks are never observed on their own but come in two types of bundles: quark-antiquark pairs (mesons), and triplets of quarks or anti-quarks (baryons), which together constitute the hadrons. (The top quark seems to be too short-lived to form such combinations before decaying.) The complicated strong interactions that take place inside hadrons make it difficult to define and measure the quarks' masses, especially those of the

Table 1.1: The six types of leptons. Their charges are listed in units of the magnitude of the electron charge ($e = 1.602 \times 10^{-19}$ Coulombs). Their masses are in units of MeV/c^2 (931 MeV/c^2 = 1 atomic mass unit).

Lepton	Symbol	Charge	Mass
		$Q/\|e\|$	MeV/c^2
Electron	e^-	-1	0.511
Muon	μ^-	-1	105.7
Tau	τ^-	-1	1777
Electon Neutrino	ν_e	0	$< 3 \times 10^{-6}$
Muon Neutrino	ν_μ	0	< 0.19
Tau Neutrino	ν_τ	0	< 18.2

Table 1.2: The six types of quarks. The masses listed are approximate.

Quark	Symbol	Charge	Mass
		$Q/\|e\|$	MeV/c^2
Down	d	-1/3	3
Up	u	+2/3	6
Strange	s	-1/3	120
Charm	c	+2/3	1,250
Bottom	b	-1/3	4,800
Top	t	+2/3	174,000

lighter quarks. Despite its very short lifetime, and the difficulty of producing and studying it, the very large mass of the top quark is known with the smallest fractional uncertainty of all the quarks' masses.

There are four forces in the physical world: gravity, electromagnetism, the weak force, and the strong force. Gravity is the weakest of these. It does not influence the subatomic particles discussed in this thesis, and is not included in the Standard Model. The forces are modeled as the exchange of different types of particles known as gauge bosons. There are five such particles in the Standard Model, and all have integer spins. Some of their properties are listed in Table 1.3.

The electromagnetic force is responsible for binding electrons and nuclei into atoms. It involves the exchange of massless photons between electrically charged particles. This sector of the Standard Model, known as Quantum Electrodynamics

Table 1.3: The gauge bosons. The masses of the W and Z bosons have been determined experimentally.

Force	Boson	Symbol	Charge $Q/\|e\|$	Mass MeV/c^2
Electromagnetic	Photon	γ	0	0
Weak	W Bosons	$W^{\pm}$	± 1	80.42
Weak	Z Boson	Z^0	0	91.19
Strong	Gluon	g	0	0

(QED), has been well tested by high-precision experiments.

The weak interaction was first observed in nuclear decay. It involves all of the quarks and leptons, including the neutrinos. It has three mediators: the W^+, W^- and Z^0. All are massive, and this means that the weak interaction has the shortest range of all interactions. Interactions mediated by the charged W bosons necessarily involve changes in particles' identities. These can lead to spontaneous decays like the process $\mu^- \rightarrow e^- \bar{\nu}_e \nu_\mu$. Such processes are known as "charged-current" interactions.

The strong force involves the exchange of gluons between particles possessing "color charge." Color charge has nothing to do with usual property of color, but rather is analogous to electric charge. It is only carried by quarks and gluons. Since they have no color charge, the leptons are unaffected by the strong force. Quarks can have one of three colors, arbitrarily denoted red (r), green (g) or blue (b). Antiquarks carry anticolor charges: $\bar{r}$, $\bar{g}$ or $\bar{b}$. Quantum chromodynamics (QCD), the theory of

the strong force, requires that the combinations of quarks and gluons found in nature have no net color charge. This is known as "color confinement," and explains why quarks are found only in mesons and baryons. In a meson, the quark's color cancels the antiquark's anticolor. In a baryon, the three quarks (or antiquarks) include one of each color (or anticolor), again giving a combination of that is "color neutral."

Another important feature of QCD is "asymptotic freedom." The coupling, or strength of the interaction, decreases as the momentum transferred increases. At infinite momentum transfer the interaction vanishes. This allows perturbative calculations for processes involving large momentum transfers. Unfortunately, the growth of the strength of the coupling at lower momenta makes QCD-based calculations difficult for many processes.

Evidence for all of the quarks, leptons, and mediators has been observed experimentally. A remaining particle, the Higgs boson, has yet to be discovered. It is widely believed to exist and major experimental efforts are underway to observe it. It is of central importance to the mechanism that gives quarks, leptons, and the W and Z bosons mass in the Standard Model.

This thesis describes measurements of B-meson decays. The specific B mesons studied consist of a heavy b quark paired with a light u or d quark: $B^- = b\bar{u}$, $B^+ = \bar{b}u$, $\bar{B}^0 = b\bar{d}$, and $B^0 = \bar{b}d$. While the decays of interest are primarily charged-current weak processes, it is necessary to deal with low-energy (nonperturbative) strong-interaction effects to interpret the measurements.

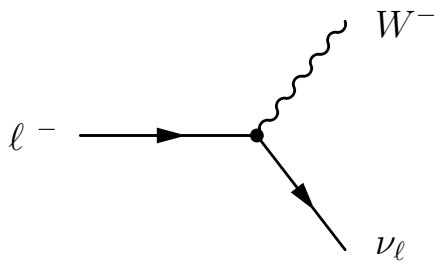

Figure 1.1: A weak vertex involving leptons.

1.2 Weak Interactions

1.2.1 Charged-Current Interactions

The Feynman diagram for the W-mediated decay of an unstable lepton is shown in Fig. 1.1. Here an electron, muon, or tau is converted to its associated neutrino and a W^- is produced. Note that these couplings group the leptons into "generations." That is, only leptons and their associated neutrinos couple to charged Ws. For example, a vertex coupling an electron and a tau neutrino to a W^- is not allowed in the Standard Model. This is often represented schematically with the following notation:

$$\begin{pmatrix} e \\ \nu_e \end{pmatrix}, \begin{pmatrix} \mu \\ \nu_\mu \end{pmatrix}, \begin{pmatrix} \tau \\ \nu_\tau \end{pmatrix}. \tag{1.1}$$

Similarly, quarks also couple to W bosons. One such coupling is represented in Fig. 1.2. Here a u quark is converted to a d quark, giving off a W^+ in the process. Charged quark currents differ from those for leptons in that the Ws couple to *mixtures*

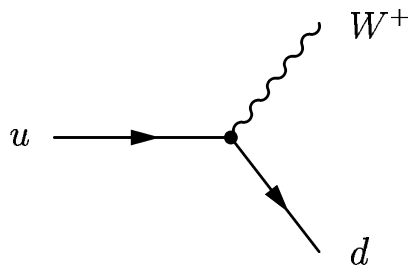

Figure 1.2: A weak vertex involving quarks.

of the quark mass eigenstates. The convention for introducing this into the Standard Model is to rotate the down-type quarks into a new basis using a 3×3 matrix:

$$\begin{pmatrix} d' \\ s' \\ b' \end{pmatrix} = \begin{pmatrix} V_{ud} & V_{us} & V_{ub} \\ V_{cd} & V_{cs} & V_{cb} \\ V_{td} & V_{ts} & V_{tb} \end{pmatrix} \begin{pmatrix} d \\ s \\ b \end{pmatrix}. \tag{1.2}$$

The matrix in Eq. 1.2 is known as the Cabbibo-Kobayashi-Maskawa (CKM) matrix [4]. The elements of the CKM matrix are among the Standard Model's fundamental input parameters. Current experimental limits on their magnitudes are as follows [3]:

$$\begin{pmatrix} 0.9742 - 0.9757 & 0.219 - 0.226 & 0.002 - 0.005 \\ 0.219 - 0.225 & 0.9734 - 0.9749 & 0.037 - 0.043 \\ 0.004 - 0.014 & 0.035 - 0.043 & 0.9990 - 0.9993 \end{pmatrix}. \tag{1.3}$$

Ws couple to the rotated quark states in a manner exactly analogous to the lepton

pairs in Eq. 1.1:

$$\begin{pmatrix} u \\ d' \end{pmatrix}, \begin{pmatrix} c \\ s' \end{pmatrix}, \begin{pmatrix} t \\ b' \end{pmatrix}. \tag{1.4}$$

This means that, unlike the leptons, the physical quarks are not strictly grouped into generations[2]. Weak interactions favor certain transitions over others, however, and this fact is reflected in the relative sizes of the magnitudes of the elements in the CKM matrix. The diagonal elements all have magnitudes near one, and these correspond to the favored transitions between the quark pairs: u to d, c to s, and t to b. Off-diagonal elements are smaller and correspond to suppressed transitions.

B mesons decay via charged-current weak interactions. They are especially interesting because energy conservation forbids the CKM-favored $b \to t$ transition, leaving the b with a "choice" of decaying by $b \to c$ or $b \to u$. These decays therefore probe the off-diagonal elements V_{cb} and V_{ub}. The analysis described here is aimed at observing $b \to u$ transitions and improving the measurement of the magnitude of smallest CKM element, V_{ub}.

1.2.2 CP Violation

One can imagine viewing a given physical process in a mirror. The operation of replacing a process with its mirror image is known as "parity" (P). It was long assumed that parity is a symmetry operation. That is, if a process is allowed, then its "mirror

[2]Actually, recent observations involving atmospheric and solar neutrinos strongly suggest that oscillations between the different types of neutrinos occur [5, 6]. The details are still being sorted out, but these results suggest that the Standard Model needs modification.

image" is also allowed. However, it was discovered in 1956 [7] that this operation is not a symmetry of the weak interaction. This can be seen in the decay

$$\pi^+ \rightarrow \mu^+ \nu_\mu. \tag{1.5}$$

In this decay, the muon neutrino is always produced with its intrinsic angular momentum (spin) directed against its direction of motion (that is, it is always "left-handed"). The mirror image of this process, in which the neutrino's spin is aligned with its momentum, is never observed, therefore this weak interaction is parity non-conserving.

Another operation that can be applied to physical interactions is charge conjugation (C), which transforms particles into their antiparticles. Weak interactions also violate C. For example, the charge conjugate of decay (1.5) would be

$$\pi^- \rightarrow \mu^- \bar{\nu}_\mu, \tag{1.6}$$

where the $\bar{\nu}_\mu$ is left-handed. Since only right-handed antineutrinos seem to exist in nature, this weak interaction is charge conjugation non-conserving.

Note that if we perform the combined operation CP on the reaction $\pi^+ \rightarrow \mu^+ \nu_\mu$, the result is $\pi^- \rightarrow \mu^- \bar{\nu}_\mu$, with a right-handed antineutrino. This process is allowed, so the decay is CP conserving.

In 1964 CP violation was observed in certain decays of neutral kaons [8]. Later, it was observed that CP violation could be included in the Standard Model by adding a third generation of quarks. This was, in fact, the motivation for introducing the 3 $\times$ 3 CKM matrix, in which elements are allowed to be complex [4]. This mechanism also predicts observable CP violation in the neutral B system, and this effect has recently been measured experimentally [9, 10].

In general, all nine elements of the CKM matrix in Eq. 1.2 can be complex numbers which, if they were all independent, would require 18 parameters to specify. In the Standard Model the matrix is constrained to be unitary ($V^\dagger V = 1$), so that there are only 9 independent parameters. Five of these can be removed by redefining the complex phases of the the quark fields that accompany the matrix in the weak-interaction Lagrangian. This leaves four independent parameters in the CKM matrix, only one of which is a complex phase. This is reflected in the popular Wolfenstein parameterization [11]:

$$V = \begin{pmatrix} 1-\lambda^2/2 & \lambda & A\lambda^3(\rho - i\eta) \\ -\lambda & 1-\lambda^2/2 & A\lambda^2 \\ A\lambda^3(1-\rho-i\eta) & -A\lambda^2 & 1 \end{pmatrix} + \mathcal{O}(\lambda^4). \tag{1.7}$$

Here A, λ, ρ, and η are the matrix's four independent parameters. A and the quantity $\rho^2 + \eta^2$ are of order unity, while $\lambda \simeq 0.22$. Terms of order $\lambda^4 \approx 10^{-3}$ and smaller are excluded from this form. To this level of approximation, only the far off-diagonal terms are complex. This means that for this Standard Model description of a CP-violating weak interaction to work, the CKM matrix element V_{ub} must be nonzero.

Applying the unitarity condition to the first and third columns in Eq. 1.2 gives the relation

$$V_{ud}{V_{ub}}^* + V_{cd}{V_{cb}}^* + V_{td}{V_{tb}}^* = 0. \tag{1.8}$$

Given that $V_{ud} \simeq V_{tb} \simeq 1$ and $V_{cd} < 0$, this can be recast as

$$\frac{{V_{ub}}^*}{|V_{cd}V_{cb}^*|} + \frac{V_{td}}{|V_{cd}V_{cb}^*|} = 1, \tag{1.9}$$

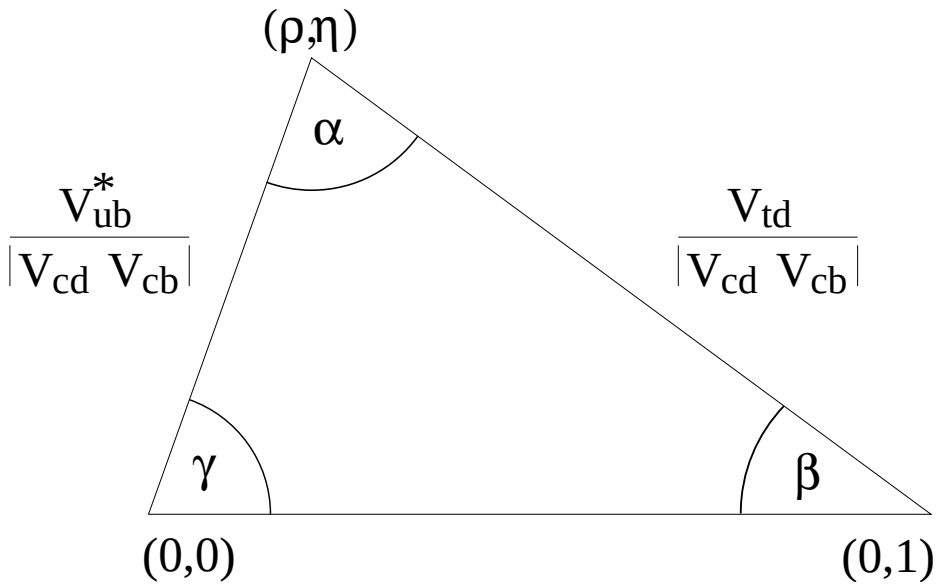

Figure 1.3: The triangle representing the unitarity condition applied to the first and third columns of the CKM matrix.

which relation can be represented graphically as a triangle in the complex plane (Fig. 1.3).

The unitarity of the CKM matrix leads to a total of six conditions like Eq. 1.8. This one is particularly interesting, however, because each of the three terms on the left-hand side are of similar size ($\mathcal{O}(\lambda^3)$). The triangle in Fig. 1.3 therefore has sides of similar length. Experiments can place constraints on these lengths, as well as on the triangle's three angles α, β and γ. Independent measurements of these quantities will allow us to check whether or not Eq. 1.8 holds and the CKM matrix is unitary.

Two important quantities in this test are accessible through the study of semileptonic decays of B mesons: the magnitudes of V_{cb} and V_{ub}. Since the element V_{cd} is well known, a measurement of V_{ub}, coupled with a value for V_{cb}, constrains the upper

left-hand side of the unitarity triangle.

1.3 Semileptonic Decays of B Mesons

Semileptonic B decays are those in which the products include both a bottomless meson X_q and a lepton-neutrino pair:

$$B \to X_q \ell \nu_\ell. \tag{1.10}$$

Here q labels the flavor of the b's daughter quark (either c or u). In general, the lepton ℓ can be an e, μ or τ. Since we limit ourselves in this thesis to the study of semileptonic B decays to electrons and muons only, hereafter the symbol ℓ indicates either an e or a μ, but not a τ. Furthermore, the subscript labeling the neutrino's flavor will be dropped, and its appropriate identity will be assumed. A tree-level Feynman diagram for semileptonic B decay is shown in Fig. 1.4. The presence of a leptonic current in the decay simplifies theoretical treatment relative to purely hadronic decays and makes the semileptonic decays particularly useful in determining $|V_{cb}|$ and $|V_{ub}|$.

The goal of the analysis described here is to observe a sample of leptons from semileptonic B decays in which the b quark is transformed into a u quark. The identity and specific properties of the hadronic final state X_u are not sought, so the momentum spectrum of the observed leptons is said to be "inclusive." This observed spectrum can be related to the total decay rate for $B \to X_u \ell \nu$, which in turn can be related to $|V_{ub}|$.

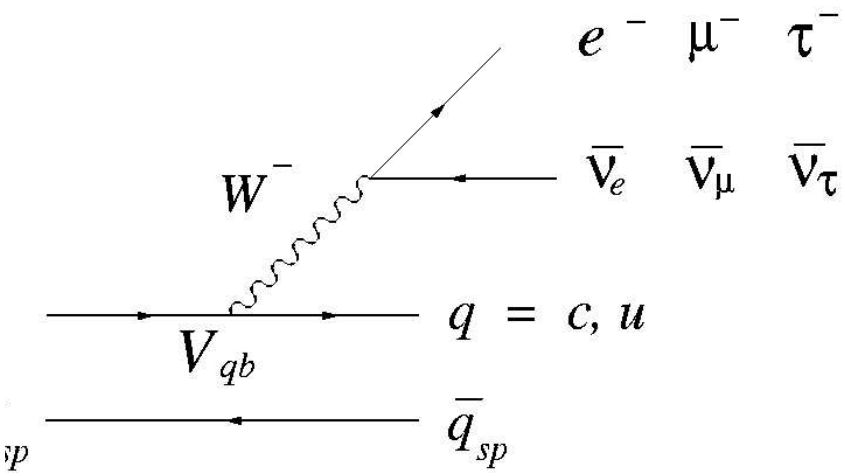

Figure 1.4: A tree-level Feynman diagram of semileptonic B decay. The B meson's valence-quark lines are shown. The accompanying quark q_{sp} in the meson decay does not participate in the b decay and is referred to as a "spectator," as is described in the text.

1.3.1 The Free-Quark Calculation of the Semileptonic Decay Rate

The decays represented in Fig. 1.4 result from W-mediated interactions between quark currents and lepton currents. Since the energies released in such decays are small compared to the W mass, their amplitudes take the form [12]:

$$M = -i\frac{G_F}{\sqrt{2}}V_{qb}L^{\mu}H_{\mu}, \tag{1.11}$$

where G_F is the Fermi constant and V_{qb} is an element of the CKM matrix. Generally speaking, the currents L^{μ} and H_{μ} are each formed from the sum of two terms which are transformed differently by the parity operator. The leptonic current is written in terms of Dirac spinors u_{ℓ} and v_{ν} and gamma matrices γ^{μ}, as follows:

$$L^{\mu} = \bar{u}_{\ell}\gamma^{\mu}(1-\gamma_5)v_{\nu}. \tag{1.12}$$

The hadronic current is written as

$$H_{\mu} = \langle X_q|\bar{q}\gamma_{\mu}(1-\gamma_5)b|B\rangle. \tag{1.13}$$

In general, it is difficult to evaluate this current since nonperturbative strong interactions are involved.

One can more readily calculate the semileptonic decay rate at the quark level ($b \to q\ell\nu$), neglecting the fact that the quark current is involved in strong interactions within the initial- and final-state mesons. In this case H_{μ} takes a form identical to L_{μ} in Eq. 1.12. In this approach, the other quark in the meson (q_{sp}) is referred to as a "spectator," because it does not participate in the decay process. Its presence has to be accounted for with subsequent corrections.

The free-quark decay is very similar to muon decay ($\mu \rightarrow e\nu_\mu\nu_e$). This process is one of the cleanest of all weak interactions, both experimentally and theoretically. Its total rate, neglecting the mass of the electron and all radiative corrections, is [1]

$$\Gamma_\mu = \frac{G_F^2 m_\mu^5}{192\pi^3}, \tag{1.14}$$

where m_μ is the mass of the muon.

Semileptonic b-quark decays differ from muon decays in two important respects: CKM matrix elements are involved and it is not always reasonable to neglect the mass of the final-state quark. Since quarks are always found bound in hadrons, their masses are ill-defined quantities. Even so, it is generally accepted that the b quark mass is around 4.7 GeV/c^2, while the c and u quarks have masses near 1.7 and 0.003 GeV/c^2, respectively. One can therefore neglect the final quark's mass for $b \rightarrow u$ transitions, while such a simplification is not possible for $b \rightarrow c$ decays. Note that in either case the final-state leptons, ℓ (e or μ) and ν, have negligible masses.

The total free-quark decay rate for $b \rightarrow q\ell\nu$ is

$$\Gamma_b = \frac{G_F^2 m_b^5}{192\pi^3}|V_{qb}|^2\Phi(m_q/m_b), \tag{1.15}$$

where Φ, the phase-space integral, is $\sim$1 for u quarks and $\sim$0.5 for c quarks. The ratio of the total rates for the two processes is then

$$\frac{\Gamma_{b\rightarrow u}}{\Gamma_{b\rightarrow c}} \approx 2 \times \frac{|V_{ub}|^2}{|V_{cb}|^2} \sim 1\%, \tag{1.16}$$

where I have used $|V_{ub}|/|V_{cb}| = 0.09$ [3]. So, if one wishes to isolate $b \rightarrow u\ell\nu$ decays, one has to somehow separate them from $b \rightarrow c\ell\nu$ decays, which occur 100 times more frequently.

The lepton momentum spectrum for free-quark decay is given by the differential decay rate:

$$\frac{d\Gamma_q}{dx} = \frac{G_F^2 m_b^5}{192\pi^3}|V_{qb}|^2\phi(x,y), \tag{1.17}$$

where x is the scaled lepton momentum $2E_\ell/m_b$ and y is the ratio of the daughter and b-quark masses m_q/m_b. The function ϕ includes both phase-space and weak-interaction information. It is given by [13]

$$\phi(x,y) = 2x^2\frac{(1-y^2-x)^2}{(1-x)^3}[(1-x)(3-2x)+y^2(3-x)]. \tag{1.18}$$

For $b \to u$ transitions we can take $y = 0$, giving

$$\phi(x,0) = 2x^2(3-2x). \tag{1.19}$$

This results in a spectrum which is maximum at $x = 1$, the kinematic limit for leptons in this decay. The free-quark spectra are shown in Fig. 1.5 for both $b \to u$ and $b \to c$ transitions. Note that the $b \to u$ spectrum peaks at high momentum while the $b \to c$ spectrum both peaks at a lower momentum and has a lower kinematic limit. This suggests that a viable method for isolating $b \to u$ decays is to look for leptons having sufficiently high momenta so that there is little background from $b \to c$ transitions. This approach led to the discovery of a nonzero $|V_{ub}|$ [14, 15]. Later, this technique provided a value of $|V_{ub}|$ that had a large theoretical uncertainty due to a heavy reliance on theoretical models [16]. This thesis presents an updated measurement of the inclusive lepton spectrum in the end-point region and an improved extraction of $|V_{ub}|$.

To determine $|V_{ub}|$ from an observation of the stiffest part of the lepton spectrum, one first needs to know the spectral shape $\frac{d\Gamma}{dx}$ in order to derive the total rate from the

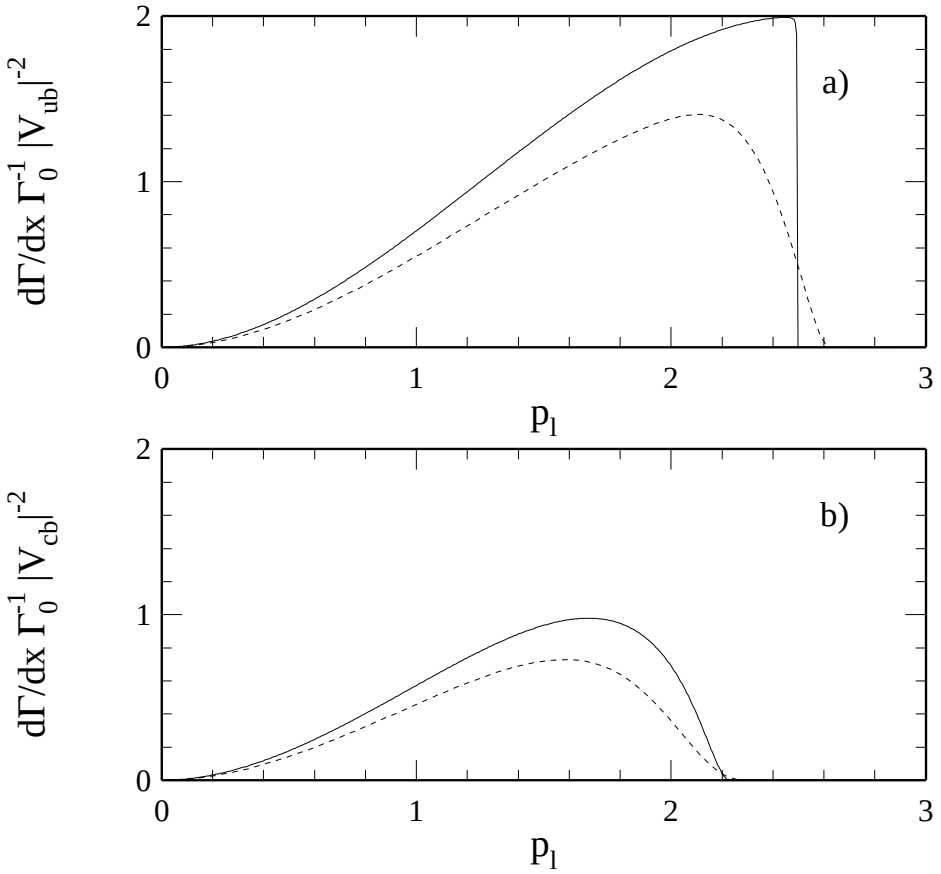

Figure 1.5: The free-quark and ACCMM spectator-model lepton spectra for semileptonic decays in the B rest frame. Both (a) $b \to u\ell\nu$ and (b) $b \to c\ell\nu$ are shown. The free-quark predictions are shown as solid lines, while the ACCMM predictions are shown as dashed lines.

observed fraction of the spectrum (f_u). A theoretical calculation of the the total rate Γ is then needed to extract $|V_{ub}|$. The calculations leading to Eq. 1.15 and Eq. 1.17 are naive in that they ignore the effects of the strong interaction inside the B meson. These interactions significantly alter the expressions for the desired quantities and therefore must be addressed. We turn now to a discussion of several strategies for including strong-interaction effects in the theoretical treatment of semileptonic B decay. These can be divided into two broad categories depending upon how they treat the hadronic final states. Inclusive approaches sum over all possible final-state hadronic systems, while exclusive approaches attempt to deal with each in turn, and then sum over each individual component to form inclusive spectra.

1.3.2 Inclusive Approaches to $\frac{d\Gamma}{dx}$

All inclusive treatments of $\frac{d\Gamma}{dx}$ build upon the simple spectator model. Throughout the decay, the b and u quarks are engaged in complicated strong interactions with the spectator quark and the surrounding sea of gluons and virtual quarks. Directly calculating all of the effects of these interactions with QCD is beyond the current state of the art. Theorists must instead resort to the use of simplified models and/or relationships between semileptonic and other types of B decay.

A part of the QCD corrections to the free-quark spectrum is directly calculable: the effect of (relatively) hard gluon emission. Lowest-order Feynman diagrams for these corrections are shown in Fig. 1.6. Because the strong coupling α_s decreases with increasing energy scale, these corrections can be calculated using a perturbative expansion. To first order, the result is a correction to the free-quark spectrum of

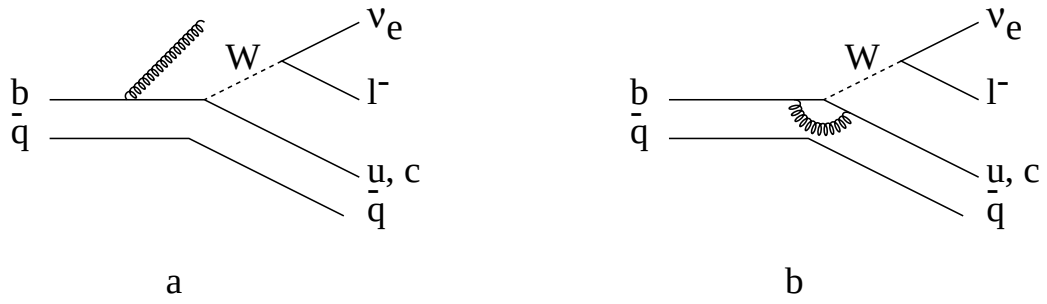

Figure 1.6: Spectator diagrams showing two types of gluon emission.

Eq. 1.17, here labeled as $\frac{d\Gamma^0}{dx}$, of the form

$$\frac{d\Gamma}{dx} = \frac{d\Gamma^0}{dx}[1 - \frac{2\alpha_s}{3\pi}G(x,y)]. \tag{1.20}$$

$G(x,y)$ has been computed analytically [17, 18] and results in a reduction of the rate at the kinematic limit for $b \to u\ell\nu$ lepton momenta to zero.

The remaining corrections to the free-quark decay rate involve softer processes and are therefore nonperturbative. They are related to the motion of the b quark inside of the B meson, commonly referred to as "Fermi motion." One approach to estimating these corrections was formulated by Altarelli, Cabibbo, Corbò, Maiani, and Martinelli [19] (ACCMM). Their model relies on a simple extension of the free-quark picture. The spectator quark is given a definite mass m_{sp} and is assumed to be moving with a momentum $\vec{p}$ in the rest frame of the B at the time of the decay. The b quark then has a momentum of $-\vec{p}$ and is given an effective mass W that conserves energy and momentum:

$$W^2 = m_B^2 + m_{sp}^2 - 2m_B\sqrt{p^2 + m_{sp}^2}, \tag{1.21}$$

where m_B is the mass of the B meson. The distribution of spectator quark momenta

in B decays is assumed to be Gaussian in shape, of unit area, and of adjustable width p_F, according to

$$\phi(|\vec{p}|) = \frac{4}{\sqrt{\pi} p_F^3} \exp\left(-\frac{|\vec{p}|^2}{p_F^2}\right). \tag{1.22}$$

The corrected lepton-energy spectrum is then formed by convoluting $\phi(|\vec{p}|)$ and $\frac{d\Gamma_q}{dE_\ell}$, the free-quark spectrum of Eq. 1.20 boosted to a quark-momentum p.

$$\frac{d\Gamma_B}{dE_\ell} = \int_0^{p_{max}} \phi(|\vec{p}|) p^2 dp \frac{d\Gamma_q}{dE_\ell}(W, \vec{p}, E_\ell). \tag{1.23}$$

Here p_{max}, the maximum allowed value of $|\vec{p}|$, makes W equal to the mass of the daughter quark.

The effects of these corrections on $b \to u$ and $b \to c$ decays can be seen in Fig. 1.5. The end points of the lepton spectra are extended beyond those for the free-quark model, reflecting the fact that the decaying b quark is not at rest in the B meson's rest frame. The free parameters of the model are α_s, m_{sp}, p_f, and m_B. We are most interested in the predicted *shape* of the spectrum, which is necessary for converting a measured partial spectrum in the end-point region to a total semileptonic $B \to X_u$ decay width. This depends most strongly on p_f, which affects the extent to which the spectrum reaches beyond the free-quark kinematic limit.

Although the intuitive picture used in deriving the ACCMM model's spectra is, even by its authors' admission, somewhat crude, its results have been shown to coincide with rigorous QCD calculations done to lowest order for transitions involving a *massless* daughter quark [20]. That is, the correspondence between the ACCMM model and QCD holds for $b \to u\ell\nu$ transitions, not for $b \to c\ell\nu$ decays.

The QCD-based approach to dealing with the b quark's motion inside the B meson

involves a "heavy quark expansion" in powers of $1/m_b$ [21]. While this approach is more complete and complex than the ACCMM model, it cannot be directly used to predict the shape of the spectrum near the end point due to the singular nature of the expansion there. There is, however, a way around this problem. The heavy quark expansion can be seen as providing a "shape function" F which describes the distribution of b-quark momenta inside the B meson. F can be convoluted with the free-quark spectrum in a manner analogous to the use of $\phi(|\vec{p}|)$ in the ACCMM approach to obtain the lepton energy spectrum in the B rest frame [22, 23, 24]. A key feature of F is that, to first order, it is *universal* for all B decays in which the b quark is transformed into an essentially massless daughter quark. The same shape function applies to $b \to u\ell\nu$ and the radiative "penguin" process $b \to s\gamma$, since m_u and m_s are negligible compared to m_b. The corresponding meson decay $B \to X_s\gamma$ bears the same relationship to $b \to s\gamma$ as the semileptonic decay $B \to X_u\ell\nu$ does to $b \to u\ell\nu$.

Spectator diagrams for $B \to X_s\gamma$ decays are shown in Fig. 1.7. The discovery of $B \to X_s\gamma$ by CLEO in 1995 [25] was a major milestone in the study of b quarks. Since the lowest-order diagrams for the process include loops, its measured rate provides constraints on physics beyond the Standard Model. An additional benefit of its study is that the that the inclusive photon-energy spectrum for $B \to X_s\gamma$ can be used to determine the shape function F, which can then be used to predict the form of the lepton-energy spectrum in $B \to X_u\ell\nu$.

Neglecting gluon radiation, the photon energy is simply $m_b/2$ in the rest frame of the b quark. The effects of gluon bremsstrahlung can be calculated using a per-

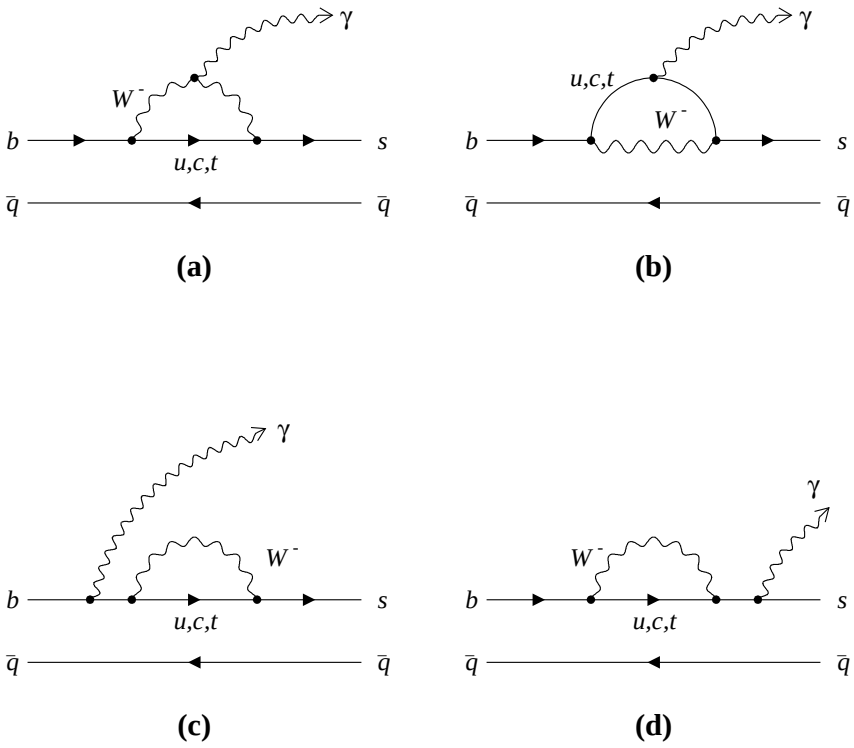

Figure 1.7: Feynman diagrams for radiative B decay to strange mesons. The B meson's valence-quark lines are shown.

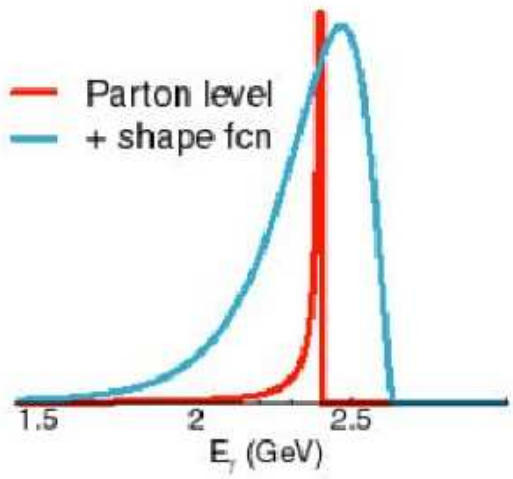

Figure 1.8: The photon-energy spectrum from radiative B decay. The spectrum for the parton-level decay $b \to s\gamma$ with perturbative QCD corrections is very narrow. The broader meson-level decay spectrum includes nonperturbative corrections as modeled with a shape function.

turbative expansion similar the one described for the $b \to u\ell\nu$ spectral calculation above [26]. The resulting spectrum, sharply peaked at $m_b/2$ with a tail extending to lower energies, is shown in Fig. 1.8. This parton-level spectrum is convoluted with the shape function to obtain the photon-energy spectrum in the B rest frame. The result is also shown in Fig. 1.8.

The CLEO experiment has recently measured the photon-energy spectrum from $B \to X_s\gamma$ decays [27]. The spectrum, shown in Fig. 5.1, is sufficiently well-measured to provide constraints on the shape function F. For the first time, CLEO can exploit the theoretical relationship between $B \to X_s\gamma$ and $B \to X_u\ell\nu$ to determine the

fraction of the lepton-energy spectrum in the end-point region.

Formally, the shape function is parameterized in terms of the residual b-quark momentum inside the B meson, k_+. While the exact form of $F(k_+)$ cannot be determined from theory, constraints on its shape are calculable [22, 23]. These are expressed as conditions on the moments A_n of $F(k_+)$:

$$A_n = \int dk_+ k_+^n F(k_+). \tag{1.24}$$

The first three moments satisfy:

- $A_0 = 1$
- $A_1 = 0$
- $A_2 = -\frac{1}{3}\lambda_1$,

where λ_1 is related to the kinetic energy of the b quark inside the B meson. These constraints are sufficient to allow theorists to postulate several possible functional forms for $F(k_+)$.

CLEO has fitted three of these forms, convoluted with a parton-level calculation of the $B \to X_s\gamma$ photon spectrum, to its measured spectrum. The three parameterizations are known as the exponential [26], Gaussian [26] and Roman [20] shape functions. Though their forms differ, they can all be expressed in terms of two parameters: the above-mentioned λ_1 and $\bar{\Lambda}$, which is related to the difference between the mass of the B meson and the b quark [28]. Fig. 1.9 shows a comparison of the three forms of $F(k_+)$ for the parameter values $\bar{\Lambda} = 0.545$ GeV and $\lambda_1 = -0.33$ GeV^2.

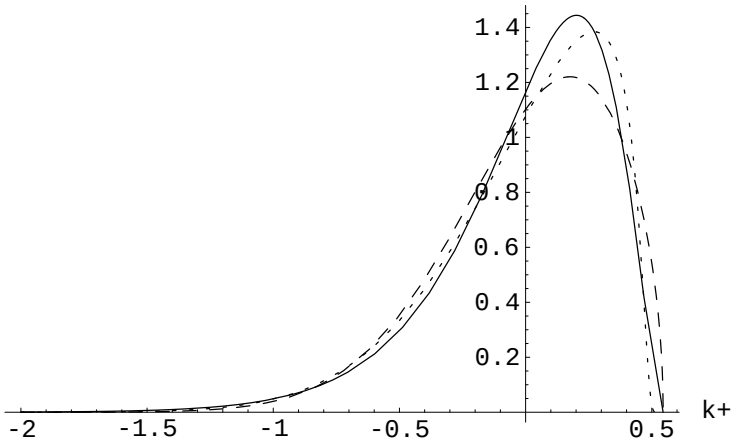

Figure 1.9: Three forms of the shape function $F(k_+)$ computed for the parameter values $\bar{\Lambda} = 0.545$ GeV and $\lambda_1 = -0.33$ GeV^2. The exponential, Gaussian and Roman shape functions are shown as solid, dashed and dotted lines, respectively.

Let $P_q(y_q)$ be the photon-energy spectrum calculated in the parton model with perturbative corrections. Here y_q is the photon energy scaled to the mass of the b quark: $y_q = 2E_\gamma/m_b$. $P(y)$, where $y = 2E_\gamma/m_B$, is the spectrum in the meson rest frame. It is given by [29]

$$P(y)dy = \int dk_+ F(k_+) \left[P(y_q)dy_q\right]_{y_q=y_q(k_+)}, \tag{1.25}$$

where $y_q(k_+)$ is calculated by replacing m_b with the effective mass $m_b^* = m_b + k^+$. The result is a spectrum that extends to $y = 1$, or $E_\gamma = m_B/2$, the correct kinematic end point in the meson rest frame. Calculated spectra for the three forms of the shape function shown in Fig. 1.10. Other kinematic distributions, such as the daughter hadronic mass spectrum, can be calculated with similar integrals. The meson-frame lepton spectrum for $B \to X_u \ell\nu$ is calculated with an expression analogous to Eq. 1.25.

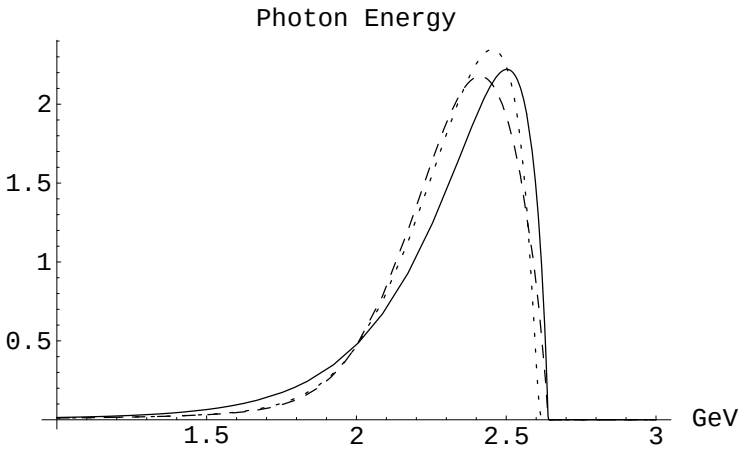

Figure 1.10: Photon spectra calculated using three forms of the shape function $F(k_+)$ computed for the parameter values $\bar{\Lambda} = 0.545$ GeV and $\lambda_1 = -0.33$ GeV^2. Spectra calculated with the exponential, Gaussian and Roman shape functions are shown as solid, dashed and dotted lines, respectively.

Details of CLEO's fits to the measured $B \to X_s\gamma$ photon-energy spectrum, and the resulting f_u calculations, are presented in Sect. 5.2.

1.3.3 Exclusive Approaches to $\frac{d\Gamma}{dx}$

Another approach taken to include the strong interaction in the decay is to modify the form of the quark current from that given in Eq. 1.13. The current is a four-vector, and must be constructed from the four-vectors available in the decay. In the rest-frame of the B, only the four-momenta of the final state particles and the polarization vector of X_u, if it is a vector particle, are available. The current is thus a sum of these four-vectors multiplied by coefficients, or "form factors," which are Lorentz invariant.

For the case where the final state meson is a pseudoscalar m, the hadronic current takes the form [30]

$$H_\mu = \langle m|J_\mu^{had}|\bar{B}\rangle = f_+(q^2)(P+p)_\mu + f_-(q^2)(P-p)_\mu, \tag{1.26}$$

where P and p are the four momenta of the B and m mesons, respectively. The form factors f_+ and f_- depend on the squared mass of the virtual W, $q^2 = (P-p)^2$. It turns out that the second term in Eq. 1.26 makes no contribution to the decay's matrix element for the case when the final-state lepton is massless [12]. Therefore, it can be neglected when $\ell = e$ or μ, and $B \to m\ell\nu$ decays are, to good approximation, described by one form factor $f_+(q^2)$, also known as $F_1(q^2)$. Semileptonic B decays to vector mesons are more complicated, since the polarization vector ϵ of the final-state hadron is also available for use in constructing terms in the hadronic current. Three independent form factors $A_1(q^2)$, $A_2(q^2)$ and $V(q^2)$ are needed to describe these decays.

To determine the $B \to X_u\ell\nu$ decay rate, both the normalization and functional form of the relevant form factor(s) must be determined. One approach to doing this involves modeling the inital- and final-state mesons as pairs of quarks bound in a potential well. Once a potential model is assumed, the meson wavefunctions are estimated and form-factor values at a particular value of q^2, either $q^2 = 0$ or $q^2 = q^2_{max}$, are computed. The variation of the form factors with q^2 is computed in a separate step. Note that this approach is limited to decays in which there is only one final-state hadron. So-called "non-resonant" decays, in which there are multiple hadrons in the final state, are not addressed by this method.

One successful exclusive model is that of Isgur and Scora and is known as ISGW2 [31]. It is an update of the model of Isgur, Scora, Grinstein and Wise (ISGW) [32]. This model uses a Coulomb-plus-linear form for the meson potential $V(r)$. The form factors are calculated at the point of zero-recoil, q^2_{max}, and the extrapolation to lower q^2 is assumed to take an exponential form. This approach was used to calculate form factors for $B \to X_u \ell\nu$ transitions to all mesons having masses less than 1.7 GeV. The sum over all spectra from these decay resonances is felt to be complete for lepton energies greater than about 2.4 GeV. Since the model does not include all possible final states, it cannot be used to estimate the total rate for $B \to X_u \ell\nu$.

The ISGW2 model also describes semileptonic decays to charmed final states, $B \to X_c \ell\nu$. For these decays, however, an approximate symmetry motivates a powerful alternative approach. This theory, known as Heavy Quark Effective Theory (HQET) begins with the approximation that both the parent b and daughter c quarks have equal and infinite masses. This is known as the "heavy-quark limit." In this limit, the light degrees of freedom in the B- and daughter-meson systems are unaffected by the decay of the b quark. One simplification that results from this is that all form factors for semileptonic B decays to pseudoscalar and vector mesons are proportional to the Isgur-Wise function $\xi(w)$. Here w is the scalar product of the initial and final hadrons' four velocities v and v', respectively:

$$w = v \cdot v'. \tag{1.27}$$

It is linearly related to q^2 and is useful in describing the behavior of the form factors because in HQET only the velocities are important for characterizing the hadronic

systems. Additionally, in the heavy-quark limit, the velocities of the initial and final mesons are the same as the velocities of the heavy quarks that they contain.

Since the Isgur-Wise function $\xi(w)$ describes nonperturbative effects, its variation with w is typically explored with techniques like Lattice QCD or QCD sum rules. However, over the range of w available in $B \to D^{(*)}\ell\nu$ decays, the approximate form

$$\xi(w) = 1 - \rho^2(w-1) + \mathcal{O}\left[(w-1)^2\right] \tag{1.28}$$

is often used.

The decays $B \to D\ell\nu$ and $B \to D^*\ell\nu$ together dominate the B-meson semileptonic decay rate and are our most important backgrounds. Measurements have placed constraints on the form factors involved in these decays. For $B \to D\ell\nu$, the differential decay rate is [33]

$$\frac{d\Gamma_{B\to D\ell\nu}}{dw} = \frac{G_F^2|V_{cb}|^2}{48\pi^3}(m_B + m_D)^2(m_D\sqrt{w^2-1})^3\mathcal{F}_D(w)^2. \tag{1.29}$$

The form factor $\mathcal{F}_D(w)$ is proportional to the traditional form factor $F_1(w)$. It is taken to have the same w dependence as $\xi(w)$:

$$\mathcal{F}_D(w) = \mathcal{F}_D(1)\left[1 - \rho_D^2(w-1)\right]. \tag{1.30}$$

In the heavy-quark limit $\mathcal{F}_D(w)$ *is* $\xi(w)$, and it becomes unity at zero-recoil (i.e., $\mathcal{F}_D(1) = 1$). The true value of $\mathcal{F}_D(1)$ can be estimated using the framework of HQET, although the errors are somewhat difficult to quantify. A measurement of $d\Gamma_{B\to D\ell\nu}/dw$ at CLEO has placed constraints on both the rate normalization $|V_{cb}|\mathcal{F}_D(1)$ and the form-factor slope ρ_D^2 [34], which influences the shape of the decay's lepton momentum spectra.

A CLEO measurement has also been used to constrain the three form factors for the decay $B \to D^* \ell \nu$ [35]. In this case the quantities directly measured include the form-factor ratios R_1 and R_2, where

$$R_1(w) = \left[1 - \frac{q^2}{(m_B + m_{D^*})^2}\right] \frac{V(q^2)}{A_1(q^2)} \tag{1.31}$$

and

$$R_2(w) = \left[1 - \frac{q^2}{(m_B + m_{D^*})^2}\right] \frac{A_2(q^2)}{A_1(q^2)}. \tag{1.32}$$

In the heavy-quark limit, both R_1 and R_2 are predicted to be unity. In addition to this, the analysis assumed a functional form for the form factor A_1:

$$A_1(q^2) = \frac{m_B + m_D}{2\sqrt{m_B m_D}} \left[1 - \frac{q^2}{(m_B + m_D^*)^2}\right] h_{A_1}(w). \tag{1.33}$$

Here $h_{A_1}(w)$ has the same functional form as $\xi(w)$ and they are identical in the heavy-quark limit:

$$h_{A_1}(w) = h_{A_1}(w) \left[1 - \rho^2_{A_1}(w-1)\right]. \tag{1.34}$$

Constraints on R_1, R_2 and $\rho^2_{A_1}$ were obtained by measuring the differential decay rate $d\Gamma_{B \to D^* \ell \nu}$, binned in four kinematic variables: q^2, $\cos\theta_l$, $\cos\theta_v$, and χ. Here θ_l is the decay angle of the lepton in the W rest frame, θ_v is the decay angle of the D in the D^* rest frame, and χ is the angle between the W and D^* decay planes in the B rest frame. To obtain the predicted shape of $d\Gamma_{B \to D^* \ell \nu}$, both R_1 and R_2 were assumed to be constant. Fits to data then provided experimental values of R_1, R_2 and the form-factor slope $\rho^2_{A_1}$.

1.3.4 Calculation of $\Gamma(B \to X_u \ell\nu)$

Unlike $\frac{d\Gamma}{dx}$, the total semileptonic decay rate $\Gamma(B \to X_u \ell\nu)$ calculated using the heavy-quark expansion has controllable errors. Here again short-distance physics, associated with the b quark, is separated from the long-distance physics associated with the light degrees of freedom. The result is a double expansion in powers of $\alpha_s(m_b)$ and Λ_{QCD}/m_b [36, 21, 37, 38, 39]. The $\alpha_s(m_b)$ expansion comes from the application of perturbative QCD to the short-distance part of the decay. The heavy-quark expansion deals with the softer processes at or below Λ_{QCD}, which is of the order of hundreds of MeV. The long-distance corrections are written in terms of the parameters λ_1 and λ_2. The first of these, λ_1, is related to the b quark's kinetic energy inside the B meson. The parameter λ_2 is related to the energy of the b quark's hyperfine interaction with the light degrees of freedom. The result, up to order $1/m_b^2$ in the heavy-quark expansion, and with the complete radiative correction of order α_s [40], is

$$\Gamma(B \to X_u \ell\nu) = \frac{G_F^2 |V_{ub}|^2}{192\pi^3} m_b^5 \left[1 + \left(\frac{25}{6} - \frac{2\pi^2}{3}\right)\frac{\alpha_s(m_b)}{\pi} + \frac{\lambda_1 - 9\lambda_2}{2m_b^2} + ...\right]. \quad (1.35)$$

Eq. 1.35 suffers from two problems: it depends upon the poorly defined quark mass m_b, and its perturbation series is badly behaved at high orders. Several approaches to dealing with these issues exist, however. The resulting expressions for $\Gamma(B \to X_u \ell\nu)$ can be used to relate $|V_{ub}|$ to the total B charmless branching fraction $\mathcal{B}(B \to X_u \ell\nu)$. An average of the formulations of Hoang *et al.* [41] and Uraltsev [42] yields

$$|V_{ub}| = (3.07 \pm 0.12) \times 10^{-3} \times \left[\frac{\mathcal{B}(B \to X_u \ell\nu)}{0.001}\frac{1.6 \text{ ps}}{\tau_B}\right]^{\frac{1}{2}}, \quad (1.36)$$

where τ_B is the B lifetime.

1.3.5 Quark-Hadron Duality

The inclusive calculations of $\frac{d\Gamma}{dE_\ell}$ and Γ discussed above rely on the assumption of quark-hadron duality. That is, they all begin with parton-level calculations and average over the details of the recoiling hadronic system. In particular, they give no information about the presence of resonances in the X_u system. As long as a measurement samples a sufficiently large region of phase space, it is felt that this technique does not introduce a significant error. Therefore duality concerns contribute a negligible uncertainty to Eq. 1.36, since it relies on a calculation of the *total* decay rate [43]. However, extraction of the total charmless semileptonic branching fraction from a measurement of the end-point lepton momentum spectrum from $B \to X_u \ell \nu$ may suffer from the limitations of this approach. Inclusive calculations say nothing about the details of decays like $B \to \pi \ell \nu$ that populate the extreme end point of the spectrum. Therefore they cannot be used with confidence to predict the fraction of the E_ℓ spectrum that is in its very end point. It is not known how to quantify the theoretical error associated with the duality assumption in this case, but there is general agreement that the more of the spectrum that is sampled, the better the measurement will be.

1.4 The Goal of this Thesis

The goal of this thesis is a determination of the magnitude of the CKM matrix element V_{ub} using a measurement of the lepton-energy spectrum from the process $B \to X_u \ell \nu$ in the region around the kinematic end point for the dominant semileptonic decay

$B \to X_c \ell\nu$. To reduce theoretical uncertainty, a great deal of effort was invested in lowering the lower bound on the region of the spectrum sampled. For the first time, a theoretical connection between $B \to X_u \ell\nu$ and radiative decays $B \to X_s \gamma$ is used to extract the total branching fraction $\mathcal{B}(B \to X_u \ell\nu)$ from the observed yield in the end-point region. This approach makes use of CLEO's recently-measured photon-energy spectrum and results in smaller and better-estimated errors than those of previous $|V_{ub}|$ measurements.

The data used in this measurement was collected by the CLEO-II experiment operating at the Cornell Electron Storage Ring (CESR). The storage ring, detector and related software are all described in Chapter 2. Chapter 3 details the analysis procedure used to isolate leptons from $B \to X_u \ell\nu$ from backgrounds. Chapter 4 presents measured signal and background yields. The extraction of $|V_{ub}|$ is described in Chapter 5, which concludes with a discussion of the measurement's theoretical uncertainties and the prospects for improvement at high-luminosity B factories.

CHAPTER 2

Experimental Apparatus

Production of B mesons and detection of their decay products are technically challenging tasks. The work represented in this thesis was made possible by the efforts of hundreds of people that collaborated in the design, construction, and operation of the accelerator and detector apparatus at the Cornell University Laboratory of Elementary Particle Physics. This chapter provides a brief description of these remarkable machines.

2.1 CESR - The Cornell Electron Storage Ring

CESR (pronounced Caesar) is an electron storage ring 244 meters in diameter located 12 meters below the Cornell University campus [44]. Since 1979, electron and positron bunches have been made to collide in CESR at center-of-mass energies in the range from 9 GeV to 12 GeV. (CESR is currently undergoing modifications to operate efficiently at energies as low as 3 GeV.) The data used in this analysis was accumulated from 1990 to 1999, when CESR was mainly operating at energies around 10.58 GeV.

The storage ring is itself part of the larger facility shown schematically in Fig. 2.1. Beam production begins with a hot-cathode electron gun at the beginning of a linear

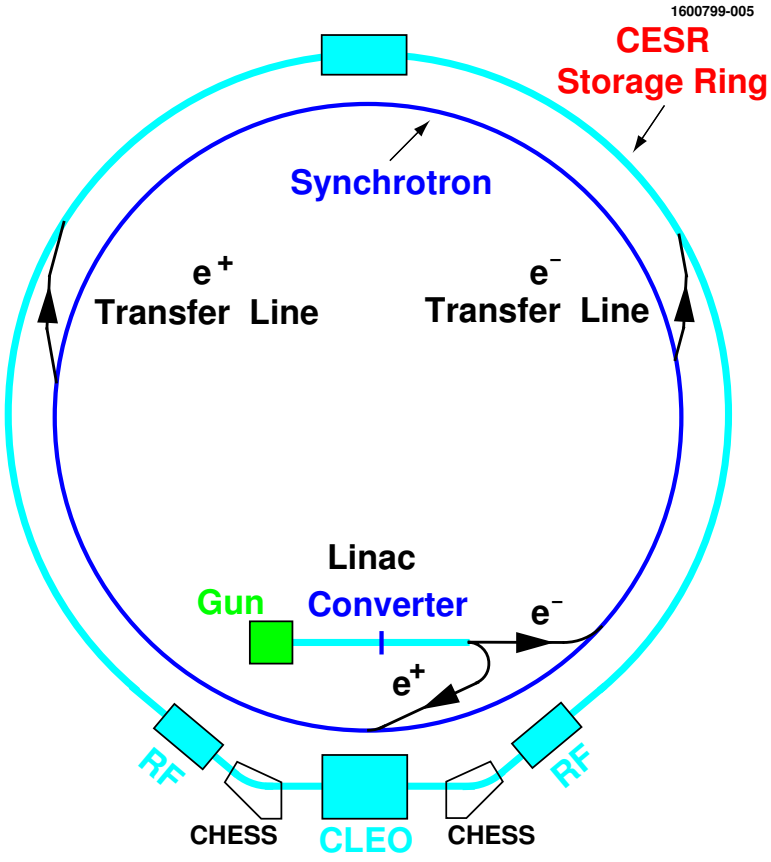

Figure 2.1: The colliding-beam facility at Cornell.

accelerator (LINAC). Electrons from a hot filament are first collimated and then accelerated through a 30-meter-long vacuum pipe to energies of around 300 MeV using a series of radio-frequency (RF) cavities. They are then injected into a synchrotron that accelerates them to 5 GeV before they are transferred into CESR for storage.

Production of positrons requires an extra step: midway through the LINAC, a tungsten target intercepts the 140 MeV electrons. The resulting collisions generate showers of electrons, positrons, and X-rays. Positrons are selected, focused, and then accelerated to energies of about 200 MeV before being injected into the synchrotron.

Inside the synchrotron, electrons or positrons travel around an evacuated ring that mostly consists of 192 three-meter sections containing bending and focusing magnets. At four places in the ring, particles pass through 3-meter-long linear accelerators. It takes about one hundredth of a second, or 4,000 circulations, for particles to reach their maximum energy in the synchroton.

Particles are next injected into the storage ring, where magnets confine the bunches in stable orbits. Electron and positron bunches counter-circulate in CESR at the same time and are kept apart using magnets and electrostatic separators. RF cavities are used to restore energy lost by the particles to synchroton radiation. Bunches are steered into one another at an interaction point (IP), where the array of detectors of the CLEO experiment studies the products of the resulting collisions.

Improvements over the years have allowed CESR's accelerator physicists to increase the number of particles stored in the ring. Since early 1999, CESR has operated with nine bunch trains each of electrons and positrons. Each train consists of as many as five bunches. The peak current stored in CESR during the collection of

our data sample was around 0.5 A (∼250 mA each of electrons and positrons), with total RF power of 0.5 MW.

The rate of collisions in CESR is described by a quantity called the luminosity. It is defined as

$$\mathcal{L} = nf\frac{N_{e^+}N_{e^-}}{A}. \tag{2.1}$$

Here f is the frequency of revolution, n is the number of electron bunches in the beam, N_{e^+} and N_{e^-} are the numbers of positrons and electrons in each bunch, and A is the cross-sectional area of the beams. The highest luminosity achieved during the time period when the data used in this thesis was taken was $0.8 \times 10^{32} cm^2 s^{-1}$ [45]. Fig 2.2 shows the yearly-integrated luminosity generated by CESR from 1985 to mid-2001. Dips in 1995 and 1999 correspond to extended shutdowns for major modifications to both CESR and the CLEO experiment.

The integral of $\mathcal{L}$ over a given time interval can be related to the total number of times N that a particular physics process occurs:

$$N = \sigma \int \mathcal{L} dt. \tag{2.2}$$

Here σ is the cross section of the process in question. Fig 2.3 shows the total cross section for e^+e^- annihilation at center-of-mass energies around 10 GeV [46, 47, 48]. The enhancements evident in this plot are known as Upsilon (Υ) resonances. They correspond to production of S-wave $b\bar{b}$ bound states. At 10.58 GeV the total hadronic cross section is about 4 nb ($1b = 10^{-24} cm^2$). One quarter of this is due to production of the $\Upsilon(4S)$ and the rest is from "continuum" production of lighter quark pairs. The $\Upsilon(4S)$ is wider than the lower energy Υ resonances because it is just above the

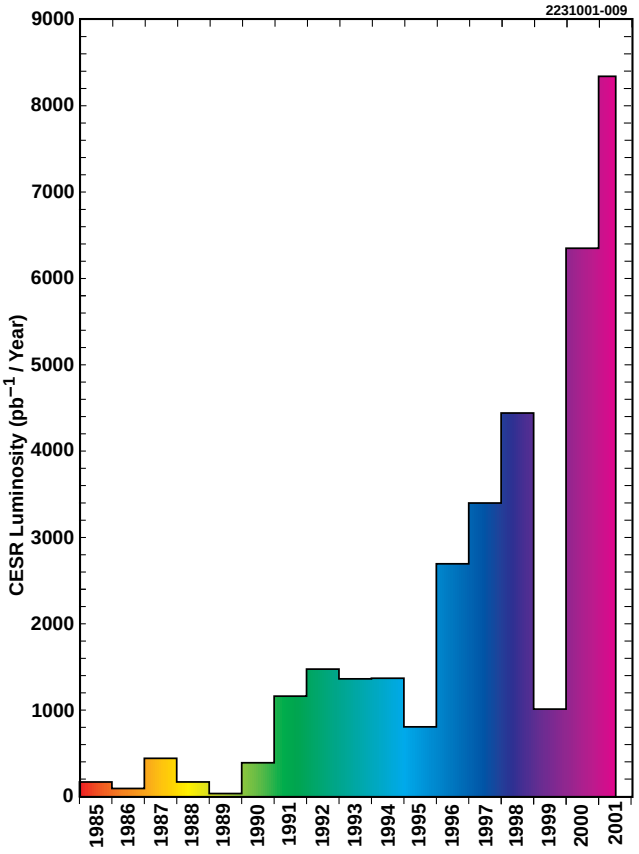

Figure 2.2: Annual integrated luminosities from CESR.

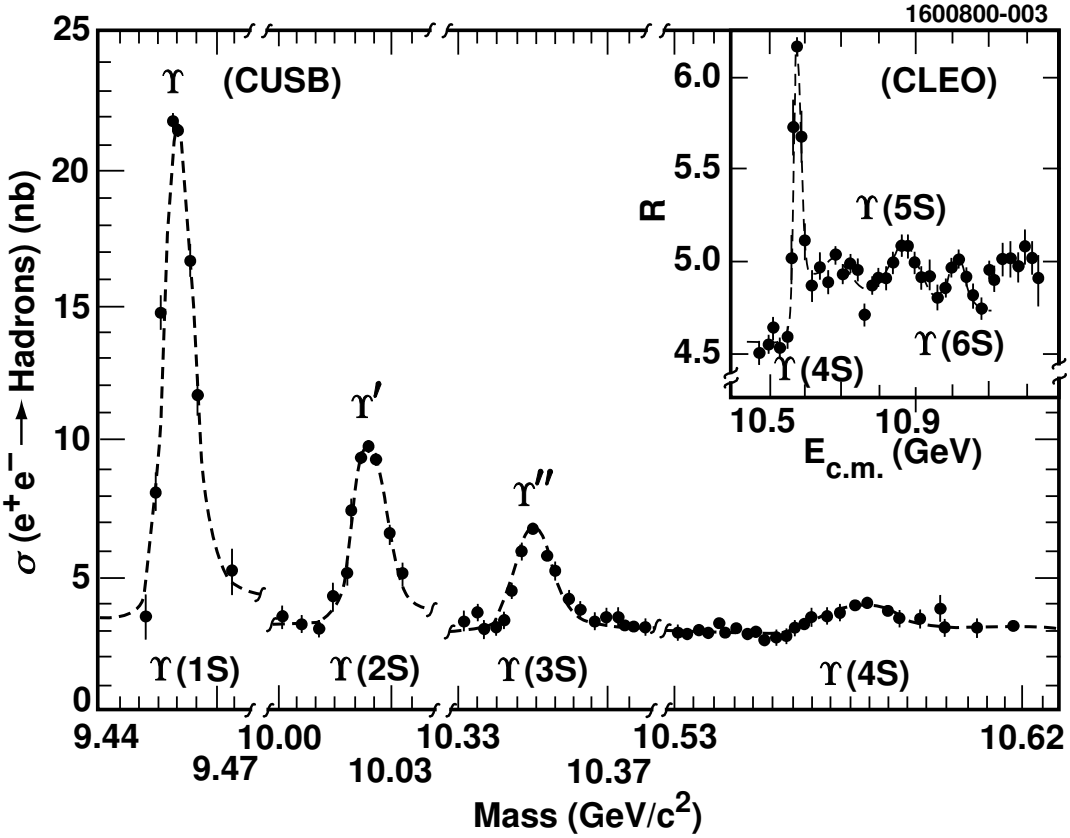

Figure 2.3: The hadronic cross section in the Upsilon region.

threshold for decay into a pair of B mesons, each with a mass of about 5.28 GeV/c^2. The data sample used for this thesis represents an integrated luminosity of 9.13 fb^{-1} at center-of-mass energies near 10.58 GeV (hereafter referred to as "on resonance" or simply ON). This corresponds to a sample of about 9.7 million $B\bar{B}$ pairs. An additional 4.35 fb^{-1} was collected just below the $\Upsilon(4S)$. This provides a sample of continuum events that is useful in estimating backgrounds to B physics.

2.2 The CLEO II Experiment

The CLEO collaboration has surrounded the IP at CESR with a set of instruments which provide acceptance over nearly all 4π of the solid angle. Two different detector configurations collected the data used in this analysis. The critical component of each was a multiple-layer composite tracking system inside a 1.5 T solenoidal magnet. This provided measurements of charged particles' specific ionizations ($\frac{dE}{dx}$) and momenta. Charged particles' times-of-flight were measured with plastic scintillators and phototubes surrounding the tracking system. A cesium-iodide calorimeter just inside the magnet detected electromagnetic showers generated in the crystals by photons and charged particles. Outside the magnet, proportional counters embedded in iron detected muons. Fig. 2.4 shows a drawing of the CLEO II experiment, which operated from 1989 to 1995, when part of the inner tracking system was upgraded and other improvements were made. The resulting detector configuration, known as CLEO II.V, took data until early in 1999. In the summer of that year the entire tracking system was replaced, the scintillator detector was removed, and a new particle

identification system was installed. The resulting experiment, known as CLEO III, is still in operation as of this writing. While detailed descriptions of the detectors' configurations and performances are given elsewhere [49, 50, 51], a brief survey of the most important points is provided here. Throughout the discussion, the following coordinate system will be used: the z axis points along the beam line in the direction of positron motion, the y axis points upward and the x axis points outward from the center of CESR. Points in the x-y plane are specified in terms of their radial distance r from the beam line and an angle ϕ measured from the y axis. The polar angle θ is defined with respect to the z axis.

2.2.1 Tracking

Upon exiting the beam pipe, a charged particle generated at the IP first encounters a set of devices designed to measure its trajectory. Prior to 1995, these consisted of three nested wire chambers [52]. These types of detectors make use of wires held at high positive voltage and suspended in a mixture of gases (argon/ethane before 1995, helium/propane thereafter). Grounded wires or a grounded conducting tube form a "cell" around each anode or "sense" wire. As a charged particle moves through the gas, it ionizes gas atoms. Electrons thus liberated in a given cell drift under the influence of an electric field to the central sense wire. Very near the wire, the field is of such strength that the drifting electrons become energetic enough to ionize gas molecules themselves, releasing more electrons which then further ionize the gas. The resulting "avalanche" of ionization produces a measurable charge on the sense wire known as a "hit." The timing of the hit allows an estimation of the particle's

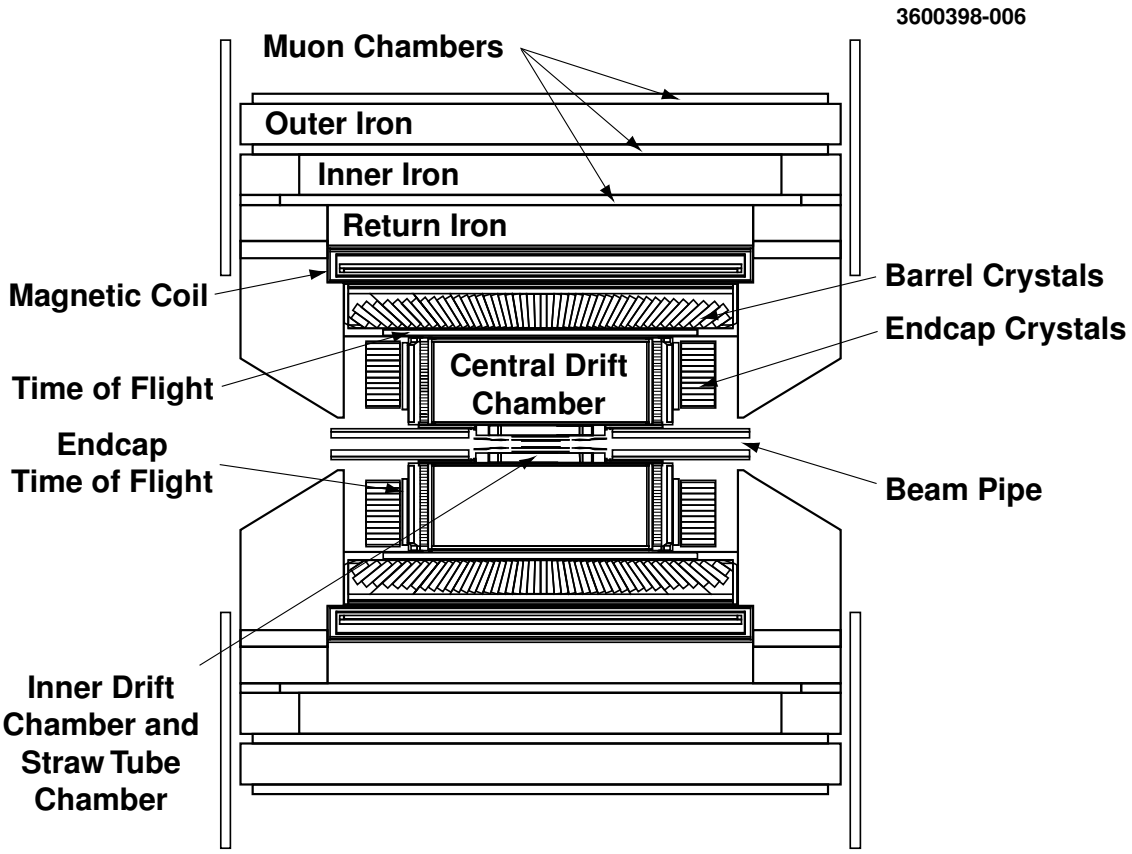

Figure 2.4: A CLEO II detector side view.

distance of closest approach to the anode wire. Combined information from multiple, staggered, cells can be used to measure precisely a particle's trajectory through the tracking device.

Because CLEO's tracking chambers are inside a magnetic field, charged particles follow a helical path. The magnetic field is along the z axis so that, in the r-ϕ plane, the radius of curvature a of a particle's track is related to its transverse momentum $p_\perp$ by the relation

$$p_\perp = qBa, \tag{2.3}$$

where q is the magnitude of the particle's charge and B is the magnitude of the magnetic field. Thus a measurement of a particle's trajectory provides a measurement of its momentum. Furthermore, the direction of curvature indicates the sign of a particle's charge.

The innermost tracking chamber in CLEO II was known as the Precision Tracker (PT). A cross section of its layout is shown in Fig. 2.5. It was a six-layer straw tube drift chamber consisting of multiple cells, each defined by a tube of aluminized mylar that acted as a cathode. A single sense wire was strung down the center of each tube. The tubes were mounted directly on the beam pipe in a hexagonal closest-packed arrangement. They varied in diameter from 4.5 mm to 7.5 mm and provided the smallest cell size in all the drift chambers. Averaged over its volume, the PT had an r-ϕ resolution of about 100 μm.

The Vertex Detector (VD) surrounded the PT (see Fig. 2.5). It was a multi-wire proportional chamber with small wire spacing. Ten layers of drift cells were composed of anode wires, each surrounded by a hexagonal arrangement of cathode wires. The

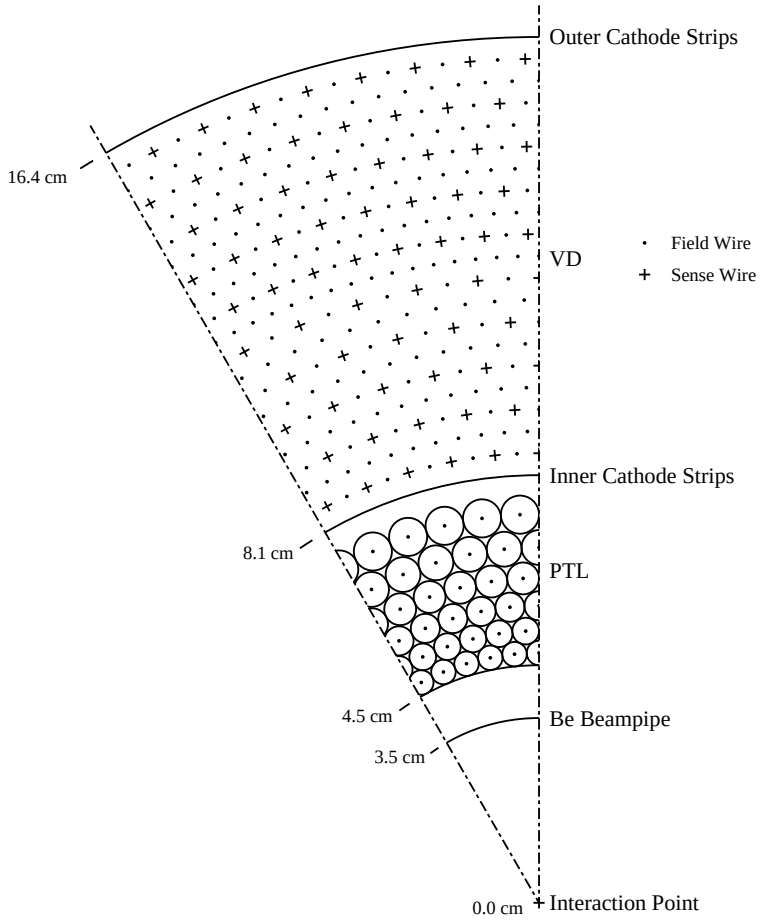

Figure 2.5: The radial layout of the CLEO II inner tracking chambers.

average r-ϕ resolution of the VD was about 150 μm. The sense wires in the VD were made from high resistance nickel-chromium wires. Signals were read out from both ends of the wires, allowing a measurement of the z position of a hit by charge division. The resulting z resolution was about 1.7 cm. Further z information was provided by segmented cathodes on the inner and outer surfaces of the VD. Image charges induced on the cathodes by pulses near the inner- and outermost anode wires were also recorded and provided a z resolution of about 750 μm. Each cathode had eight separately-read strips in ϕ, and the inner (outer) cathode had 64 (96) segments in z.

In 1995, the PT was replaced by a silicon vertex detector, pictured in Fig. 2.6. It consisted of three concentric layers of 300-μm-thick Si wafers mounted directly onto the beam pipe. The wafers contained many thin and long p-n junctions with depletion zones that were enhanced by an applied reverse-biased voltage. Conducting strips on both sides of each wafer gathered charge liberated by charged particles passing through the depleted region. Electrons were gathered on one side, holes were gathered on the other. On average, deposited charge from a single track was distributed among two or three strips on each side. The position resolution achieved by this device was about 30 μm in r-ϕ and 60 μm in z, much superior to the earlier, purely gas-based tracking system.

The largest and most important tracking device in CLEO II was known as the central drift chamber or DR [53]. Its 52 layers provided most of the information used in the measurement of charged-particle momenta. A total of 12,240 anode and 36,240 cathode wires were arranged in a pattern of square drift cells with each layer staggered

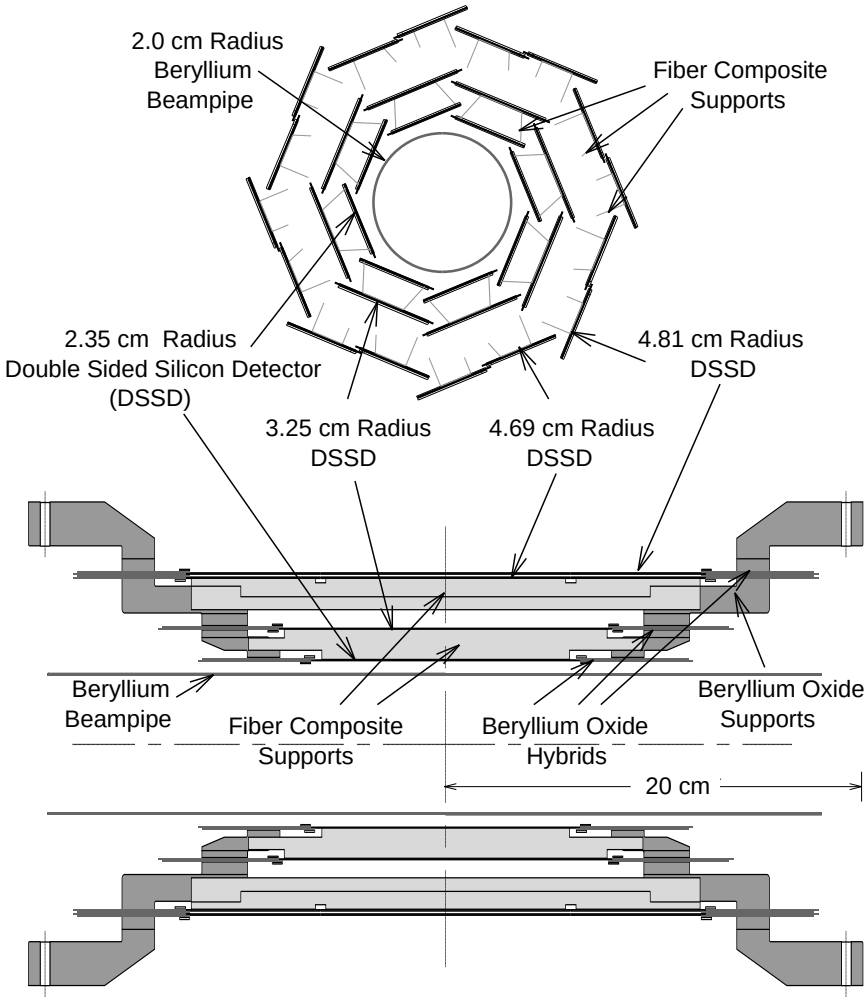

Figure 2.6: End-on (top) and side (bottom) cross-sectional views of the CLEO II.V silicon vertex detector.

by one half of a cell. The number of cells in a layer increased with radius so that all cells were of approximately the same size: 15 mm by 15 mm. Electronics monitored both the drift time and the amount of ionization left in a cell by a passing track. Some layers had anode wires which were skewed from the z axis by a few degrees. These "stereo" layers provided information about the z coordinate of the tracks that crossed them. Additional z information came from segmented cathodes on the inner and outer surfaces of the DR. The averaged r-ϕ resolution for the DR was around 150 μm, while the z resolution of the stereo layers varied from 3 to 5 mm.

Altogether, the CLEO II tracking system covered about 95% of the solid angle. For $\sim$2 GeV/c tracks that passed through all of the DR ($|\cos\theta| <\sim 0.71$) it provided a momentum measurement with a precision of 0.6%.

2.2.2 Time-of-Flight Measurement

A time-of-flight detector (TF) surrounded CLEO's tracking chambers. Its purpose was to measure the elapsed time between a particle's creation at the IP and passage through the TF, approximately one meter away. When combined with a momentum estimate, such a measurement provides some discrimination among particle species of differing mass.

The TF made use of scintillation counters. These were made from a special plastic that was doped to make it emit light, or scintillate, when a charged particle passed through. This material was arranged into three sections to provide better solid-angle coverage (see Fig. 2.4). The barrel section consisted of 64 rectangular blocks, each 2.8 m by 10 cm by 5 cm, arranged to form a cylindrical shell centered on the beam

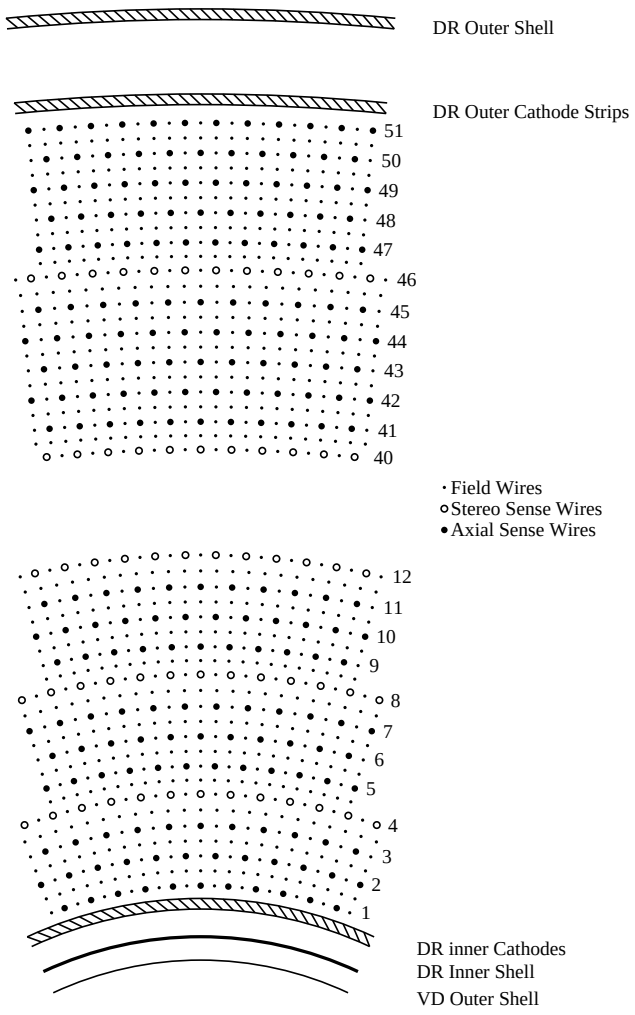

Figure 2.7: A cross-sectional view of the CLEO II main drift chamber. The drawing begins with the VD outer shell and extends outward to show some of the layers of the DR.

axis. This arrangement covered the angular region from $36^\circ < \theta < 144^\circ$. The light generated in each section, or counter, was fed through lucite light guides to a pair of photomultiplier tubes, one on each end. The time-resolution of this system was about 150 ps. There were also two endcap sections situated outside the DR endplates. These were each composed of 28 wedge-shaped counters about 58 cm long and 5 cm thick. A single photomultiplier tube collected light on the narrow end of each counter. The TF endcaps covered the angular regions from $15^\circ < \theta < 36^\circ$ and $144^\circ < \theta < 165^\circ$. The entire TF covered 97% of the solid angle.

2.2.3 Calorimetry

An electromagnetic crystal calorimeter (CC) occupies the space just inside CLEO's superconducting magnet [54]. It was designed to measure particles' energies. The amount of energy lost by a particle prior to entering the CC was reduced by keeping the amount of material traversed to a minimum. This motivated the detector's placement inside of the magnet. The CC consists of about 7,800 thallium-doped cesium-iodide crystals, 80% of which are arranged in a barrel-shaped configuration just inside the solenoid. The remainder occupy two endcap detectors. Each crystal is approximately 30 cm long and 5 cm square in cross section. Barrel crystals are tilted to point slightly away from the IP in order to minimize gaps through which particles can pass undetected.

Particles entering these high-density crystals interact with the material and lose energy through processes including ionization, bremsstrahlung, pair conversion, and nuclear interactions. Electromagnetic interactions with the high-Z nuclei are ex-

tremely effective at stopping electrons and photons, which lose energy through the generation of a cascade of brehmsstrahlung-photon and e^+e^- pair production. These "showers" result in a flash of light that is read out using photodiodes mounted on the backs of the crystals. The energy resolution of the barrel calorimeter is approximately 2% for 2.0 GeV electrons or photons. Hadrons lose energy less quickly in such materials, and their showers extend into the magnet material. Muons deposit only a small fraction of their energy in the calorimeter, and travel through the magnet and beyond.

2.2.4 Magnetic-Field Generation

CLEO's 1.5 T magnetic field is provided by a large superconducting solenoid with a diameter of 3 m and a length of 3.5 m. Cooled with liquid helium, the coil carries a current of 3,500 A and stores 25 MJ of energy. It produces a field that is uniform to $\pm 0.02\%$ over 95% of the tracking volume. The iron flux return for the magnet also serves as part of the absorber for the muon identification system.

2.2.5 Muon Detection

Muons are long-lived particles that do not participate in strong interactions. Because they are much more massive than electrons, they lose energy more slowly and penetrate greater depths of material. The muon detector (MU) exploits this characteristic using gas-filled tracking chambers installed in gaps between 36-cm-thick iron absorbers surrounding the detector (see Fig. 2.4). Two endcaps provide additional

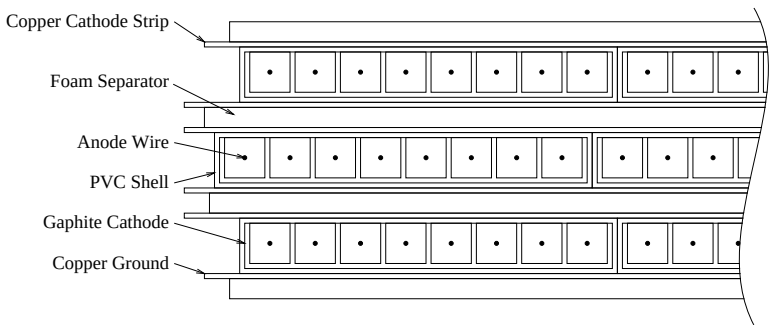

Figure 2.8: A cross section of a muon super-layer

solid-angle coverage.

A MU tracking super-layer is shown in Fig. 2.8. Each super-layer consists of three layers of proportional wire chambers 8.3 cm wide, 1 cm thick, and about 5 m long. Each chamber has eight rectangular cells, each with an anode wire strung along its center. Three of each cell's four walls are coated with graphite and used as cathodes. The fourth has copper strips oriented perpendicularly to the anode wires that provide z information. Chambers in a layer are staggered to eliminate gaps in coverage. The eight anode wires in a counter are ganged together for read-out. Adjacent counters' anode sets are connected through a series of resistors. Muon hits are located using charge division from pulse-height measurments made at each end of a read-out chain. Pulses from the cathode strips provide z information. Averaged over its volume, the muon detector's spatial resolution is about 5 cm.

The muon detector's super-layers provide sensitivity to particles traversing different numbers of "absorption lengths" of material. An absorption length is defined as

the mean distance over which a particle travels before scattering inelastically from a nucleus. The barrel MU super-layers are located at depths of 3, 5 and 7 nuclear absorption lengths. The endcaps each contain one super-layer at a depth of about 7 absorption lengths.

2.3 Data Acquisition

During the CLEO II and II.V experiments, bunch trains crossed at CESR's IP at a rate that rose to 3.5 MHz. The actual rate of interesting physics events was much smaller than this, of order 10 Hz.

CLEO's various detector subsystems include tens of thousands of sensitive elements and associated electronics channels. Each of these can potentially deliver a pulse representing the response of that element to a passing particle. In any given event, only a small subset of all channels have significant data. Nevertheless, read out of the detector requires several milliseconds. During the read out, the experiment is insensitive to new physics events. This makes it essential to read out only interesting physics events.

Fast event discrimination for CLEO II and II.V was achieved with a multiply-tiered trigger system [55, 56] that enabled, disabled, and reset the readout of detector components. This system was designed to efficiently pass higher-multiplicity events involving e^+e^- annihilation into hadrons or τ-pairs. A pre-determined fraction of of Bhabha scatters ($e^+e^- \rightarrow e^+e^-$) and most μ-pair events were kept for use in detector calibration.

The trigger consisted of both hardware and software components. The hardware component had three sequential levels and made use of information from the tracking chambers, TF, and CC to determine if charged or neutral particles had passed through CLEO. Each level used more information and made more sophisticated decisions.

The first and fastest of the hardware triggers was called L0 ("Level-0"). TF counters were grouped into a total of 16 barrel and 14 endcap segments for use by L0. The CC was similarly partitioned into 16 barrel and 16 endcap segments. Anode hits in the VD were grouped by a fast track-segment processor and also used by L0. The patterns in these different detector groups were then used to select interesting events. It took L0 about 300 ns to make a decision. At an instantaneous luminosity of $2.0 \times 10^{32} cm^{-2} s^{-1}$, L0 selected events at a rate of about 10 kHz. If an event passed L0, individual data channel monitors were "latched." That is, sample-and-hold circuits stored their current values until an event either failed a subsequent hardware trigger or was read out. The subsequent hardware triggers, L1 and L2, added DR information to their inputs and had output rates of 100 and 25 Hz, respectively.

Particles generated in collisions generally affected only a fraction of CLEO's many channels. To save storage space, only those channels that registered signals above certain thresholds were recorded. For events passing L2 these channels were assembled, written to disk, and passed through the last component of the trigger system, a software filter known as L3. It ran reconstruction algorithms on the data and used the resulting detailed information to reject additional uninteresting events. It was particularly good at rejecting events in which beam particles interacted with the beam pipe or residual gas atoms. The frequency with which such events occurred depended upon

beam conditions, and L3 could reduce the trigger rate by as much as 50%. Data from events passing L3 were written to tape for later analysis. Overall trigger efficiency for $e^+e^- \to B\bar{B}$ events was over 99%.

2.4 Event Reconstruction

Before the raw data collected from the CLEO II and II.V detectors could be used in analyses, it had to be reduced into quantities of direct physical interest. The many hits in the tracking devices had to be turned into trajectories and momenta, light pulses observed in TF scintillators and CC crystals had to be converted into particle flight times and shower energies, hits in the MU chambers had to be sorted into those likely to be from muons, and so on for each detector subsystem. Momenta, energies, and other quantities were then combined to identify different kinds of particles in the detector and to reconstruct particles which decayed after their production in the e^+e^- collision. All of this was accomplished with a software package called `pass2`.

2.4.1 Track Reconstruction

The most cpu-intensive task performed by `pass2` was track fitting. Raw hit times were first converted into drift distances using tracking-detector calibrations that were precisely determined and closely monitored as data were collected. Pattern-recognition algorithms then grouped hits into track candidates and particle trajectories were fit to these groups of hits [57]. The fits were performed assuming the trajectories were approximately helical, with corrections due to energy loss in material [58]. Multiple

passes through an event's tracking hits were necessary to ensure the most accurate fits. Fit results stored included the helical trajectory parameters (5 total), their errors with correlations, and the residual of the fit, defined as

$$\texttt{RESIDUAL\_RMS} = \left[\sum_i \left(d_i^{obs} - d_i^{fit}\right)^2 / N\right]^{1/2}. \tag{2.4}$$

The sum here is over all non-stereo layers i in the DR, and d_i^{obs} is the measured drift distance for the hit in layer i, d_i^{fit} is the drift distance predicted by the track's helix. N is the total number of degrees of freedom in the fit, a function of the number of DR hits included.

To maximize efficiency, the track-finding algorithm was very inclusive. It sometimes tried to reconstruct tracks using information that was incomplete in some way. For example, when particles emerged close to the beam direction, they included little or no z information from stereo layers or cathodes. The tracks resulting from such fits are known as "z-escapes." Another type of fit made with poor information is known as a "dredge seed." These resulted when, near the end of the track-reconstruction process, the track finder attempted to make a track out of hits not included in other tracks. Such tracks usually have few hits. The track fitter flagged tracks as coming from both of these problematic cases.

Other problematic types of tracks resulted from the confusing arrangement of particles in the tracking volumes. One such type are known as "curlers," and result when a charged particle had sufficiently low momentum that it curled around completely in the drift chamber and traveled back towards the IP. This can result in two (or more) separate track fits: one each for the outgoing and incoming parts of the particle's

trajectory. Sometimes, the hits generated by a single particle traveling away from the IP could be split into multiple tracks. Extra tracks thus generated are known as "ghosts." Examples of both ghosts and curlers are shown in the event display in Fig. 2.9. A separate processor was run after track fitting that attempted to eliminate these and other types of spurious tracks [59].

2.4.2 dE/dx Calculation

The amount of ionization produced in a material by a passing charged particle depends upon its velocity. The integrated charge measurements made for each of the hits used in a track fit were used by `pass2` to estimate the linear density of energy deposition in the DR gas, or specific ionization, dE/dx. This quantity, when combined with a track's measured momentum, can discriminate between particles of different mass.

A variety of systematic detector effects also influenced the amount of ionization deposited in each cell by passing particles. Changes in atmospheric pressure, temperature, and in the gas mixture were all accounted for with time-dependent corrections calculated using Bhabha events. Other effects corrected for include broken wires and variation in electronics gain.

Track-parameter-dependent corrections were also applied to hits used in the dE/dx. These accounted for variation in pulse height due to cell-entry angle, drift distance, magnetic field, and other effects. Once these were applied, the mean charge deposited per cell was calculated. The distribution used in this calculation was truncated to minimize sensitivity to fluctuations in the Landau-like high-side tail. Fig. 2.10 shows a plot of the results for different particle types over a range of momenta. Above $\sim$400

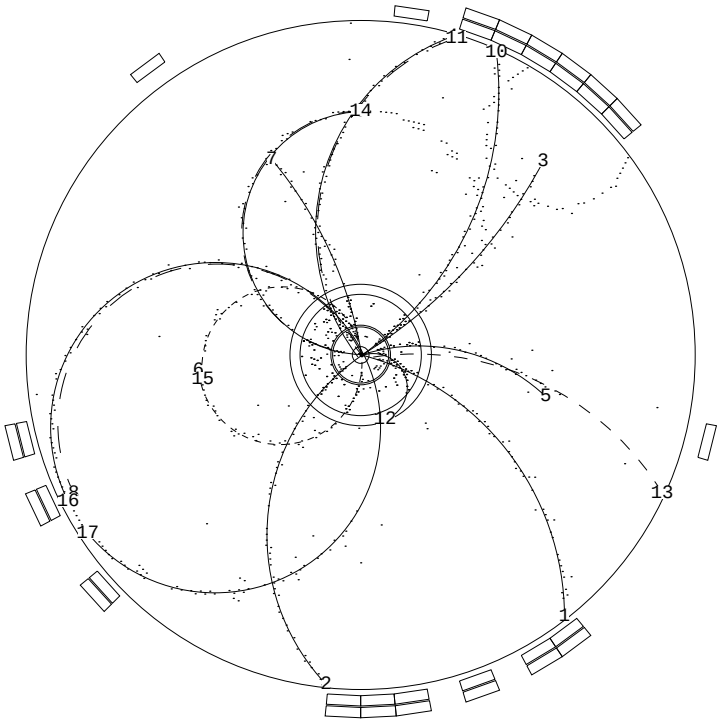

Figure 2.9: A CLEO event display containing examples of curler and ghost tracks. The view is in the r-ϕ plane. Tracking chamber hits are represented by dots, and reconstructed tracks are shown as solid and dashed arcs. The tracks labeled as numbers 16 and 17 are fit to the two halves of a curling particle's trajectory. Tracks 5 and 13 are a "ghost pair," in which the hits from one particle are divided into two separate track fits.

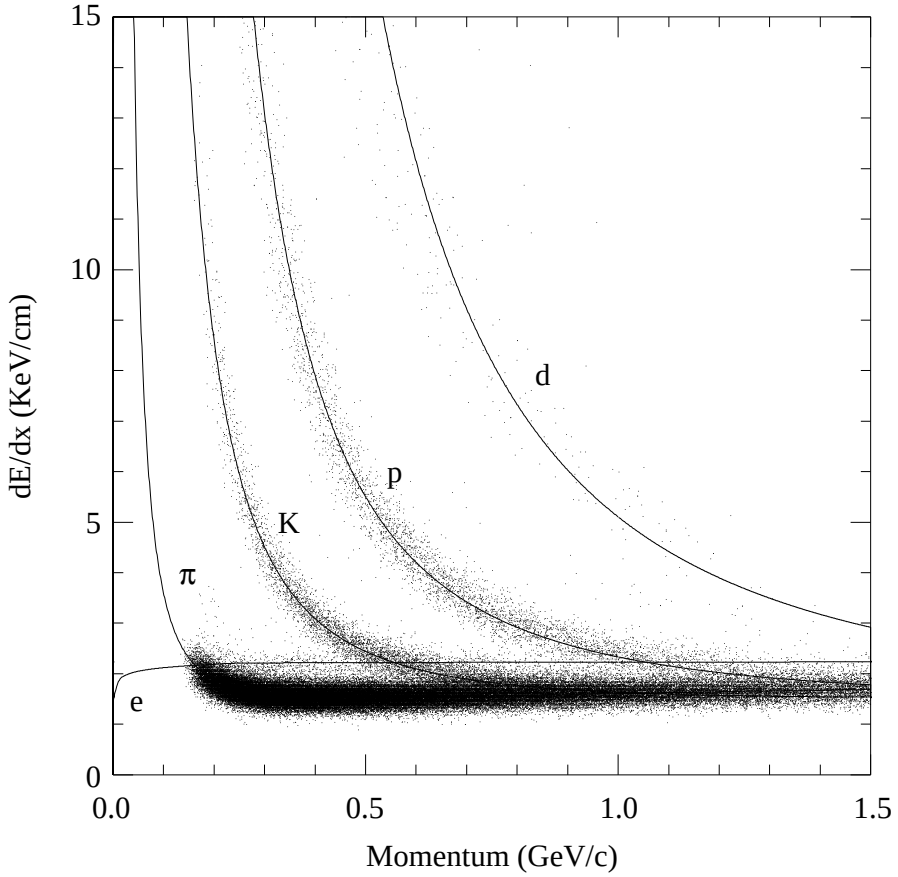

Figure 2.10: Measured dE/dx as a function of momentum. Theoretical curves for various types of particles are shown as solid lines.

MeV/c, calculated specific ionizations provide $\sim 2\sigma$ separation between electrons and pions. Good separation between electrons and protons is possible below $\sim$900 MeV/c.

2.4.3 Time-of-Flight Calculation

The TF provided another means to estimate a partlicle's velocity. Light pulses generated by the passage of charged particles traveled the length of a counter and their

time of arrival at the photomultiplier tubes was recorded. If a reconstructed track was found by `pass2` to have entered the counter, its point of entry and the speed of light in the scintillating plastic were used to compute the particle's time of arrival at the counter. In the barrel section, measurements from a counter's two photomultiplier tubes were averaged. The TF had a time resolution of about 155 ps (220 ps) for hits in the barrel (endcap) counters.

We measure the velocity of a particle relative to the speed of light (i.e. $\beta = v/c$). Fig. 2.11 shows distributions of measured βs for different particle types over a range of momenta. The electron and proton curves remain well-separated up to about 1.6 GeV/c, higher than the 1.1 GeV/c crossing of the corresponding distributions in the dE/dx plot (Fig. 2.10).

2.4.4 CC Shower Reconstruction

Information from CLEO's electromagnetic calorimeter is of crucial importance to the measurement in this thesis. As mentioned in Sec. 2.2.3, electrons deposit most of their energies in the CC's crystals. Therefore, neglecting the small electron mass, the ratio of the energy measured in the calorimeter to the momentum measured in the tracking chambers should be near one for electrons. Heavier particles, which do not initiate electromagnetic showers, should have E/p values less than one.

Showers were reconstructed by first converting the amount of light detected in each crystal into a deposited-energy estimation. Since showers frequently spanned multiple crystals, clusters were formed by grouping neighboring crystals having energies above threshold. The highest-energy crystal in a cluster was required to be at least 10 MeV.

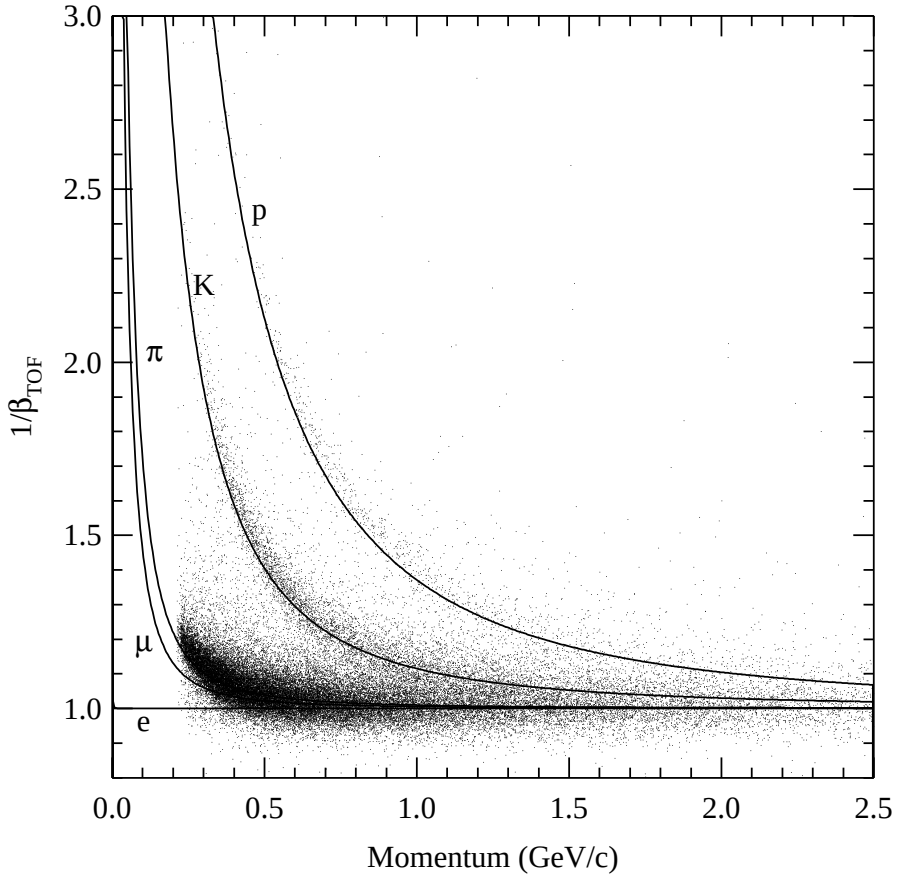

Figure 2.11: Measured times of flight as a function of momentum. Theoretical curves for various types of particles are shown as solid lines.

The position of the shower was then calculated as the energy-weighted mean of all member-crystal positions. The energy and angular resolutions for barrel showers were 3.8% and 11 mrad at 100 MeV, and 1.5% and 3 mrad at 5 GeV. Endcap performance was somewhat degraded by the presence of the DR endplates and electronics in front of the crystals. Showers associated with charged particles were distinquished from photons using loose track-shower matching criteria.

2.4.5 Muon Identification

Muons were identified during event reconstruction by matching hits in the MU chambers to tracks extrapolated from the tracking chambers. At least two of each superlayer's three chambers were required to have registered a hit in order for the layer to be considered. The number of nuclear interaction lengths penetrated by the particle in order to reach the furthest MU chamber registering a matching hit was calculated. Muons need momenta of at least 1.0, 1.4, and 1.8 GeV/c in order to penetrate to depths of three, five, and seven interaction lengths, respectively. The matched track's mometum was used to estimate the depth to which it would have penetrated into the MU chambers if it were a muon, and the absence of any expected hits was noted.

2.4.6 Electron Identification

Electron identification required consideration of multiple quantities and was performed after event reconstruction by software known as the Cornell Electron Identification package (`CEID`). `CEID` examined quantities associated with each track in an

event and calculated a log-likelihood that the track came from an electron. This was stored in a variable named R2ELEC, defined as

$$\texttt{R2ELEC} = \sum_i \ln\left(\frac{P_{ei}}{P_{\not e i}}\right), \tag{2.5}$$

where the sum is over all variables considered. Given a measurement of a particular quantity for a track, P_{ei} is the probability for an electron to have given that value, while $P_{\not e i}$ is the probability that a non-electron would have given that value. The P_{ei} were calculated using variable distributions from radiative Bhabha events, while the $P_{\not e i}$ came from studying tracks from $\Upsilon(1S)$ decays, which contain very few electrons.

Variables considered in the R2ELEC calculation included the track's specific ionization dE/dx, time of flight, track-shower miss distance, the shower's shape and size, and the ratio E/p of the shower's energy to the matching track's momentum. Plots comparing dE/dx and times of flight for electrons to those of other particle types have been shown in Figs. 2.10 and 2.11. Fig. 2.12 shows comparisons between electrons and combined kaon and pion distributions for some of the other variables used by CEID. Of all the variables considered, E/p has the most power to discriminate electrons and hadrons. This quantity is sharply peaked around one for electrons while hadrons have a broader distribution at lower values. The magnitude of the distance separating a candidate shower's center and the point of intersection of the track and CC surface tends to be smaller for electrons than for hadrons. LP2SH, the RMS width of the shower, is more narrowly distributed for electrons. The ratio of the total energy in the shower's innermost 9 crystals to the energy in the innermost 25 crystals is known as $E9/E25$. Since electron showers tended to be confined to narrow regions, this

quantity is more sharply peaked near one for electrons than for hadrons.

2.5 Physics Simulation

The complexity of the CLEO experiments requires the use of sophisticated simulations to understand its response to various physical processes. CLEO's simulation software is based on `GEANT`, a program that simulates the passage of particles through matter [60]. Because it makes use of random number generation to choose among possible outcomes, it is often called a "Monte Carlo" generator.

The CLEO event simulation package, known as `CLEOG`, contains complete descriptions of the various detector configurations used to collect data. These descriptions include material in instrumented volumes, like CsI crystals and cathode traces, and the various support structures and electronics that a particle might have encountered as it moved through the experiment.

Production of a Monte Carlo event begins with the creation of a list of particles created in an e^+e^- interaction. This list includes the 4-momenta of the particles at the time of their creation as well as the momenta of the daughters of any unstable particles generated in the interaction. The list is generated by a program that contains parameterizations of the known and expected physics processes available in e^+e^- interactions at 10 GeV. Whenever possible, its models are constrained by measurements.

Next, `CLEOG` propagates these particles through the detector. At each step, a random number generator is used to determine if a particle interacts with any material

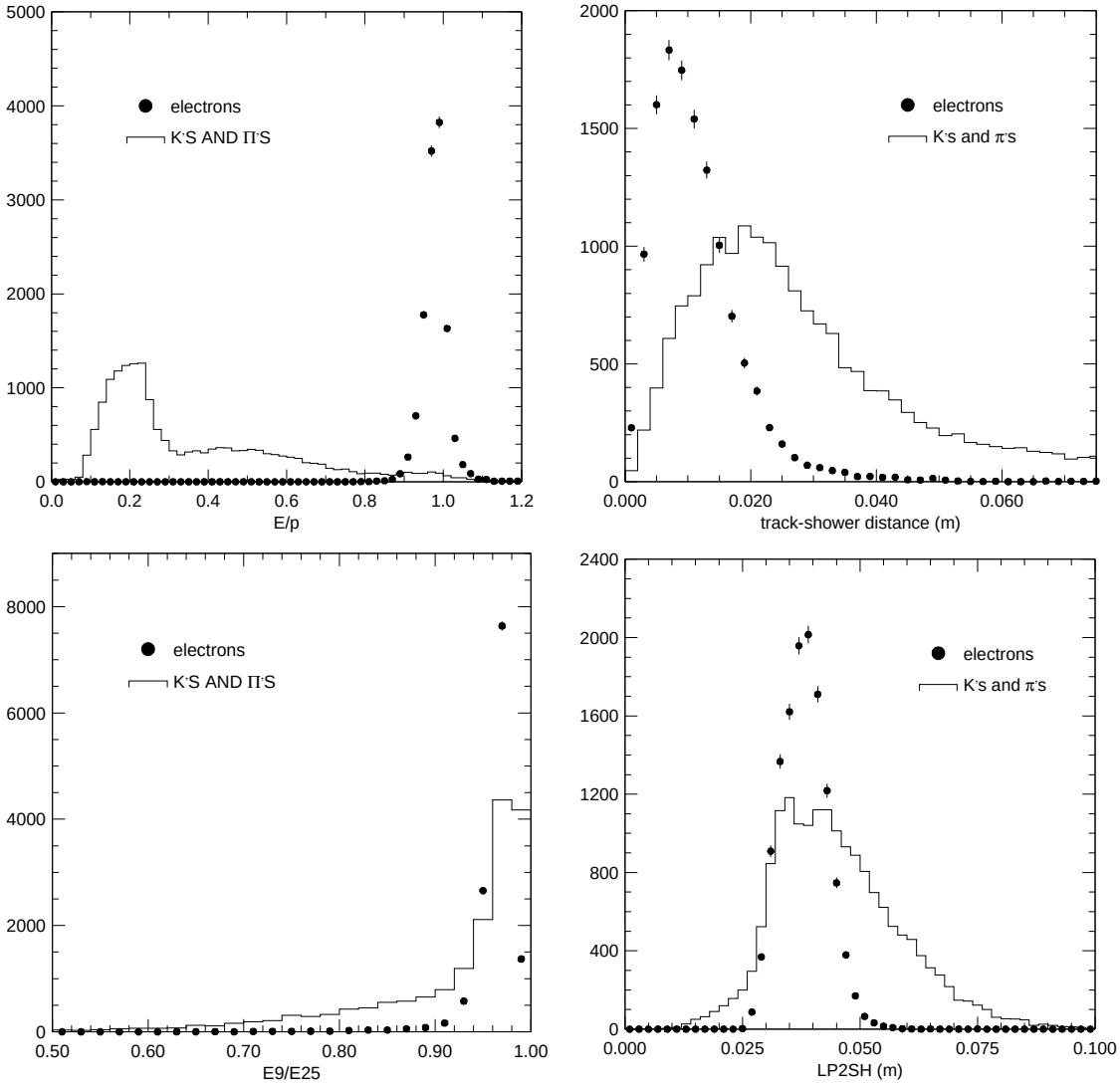

Figure 2.12: Distributions of variables used by `CEID` for electrons and combined pions and kaons. Clockwise from upper left: E/p, track-shower miss distance, `LP2SH`, and $E9/E25$.

it might encounter. If there is an interaction, more random numbers are used to determine its effect on the particle in question. If this interaction occurs in an instrumented volume, the detector's response is also simulated. For the tracking volumes, the distance of closest approach and path length in a given cell are estimated using the particle's trajectory. The cell's response is then simulated using hit efficiencies and charge and drift-distance resolutions measured in data [61]. The limitations of this approach are important for this analysis, and a detailed study comparing tracking efficiency in data and Monte Carlo is discussed in Sect. 3.3.2. Noise in CLEO's various detector systems from electronics and beam-related backgrounds is added to Monte Carlo events using samples of data events taken with a random trigger. Finally, simulated events are put into the same format as raw data so they can be processed by `pass2`.

Fig. 2.13 shows an r-ϕ cross-section of a quandrant of CLEO at $z = 0$. Dashed lines show `GEANT`-propagated particles. Moving clockwise from the left vertical edge of the figure, trajectories are shown for an electron, a muon, a photon, and a pion. Note the many branchings in the e, γ, and π lines in the CC. These correspond to particles created in `GEANT`-simulated interactions in the crystals. Note that some of the particles created in the pion's shower exit the back of the CC and carry on into the flux return.

Large samples of Monte Carlo were produced for use by CLEO's collaborators. For $e^+e^- \to \Upsilon(4S) \to B\bar{B}$ events, the $B\bar{B}$ pairs were decayed using a table that included final states that have been observed and others that are expected theoretically. Whenever possible, experimentally-constrained branching fractions and decay

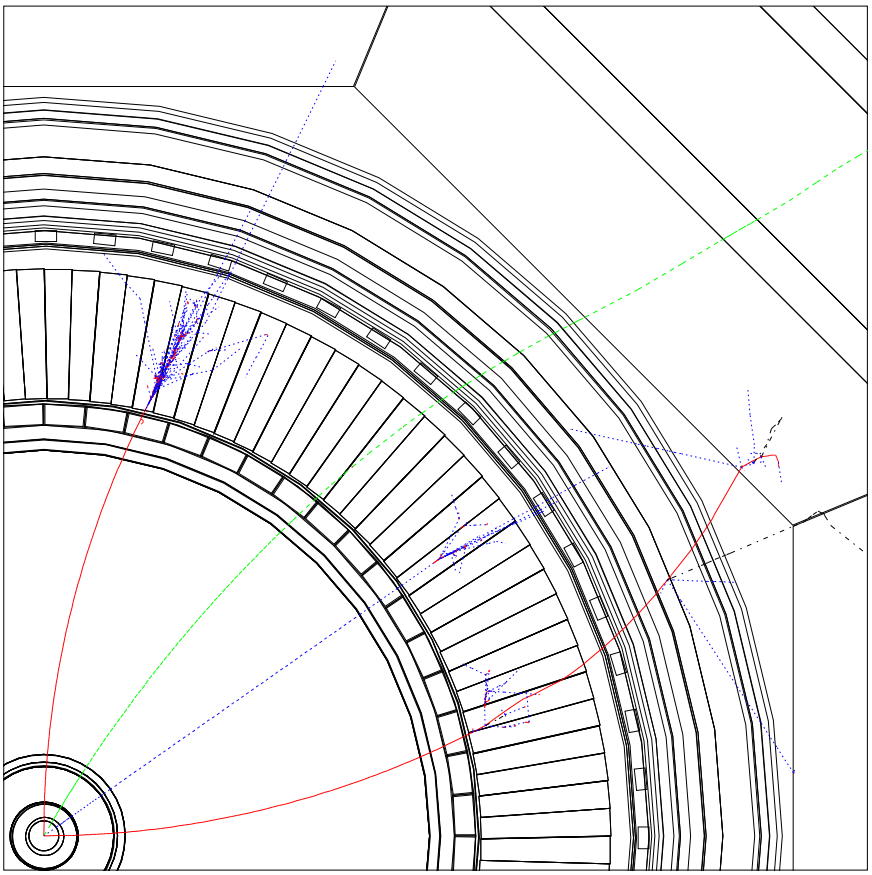

Figure 2.13: Simulated trajectories for particles moving through the CLEO detector. Clockwise from left: an electron, a muon, a photon, and a pion.

distributions were used. If some of a particular particle's decay modes are not experimentally constrained, theoretical predictions were used instead. Several models were used for the semileptonic decays $B \to X_c \ell\nu$. The decays $B \to D^* \ell\nu$ were generated with CLEO-measured HQET form-factor parameters [35], and $B \to D\ell\nu$ was generated with the ISGW2 model. Decays to higher-mass charmed mesons, denoted $B \to D^{**}\ell\nu$, were also generated with the ISGW2 model, and nonresonant $B \to D/D^* X\ell\nu$ were described by the model of Goity and Roberts [62].

Samples of non-$B\bar{B}$ Monte Carlo were also generated using a variety of models. Lighter $q\bar{q}$ pairs produced from e^+e^- annihilations were fragmented into hadrons using the JETSET package from the European Center for Nuclear Research (CERN) [63]. Electron- and muon-pair events were generated according the results of explicit QED calculations. Tau pairs were produced using the KORALB package [64].

CHAPTER 3

Analysis Procedure

3.1 Data Sample

This analysis was performed on data collected with both the CLEO II and II.V detector configurations. We collected 3.14 fb^{-1} of ON data and 1.61 fb^{-1} of OFF data with the CLEO II detector between 1990 and 1995. After a seven-month shutdown, we collected 5.99 fb^{-1} of ON data and 2.74 fb^{-1} of OFF data with the CLEO II.V detector. The total data sample thus includes 9.13 fb^{-1} of ON data and 4.35 fb^{-1} of OFF data. ON beam energies range from 5.285 to 5.295 GeV, while OFF beam energies vary from 5.188 to 5.275 GeV.

OFF data was used to subtract continuum background not removed by the application of signal-selection criteria. Prior to the subtraction, OFF events passing signal criteria were scaled by a factor α that accounts for the difference in luminosity and the continuum-production cross-section between the ON and OFF data samples. It was computed as

$$\alpha = \frac{\mathcal{L}_{ON}}{\mathcal{L}_{OFF}} \times \frac{E_{OFF}^2}{E_{ON}^2}, \tag{3.1}$$

where $\mathcal{L}_{ON}$ and $\mathcal{L}_{OFF}$ are the ON and OFF luminosities, while E_{ON} and E_{OFF} are the luminosity-averaged beam energies. This approach gave $\alpha_{II} = 1.931$ and $\alpha_{II.V} =$

2.156 for the CLEO II and CLEO II.V samples, respectively. In previous CLEO analyses, this scale factor was given a fractional error of 1% and its reasonableness was verified independently by measuring the continuum-subtracted yields for leptons above the end point [65]. We performed a similar study on the current data by measuring the yield of 3 to 3.5 GeV/c tracks passing all of the selection criteria described in Sect. 3.2, with the exception of lepton-identification and continuum-suppression requirements. In the ON sample, tracks in this momentum interval cannot come from $B\bar{B}$ decays, so the measured continuum-subtracted yield should be zero. For CLEO II data, the resulting yield is -490 ± 737, consistent with zero as expected. CLEO II.V looks problematic, however, with a negative yield of -3928 ± 1073.

The ratio of high-momentum track yields, as an alternative measure of the scale factor, is $\alpha_{II.V} = 2.133$, slightly more than 1% smaller than the computed value. To search for systematic effects that might contribute to this discrepancy, we tried varying some of the event-selection criteria. We found that the ratio of track yields has little sensitivity to our requirements on event shape and the z-projection of a track's distance of closest approach to the event's primary vertex. The measured value of α does show a dependence on the track-multiplicity requirement, however, an effect seen in both CLEO II and II.V data. Since we use the scale factor in the subtraction of track spectra, we decided to adopt the value of $\alpha_{II.V}$ measured with our final selection criteria as appropriate for our analysis. We include a 1% systematic error on both scale factors, as this accounts for the difference between the calculated and measured values of $\alpha_{II.V}$. We have verified that values of α measured with tracks passing our lepton-identification requirements (see Sect. 3.2.4) are consistent with the

values we quote here.

Note that the small uncertainty in the CLEO II.V scaling factor is only important when our analysis is performed without continuum suppression. Our continuum-suppression procedure (see Sect. 3.2.5) reduces the continuum background enough that subtracted yields computed with either scale factor differ by a negligible amount.

3.2 Event Selection

3.2.1 General Event Requirements

Event selection was based on a set of requirements, or *cuts*, designed to eliminate obviously non-hadronic events. These included requirements on an event's charged-particle multiplicity, visible energy, and event-vertex position [66]. The event vertex is the point in an event that is closest to the largest number of tracks. It was required to be within 2 cm of the IP in the x and y directions, and 7.5 cm in the z direction. At least three separate tracks were required in the event. Pairs of tracks found to have both come from a point displaced from the IP were assumed to have originated from the same parent particle and were counted as one track. The sum of the energies of all charged and neutral particles in the event was required to be at least 15% of the center-of-mass energy. Also, the total energy observed in the calorimeter was required to be between 15% and 90% of the center-of-mass energy. Together, these requirements were found to be more than 99% efficient for simulated $B\bar{B}$ events.

Because our signal events include the production of a neutrino, not all of the available center-of-mass energy should be visible in the detector. We therefore added

to the above event-selection criteria the loose requirement that the total visible energy be less than the center-of-mass energy.

3.2.2 Event Multiplicity

On average, $B\bar{B}$ events have higher multiplicities than backgrounds like Bhabha, μ-pair, and τ-pair events. Therefore, we applied an overall track- and shower-multiplicity requirement when selecting signal candidates.

While counting tracks and showers, we used selection criteria to distinguish real particles from spurious ones, and to avoid over-counting curlers and showers matched to tracks. Tracks and showers passing these criteria will hereafter be referred to as *global* particles.

Global tracks were required to pass criteria ensuring that they were not ghosts or curlers, they did not come from dredge seeds, and they were not z-escapes.

In addition, they were required to pass three of the following four cuts that ensure good fits to hits produced by particles originating at the IP:

- $\texttt{RESIDUAL\_RMS} \leq 1$ mm
- DR hit fraction $\geq 30\%$
- $|\texttt{DBKL}| \leq 5$ mm
- $|\texttt{ZOKL} - \texttt{IP(3)}| \leq 5$ cm

Here RESIDUAL_RMS is the residual of the fit, as defined in Sect. 2.4.1, and the DR hit fraction is defined as the ratio of DR hits found on a track to the number expected

given its reconstructed trajectory. The quantities DBKL and Z0KL are impact parameters. Z0KL is the z coordinate of the track's point of closest approach to the beam axis, and DBKL is the distance in the r-ϕ plane between this point of closest approach and the beam axis. Since the location of the beam-crossing point varies somewhat with time, we cut on the difference between Z0KL and the z coordinate of the event's vertex, IP(3).

Tracks from secondary decay vertices typically have larger impact parameters. For this reason, such tracks were required to pass only the first three requirements and the RESIDUAL_RMS cut.

Global showers were selected from a list of CC clusters that were not matched to any track and were required to pass the following cuts:

- Shower Energy ≥ 50 MeV
- $|\cos\theta| \leq 0.90$

Given the above definitions of global particles, we designed minimum event-multiplicity requirements using samples of τ-pair and ISGW2 $B \to X_u \ell\nu$ Monte Carlo. Both samples were required to have a generated lepton with at least 1.4 GeV/c of momentum, and to have passed the basic hadronic event-selection criteria discussed above. Charged and neutral multiplicity distributions from each sample are shown in Fig. 3.1. We found that a multiplicity requirement of at least five global tracks, or four global tracks with at least six global showers rejects over 94% of the τ-pair events, while it keeps 93% of the $B \to X_u \ell\nu$ sample.

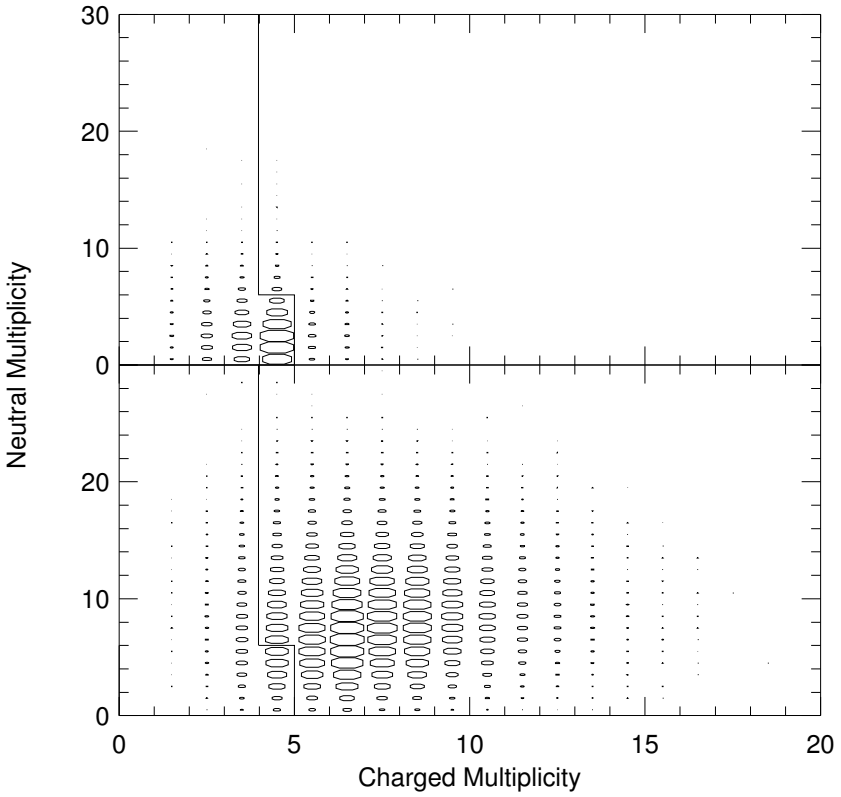

Figure 3.1: Charged and neutral multiplicities for τ-pair (top) and ISGW2 signal (bottom) Monte Carlo. The lines in each plot show the multiplicity cut boundary.

3.2.3 Signal-Track Selection

Because of our signal's proximity to the kinematic limit for leptons from charmed semileptonic B decays, it is critical that we only consider well-reconstructed tracks. Errors in track reconstruction could "smear" leptons from $B \to X_c \ell \nu$ decays into our signal region. We therefore required a more stringent set of track-quality cuts for signal-lepton candidates.

These new cuts were chosen using a sample of $B \to X_c \ell \nu$ Monte Carlo events from CLEO's $B\bar{B}$ Monte Carlo (see Sect. 2.5). Tracks coming from generated leptons from B decays were divided into two groups. The first group, *good* tracks, had reconstructed momenta differing in magnitude from their generated momenta by less than 1%. *Bad* tracks' generated and reconstructed momenta differed by more than 2%. Cut values for different track parameters were chosen to reject bad tracks with minimal impact on good tracks. To ensure that we are not relying too much on any one of the cut variables, the effect of all of the cuts was compared to those of the sets of cuts with one variable removed from consideration.

Signal tracks were required to pass global track-quality cuts. The following criteria were also applied:

- $|\cos\theta| \leq 0.7071$ ("Good Barrel")
- `RESIDUAL_RMS` ≤ 0.5 mm
- $|$`DBKL`$| \leq 2$ mm
- DR hit fraction $\geq 50\%$

- Not associated with a reconstructed displaced vertex

The impact of these cuts on mismeasured tracks near the $B \to X_c \ell \nu$ end point is shown in Fig. 3.2. Over 99% of tracks having reconstructed momenta smeared beyond the kinematic end point fail our track-quality cuts.

3.2.4 Lepton Identification

Signal-track candidates were subjected to a set of lepton-identification requirements to reject hadronic tracks. For electrons, we used the CEID package with a requirement of `R2ELEC` ≥ 3.0 (Sect. 2.4.6).

For muons, we required that the track penetrated at least seven interaction lengths of absorber material. In addition, we required that the muon identification package found no expected hits missing at penetration depths less than the maximum reached.

Tracks that were identified as both electrons and muons ($\sim$0.1%) were counted as electrons. This procedure was based on a study [67] that found a measurable rate for electrons to fake muons through matches between an electron track and random hits in the muon chambers. Muons, on the other hand, are unlikely to fake electrons given the use of dE/dx and E/p in electron identification.

We studied the stability of these requirements by calculating the continuum-subtracted lepton yields, normalized to the number of $B\bar{B}$ events in data. Fig. 3.3 shows this normalized yield for 15 chronologically-ordered time intervals throughout CLEO II and II.V data-taking. We found that lepton yields are mostly consistent across all of the data. However, electron yields in two blocks taken early in

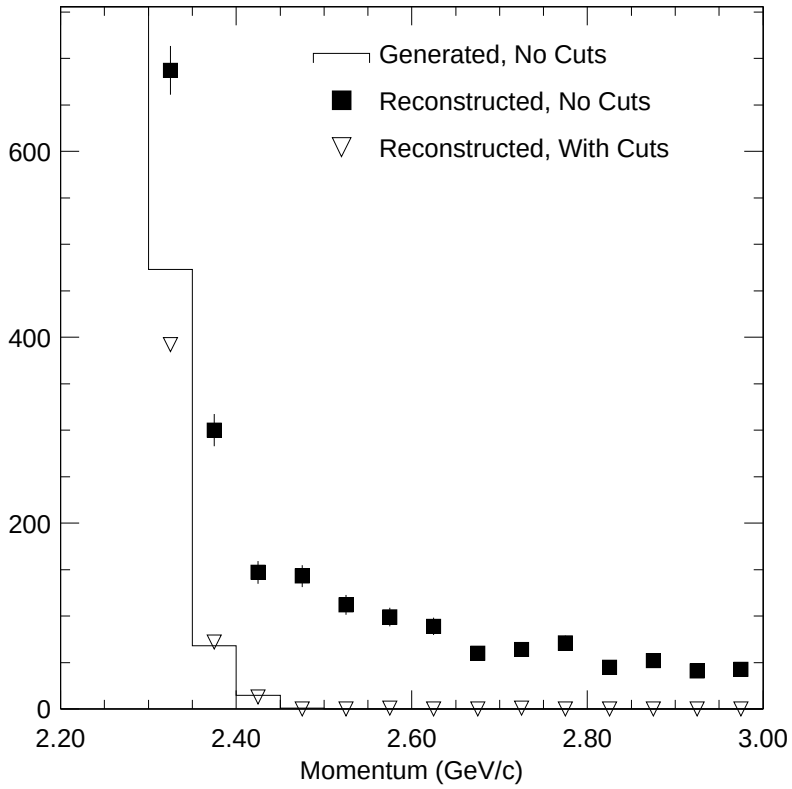

Figure 3.2: The effect of signal track-quality cuts on the reconstructed momentum spectrum around the end point for $B \to X_c \ell \nu$ transitions. The solid histogram shows the generated lepton momentum spectrum in generic $B\bar{B}$ Monte Carlo. The reconstructed spectrum, without tight track-quality cuts, is shown in solid squares, while the spectrum of tracks remaining after cuts is in empty triangles.

CLEO II.V are around 10% lower than those found in other blocks, an effect not seen in the muons. Electron-identification studies made with samples of embedded radiative Bhabha events (see Sect. 3.3.3) did not indicate a lower efficiency for these data blocks. While we do not understand this discrepancy in yields, we note that these blocks together make up about 10% of our ON data, which means that the effect is of order 1% for electrons, or 0.5% for all leptons. Given that we have more significant sources of uncertainty, we included this data in our analysis without addressing this issue further.

3.2.5 Continuum Suppression

Non-$B\bar{B}$ events at the $\Upsilon(4S)$ can yield leptons with momenta consistent with those from the $B \to X_u \ell \nu$ end point. Although the cuts discussed so far eliminate lower-multiplicity events, continuum processes like $e^+e^- \to c\bar{c}$ still present a potentially overwhelming background. In fact, the ratio of $B\bar{B}$ to continuum events in the end-point region is on the order of one to ten. OFF data can be used to subtract continuum background from an ON momentum spectrum, but the resulting yield will have a large statistical uncertainty. We therefore must eliminate continuum events from our sample prior to the subtraction of OFF data.

The quarks produced in a $c\bar{c}$ event have significant boost. Hadronization then yields events in which particles coming from each quark tend to be collimated in back-to-back "jets." B Mesons in $B\bar{B}$ events are produced nearly at rest and decay almost isotropically in the lab frame. We exploited this topological difference to suppress continuum background events.

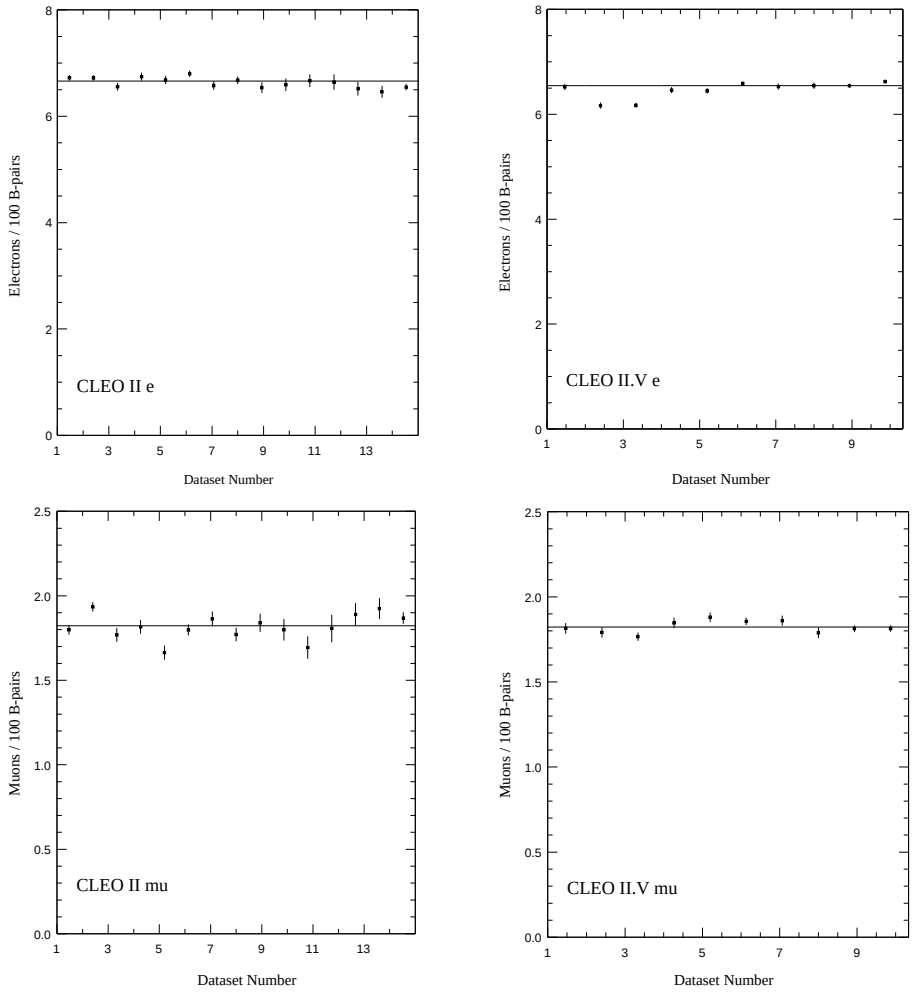

Figure 3.3: Continuum-subtracted electron yields (top plots) and muon yields (bottom plots) in the momentum interval from 1.5 to 2.2 GeV/c for the CLEO II (left plots) and II.V (right plots) data. Each point represents a contiguous block of data. In each figure, the solid line indicates the result of a fit of a constant to the points. The first two data blocks were excluded from the fit to CLEO II.V electron points. The vertical scales of all the plots are lepton yield per 100 $B\bar{B}$ events.

In constructing a variable that discriminates between events of different topologies, we took inspiration from the "virtual calorimeter" used in previous CLEO rare B analyses [68]. In this approach, one defines an axis for the event and then constructs a set of nested cones, each with its apex at the interaction point, opening about this axis. The energies of tracks and unmatched showers pointing into the volume between consecutive cones are summed. In our case, the high-momentum lepton's momentum vector provided a suitable axis, and we used separate sets of cones opening along and against the lepton's direction. A diagram of this arrangement is shown in Fig. 3.4.

We expect continuum events to have more of their visible energy flowing into the shells near the lepton's momentum vector, while the energy in $B\bar{B}$ events should be more uniformly distributed. Monte Carlo studies were consistent with this expectation. We used a sample of continuum Monte Carlo and signal events simulated with the ISGW2 model to study these variables. We defined forty conic shells, twenty in the forward direction and twenty in the backward direction, each covering uniform steps of 0.05 in $\cos\theta$. Fig. 3.5 shows the energy, *averaged over many events*, flowing into each of the shells for both of our Monte Carlo samples.

We sought a method to combine these variables that would allow us to accept an event as signal-like or reject it as likely background. A neural net provided a semi-automated way to choose such a combination. A trained neural network is nothing more than a function that divides a variable space with a decision surface and outputs a number that depends on an input vector's relation to that decision surface.

The type of net that we have chosen is known as a *feed-forward multilayer perceptron* [69]. It is formed by several layers of *neurons*, or *nodes*, which compute a linear

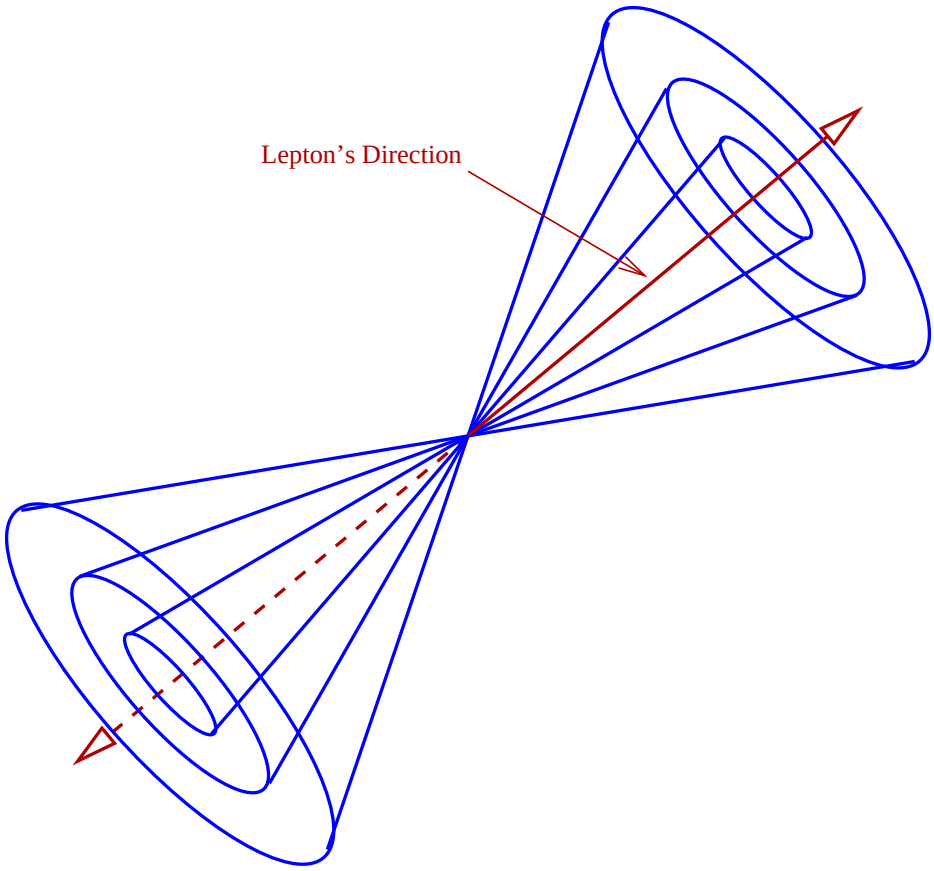

Figure 3.4: A diagram of our virtual calorimeter.

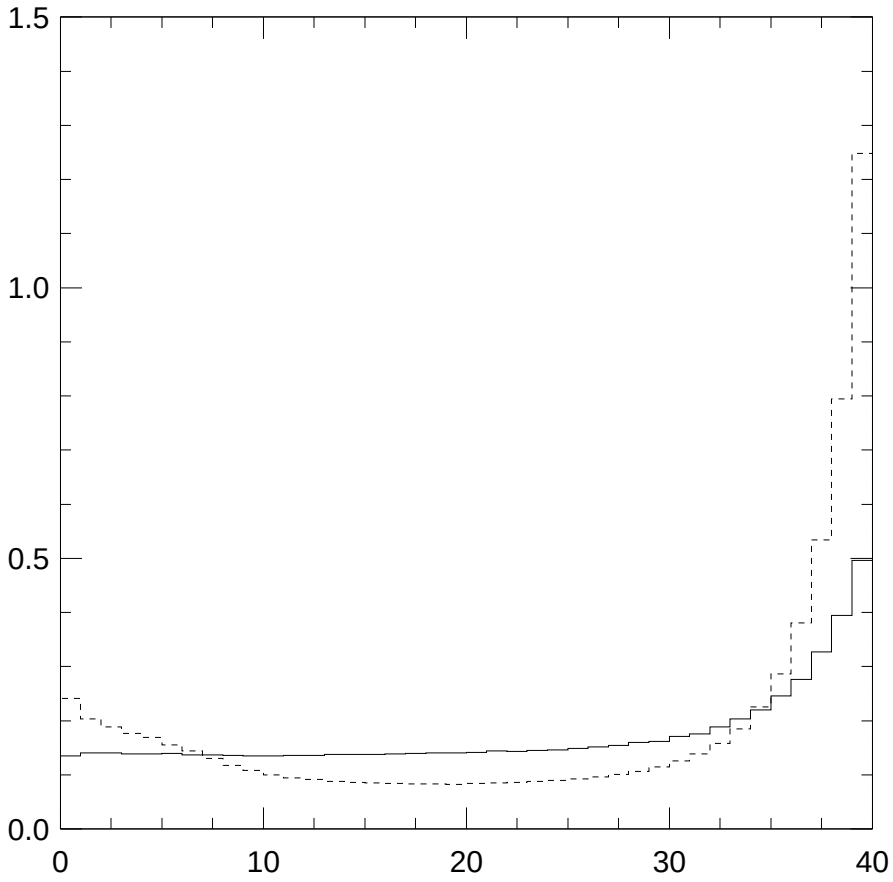

Figure 3.5: Plots of *average* energy flow into conic shells opening about the lepton's direction for continuum (dashed histogram) and ISGW2 signal (solid histogram) Monte Carlo. The horizontal axis shows the bin number, with the first bin corresponding to the cone opening about the lepton's momentum vector and the last bin's cone opening in the opposite direction.

combination x of the outputs of the previous layer's nodes and then feed the result into the *activation function* $g(x)$. The resulting number is fed forward, along with the outputs of all the other nodes in the layer, to the neurons in the next layer. Fig. 3.6 shows a schematic of our neural net. It has three layers: the input nodes x_i, a hidden layer of nodes h_j, and an output node y. The input nodes take the values of each of the variables used to discriminate signal from background. These are then passed through the net in the process described above. Each hidden node then outputs a value given by

$$h_j = g(\sum_i w_{ij} x_i + \theta_j). \tag{3.2}$$

The output node uses the results to compute the value

$$y = g(\sum_j w_{jy} h_j + \theta_y). \tag{3.3}$$

Here w_{ij} and w_{jk}, the *weights*, are fitted from the data distributions.

A plot of our activation function

$$g(x) = (1 + e^{-2x})^{-1}, \tag{3.4}$$

is shown in Fig. 3.7. It outputs a value near zero for arguments sufficiently below zero, and a value near one for sufficiently positive arguments. In this way, the hidden nodes divide the variable space into *hyperplanes* which collectively form a decision surface dividing input events into two groups.

The process of selecting a net's weights is known as *training*. We've employed a method called *back propagation*. Here one begins with a random set of weights and then calculates the net's output for events selected from known signal and background

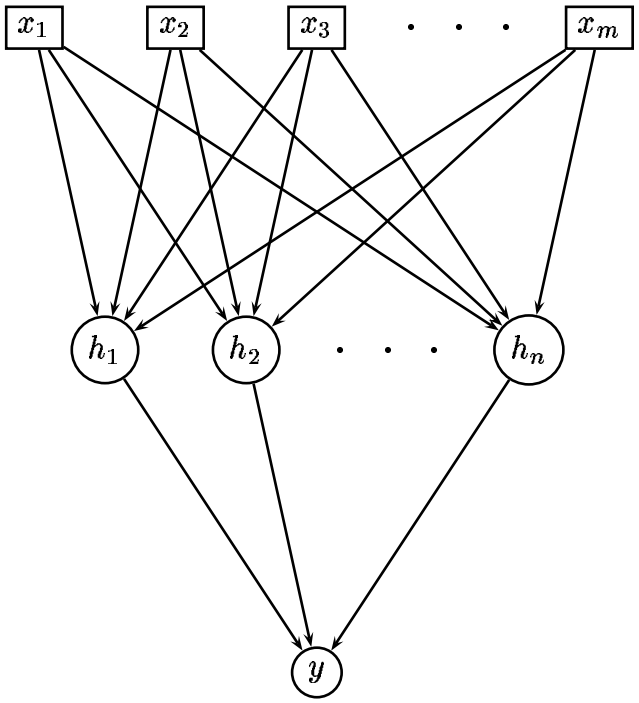

Figure 3.6: A diagram of our neural net: x_i are the inputs, h_j the hidden nodes, and y is the ouput.

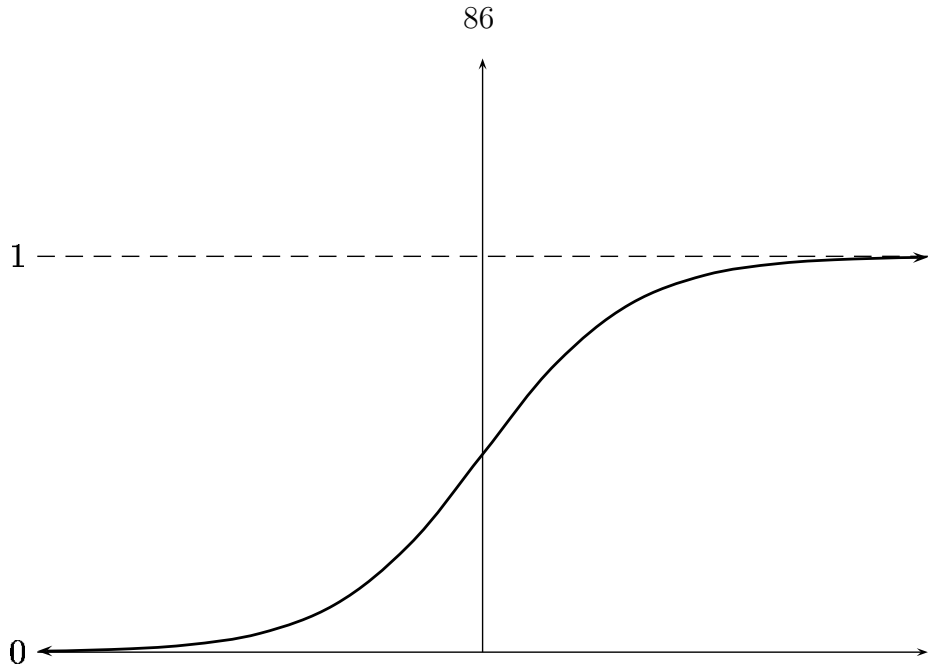

Figure 3.7: The activation function used by our net.

samples. Since the desired answer t is known (say 0 for background events and 1 for signal events), one can use the difference between it and the actual output y to correct the weights. For every N events, an *epoch*, an error is calculated:

$$E = \frac{1}{N} \sum_{p=1}^{N} (y_p - t_p)^2. \tag{3.5}$$

Each weight vector is then updated according to the rule

$$w_{t+1} = w_t + \Delta w_t, \tag{3.6}$$

where

$$\Delta w_t = -\eta \frac{\partial E}{\partial w}. \tag{3.7}$$

Here η is the *learning rate*, which is reduced at each epoch as training progresses to facilitate convergence.

Training samples were chosen from continuum Monte Carlo and $B \to X_u \ell \nu$ signal events simulated with ISGW2. The multiplicity, track-quality, and lepton-identification requirements outlined in Sect. 3.2 were applied and samples of 140,000 signal and 130,000 background events were selected. To limit the number of inputs (and therefore the number of weights to train), the energy cone variables of Fig. 3.5 were combined where there was little relative change from cone to cone. We constructed a total of 12 cones by grouping the 10 forward-most and 10 backward-most cones by twos, and dividing the middle 20 cones into two groups of 10 each. Note that both distributions in Fig. 3.5 are relatively flat in the middle. This observation motivated the large consolidated cones used in this region.

We had several considerations in mind while designing our net. Of course, we wanted to maximize the significance of a measured excess in the end-point lepton spectrum. In addition, we sought to limit the dependence of the efficiency of a neural-net cut on the features of a particular model for $B \to X_u \ell \nu$, such as the distribution of $q^2 = (p_\ell + p_\nu)^2$ (the squared mass of the virtual W).

We know that low q^2 signal events, in which the hadronic daughter system X_u recoils hard against the lepton-neutrino pair, are the most continuum-like topologically. Therefore, a net trained to reject continuum events using our cone variables will likely also reject low-q^2 signal events. We determined that this effect can be limited by eliminating the backwardmost consolidated cone from our net's consideration. The output of the resulting net, trained on 11 energy-cone variables, is shown in Fig. 3.8.

To optimize the cut on this net, we used as our figure of merit the statistical significance of an expected $B \to X_u \ell \nu$ signal. Given the effectiveness of the net in

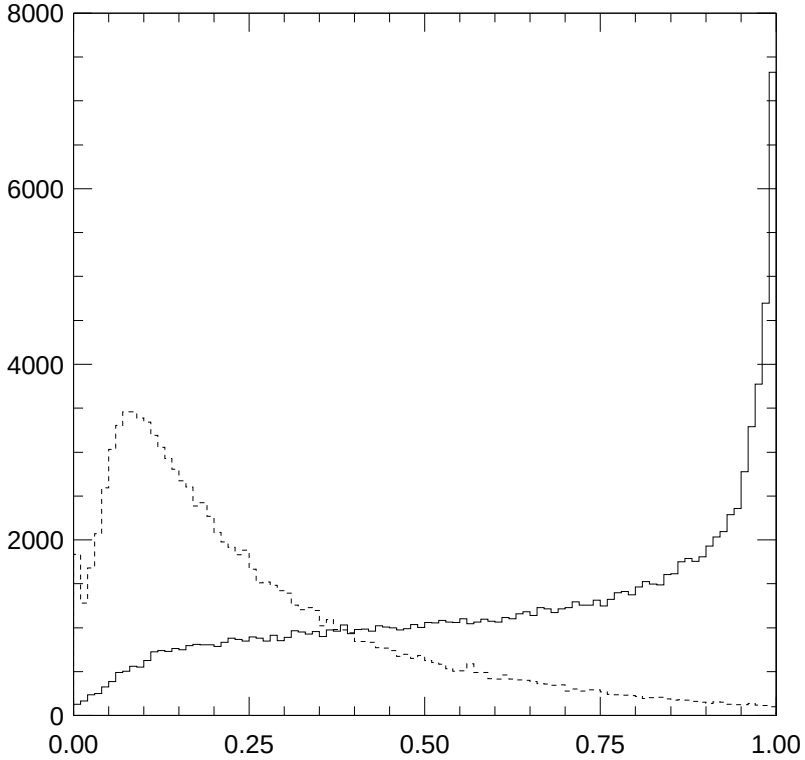

Figure 3.8: The output of the 11-cone net for continuum (dashed histogram) and ISGW2 signal (solid histogram) Monte Carlo.

suppressing continuum, the ON sample remaining after a cut should be dominated by signal events. If we let T be the total number of leptons (signal and background) in our ON data sample, while B is the number of leptons in the OFF sample passing our cuts, then the number of signal leptons in the ON sample, S, is

$$S = T - \alpha B, \tag{3.8}$$

where α is the ON-OFF scale factor. The fractional error in our continuum-subtracted signal yield is then

$$\frac{\Delta S}{S} = \frac{\sqrt{(S + \alpha B) + \alpha^2 B}}{S}. \tag{3.9}$$

Since $\alpha \approx 2$, we need to choose a cut that maximizes the figure of merit:

$$\mathcal{F} = \frac{S^2}{(S + 6B)}. \tag{3.10}$$

Fig. 3.9 shows the results of the cut optimization. We used subsamples of our Monte Carlo containing leptons of momenta from 2.4 to 2.6 GeV/c. Their normalizations were chosen using scaled, efficiency-corrected, yields from the previous CLEO end-point analysis [65]. The optimum cut is at 0.84, but the peak is broad so we chose 0.80 to preserve signal efficiency.

In evaluating this net, we compared its performance to a number of nets using different sets of input variables and assorted architectures. We varied the number of consolidated energy cones, tried removing different segments of the event from the net's consideration, and added additional variables like R_2 (defined below) as inputs. The nets were all trained on the same Monte Carlo samples, and compared using S^2/B as an approximate figure of merit. Efficiencies were calculated by running the

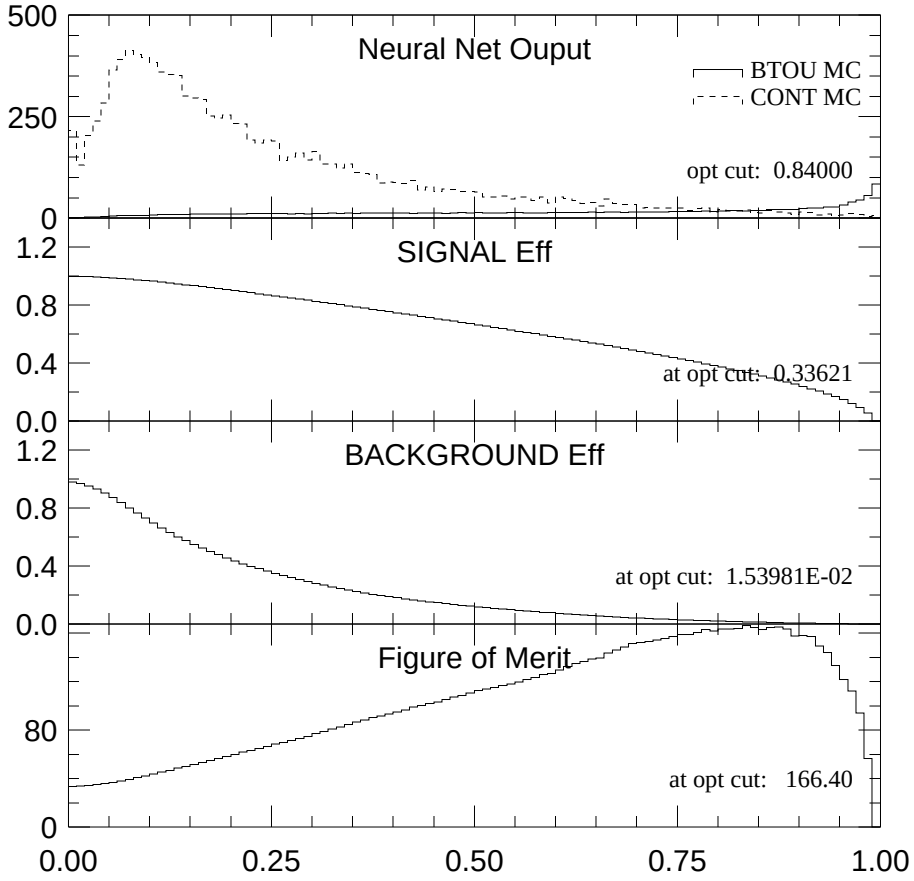

Figure 3.9: Optimization of our neural-net cut. The x axis is the net's output, ranging from 0 to 1. The top plot shows histograms of the net's output for signal (BTOU) and continuum (CONT) Monte Carlo. Efficiencies versus cut values are in the middle two plots, and the bottom plot shows how the figure of merit varies with cut value.

nets on Monte Carlo samples independent of the samples used in training. We found that our 11-cone net has the best combined performance in terms of signal efficiency and minimal q^2-dependence.

In addition to neural nets, we explored using more traditional shape variables like R_2. R_2 is defined as a ratio of Fox-Wolfram moments [70] H_2/H_0, where

$$H_k = \frac{1}{s}\sum_{i=1}^{n}\sum_{j=1}^{n}\left[|\overrightarrow{p_i}||\overrightarrow{p_j}|P_k(cos\phi_{ij})\right].$$

Here n is the number of particles, s is the center-of-mass energy squared, ϕ_{ij} is the angle between the momentum vectors for particles i and j, and P_k is a kth order Legendre polynomial. $B\bar{B}$ events have R_2 values near zero, while continuum events have higher values. We picked an optimum cut on R_2 by following the same procedure used in the net cut's optimization. We found that the net cut showed better all around performance. The R_2 cut has a signal efficiency of 44.6%, somewhat higher than the net cut's 33.6%. However, the background efficiency is also higher for the R_2 cut (3.8% versus 1.5%), so that the R_2 cut's overall figure of merit is 152.9, slightly worse than the net cut's 166.4. Fig. 3.10 shows the dependence of the signal efficiency of both cuts on q^2. The R_2 cut's efficiency has about three times more fractional variation over the q^2 range spanned by our signal events.

We expect that different theoretical models for $B \to X_u\ell\nu$ decays might populate the hadronic recoil-mass spectrum differently. To check for sensitivity to this variable, we binned events in our ISGW2 Monte Carlo according to X_u mass. We grouped the 25 different exclusive hadronic modes into four bins and then computed the efficiency of our net cut on the sample in each mass bin. Table 3.1 summarizes the results,

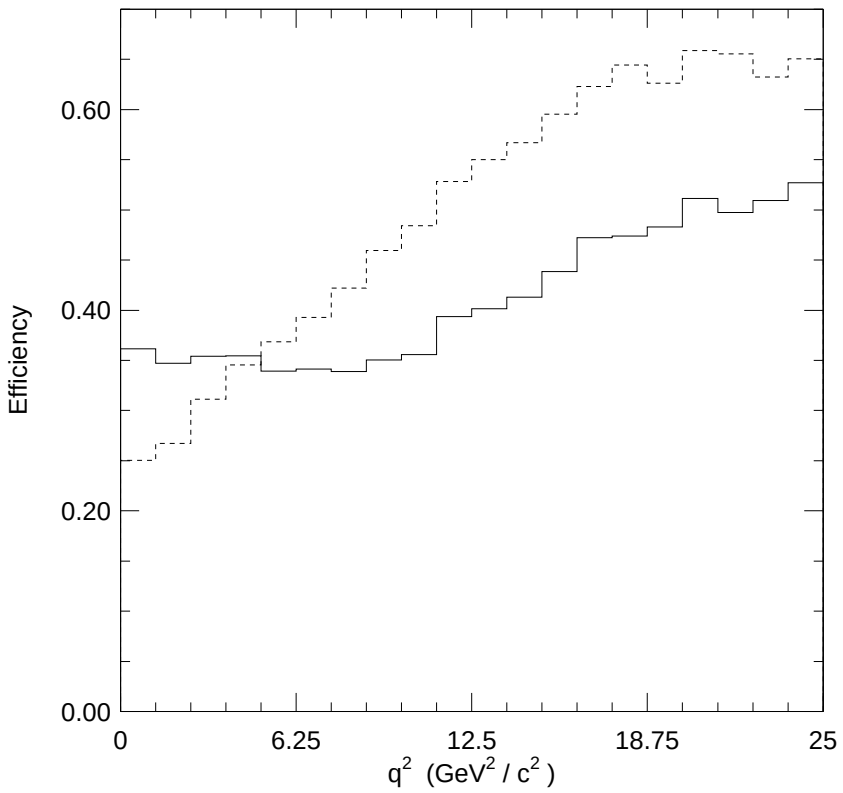

Figure 3.10: Cut efficiency versus q^2 for the neural-net cut (solid) and a similarly optimized R_2 cut (dashed). While the average efficiency of the R_2 cut is higher, it has a larger fractional variation than the net cut.

Table 3.1: The efficiency of our neural-net cut when applied to ISGW2 Monte Carlo signal events grouped by X_u mass.

Mode	X_u Mass (MeV/c^2)	ϵ_S (%)
All	130 - 1500	21.4
1	130 - 550	21.9
2	770 - 780	21.6
3	950 - 1250	20.7
4	1250 - 1500	21.0

demonstrating that the net cut is insensitive to X_u mass.

To test the stability of our net's behavior across our data, we computed the continuum-subtracted spectra of net ouputs for events with leptons having momenta between 1.5 and 2.2 GeV/c. Fig. 3.11 shows separate sets of overlaid CLEO II and II.V plots for electrons and muons satisfying our selection criteria. All spectra have been normalized to the same area. There is no discernible difference between the shapes of the spectra in the two sets of data.

3.2.6 Other Continuum Background

QED processes can also contribute background to our analysis. Examples include $e^+e^- \to \gamma e^+e^-$ with additional spurious or beam-related particles, and two-photon events: $e^+e^- \to e^+e^-\gamma^*\gamma^* \to e^+e^- hadrons$. Such events frequently result in the scattering of one beam particle into the detector's acceptance with the other continuing

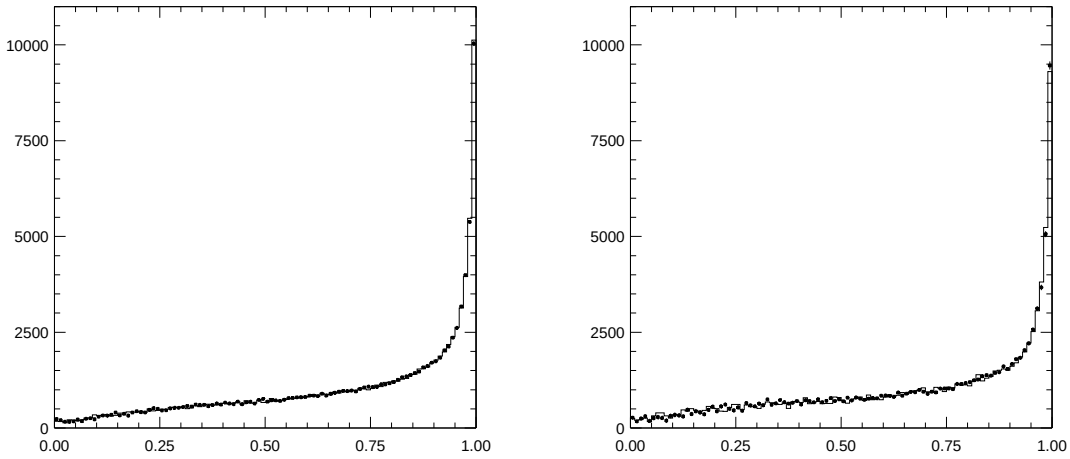

Figure 3.11: Continuum-subtracted spectra of neural-net outputs for events containing signal-quality electrons (left) and muons (right) in the momentum interval from 1.5 to 2.2 GeV/c. CLEO II data are shown with solid histograms, and CLEO II.V data are plotted with dots. All spectra are normalized to the same area.

down the beam pipe. It was previously found that a cut on missing momentum is useful in suppressing these backgrounds [65].

We investigated this idea using leptons with momenta between 3.0 and 3.5 GeV/c. These leptons have energies sufficiently above the $B \to X_u \ell \nu$ end point that we can be confident they are from the continuum. Fig. 3.12 shows histograms of the direction cosines of the missing momenta ($\cos\theta_{P_{miss}}$) in events containing high-momentum electrons passing all of our cuts. Since the lab is in the center-of-mass frame, we calculated each event's missing momentum as the inverse of the sum of all detected particles' three momenta. The large peaks show beam correlation. That is, if the detected particle is an e^-, the missing momentum peaks in the negative z direction - the direction that the beam's positrons travel. Peaking occurs in the opposite direction if the detected particle is an e^+. This pattern suggests that the detected particles come from some QED process in which one of the beam particles escapes down the beam pipe. A cut on $\cos\theta_{P_{miss}}$ helps suppress such backgrounds.

Examination of continuum Monte Carlo shows additional peaking in $\cos\theta_{P_{miss}}$ (Fig. 3.13). Both electrons and muons show this effect, and no beam correlation is evident. We interpret this as a geometrical-acceptance (fiducial) effect resulting from tracks and showers that escape at small polar angles. Signal Monte Carlo, on the other hand, exhibits anti-peaking at the ends of its $\cos\theta_{P_{miss}}$ distribution. This is a result of the $1 + \sin^2\theta$ distribution of the B mesons' momenta.

Using the high-momentum lepton sample from data and our signal Monte Carlo, we picked a symmetric cut on $\cos\theta_{P_{miss}}$. Of course, such a cut is only reasonable if an event actually *has* missing momentum. We decided to reject events which have

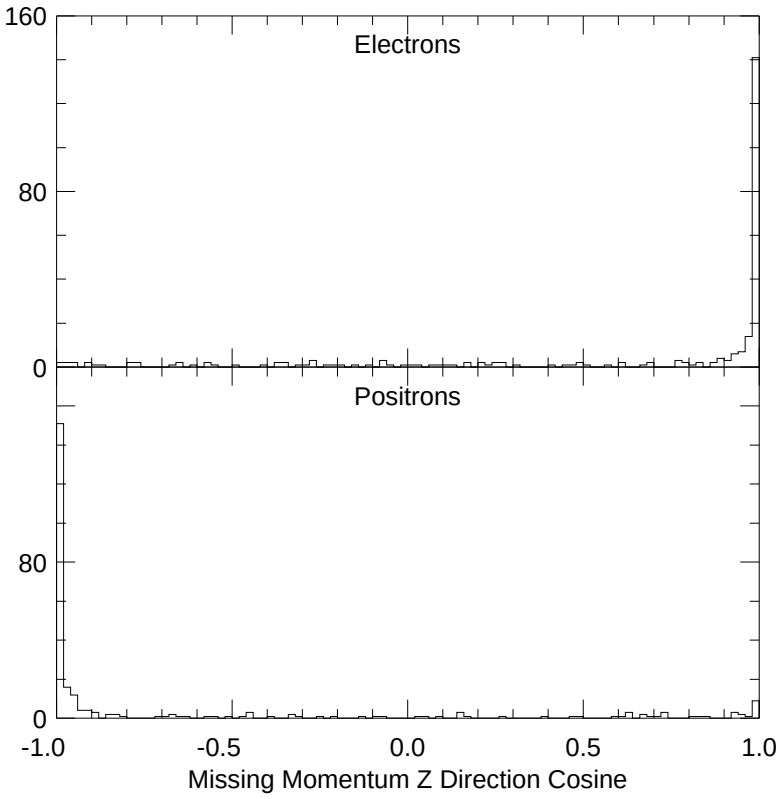

Figure 3.12: Histograms of $\cos\theta_{P_{miss}}$ for electrons and positrons in data with momenta between 3.0 and 3.5 GeV/c. Beam-correlated peaking is quite evident.

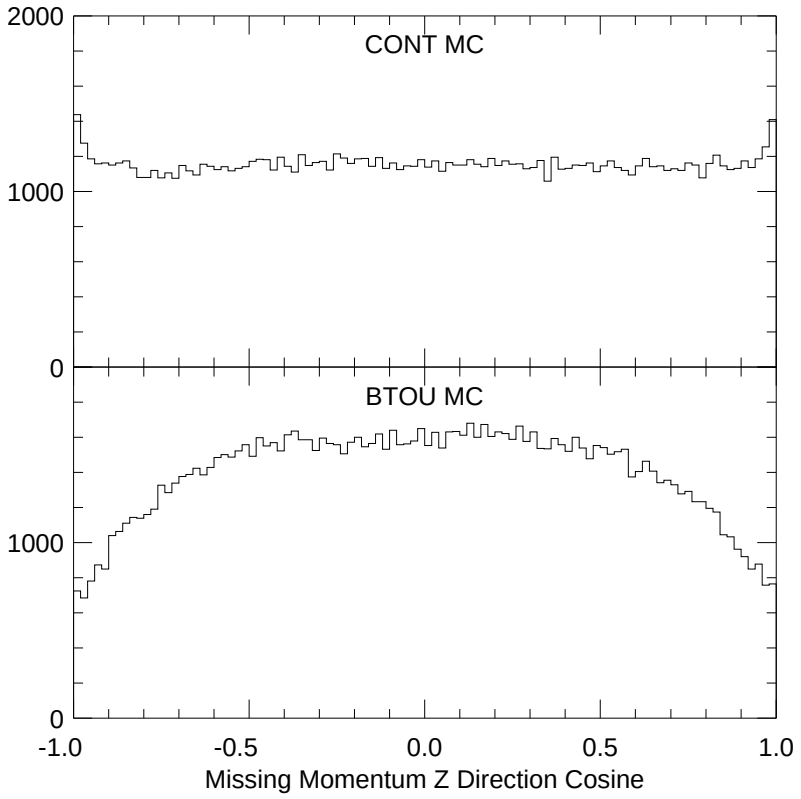

Figure 3.13: Histograms of $\cos\theta_{P_{miss}}$ for events with signal-quality leptons in the momentum interval from 2.0 to 3.0 GeV/c in continuum (CONT) and signal (BTOU) Monte Carlo.

$P_{miss} > 500$ MeV and $|\cos\theta_{P_{miss}}| > 0.9$.

3.2.7 Physics Vetoes

J/ψ Decay

Leptons from leptonic decays of J/ψs produced in the decays $B \to J/\psi X$ constitute a significant background in the end-point region. Fig. 3.14 shows the reconstructed momenta of signal-candidate leptons coming from J/ψ decay in generic $B\bar{B}$ Monte Carlo in the end-point region.

We applied a veto to signal-lepton candidates by calculating the invariant mass of the lepton candidate and any identified lepton of the same type and opposite charge with a momentum above 800 MeV/c. For electrons, we required that the second track pass our standard electron identification cut, while muons were required to have penetrated at least three interaction lengths of absorber material. If the resulting mass fell within a pre-determined cut window, we rejected the candidate lepton as the decay product of a J/ψ. Separate mass windows for electrons and muons were determined by fitting dilepton mass distributions in ON data. In each case, the region around the J/ψ mass peak was fitted with a bifurcated Gaussian (separately adjustable widths on the high and low sides of the peak) and a second-order polynomial for the background. Asymmetric mass windows were then set at $\pm 3\sigma$ (Table 3.2). Fig. 3.15 shows the veto efficiencies as a function of momentum for electrons and muons seperately. Overall, the veto is about 60% efficient for electrons and muons coming from J/ψ decays. It introduces a signal inefficiency of about 0.5%

Table 3.2: The limits of our mass windows used to veto $J/\psi \to \ell^+\ell^-$ candidates.

Channel	Lower Limit (MeV)	Upper Limit (MeV)
e^+e^-	3022.99	3141.95
$\mu^+\mu^-$	3057.66	3137.73

in ISGW2 signal Monte Carlo.

$\gamma \to e^+e^-$

We rejected electron candidates as coming from gamma conversions by combining a given track with other tracks of opposite charge to form candidate vertices [71]. The track was vetoed if the radial position of any well-defined vertex coincided with a concentration of material, such as the beam pipe, the drift chamber walls, or (for CLEO II.V) the silicon wafers in the vertex detector. This veto rejects around 45% of electrons from gamma conversions with momenta above 1.5 GeV/c and introduces a signal inefficiency of around one percent.

3.3 Efficiencies

We must correct our observed lepton spectra for the inefficiencies in our signal-selection criteria. For each of our spectra, we can represent the total efficiency of our cuts as a product of the event-selection, track-quality, and lepton-identification

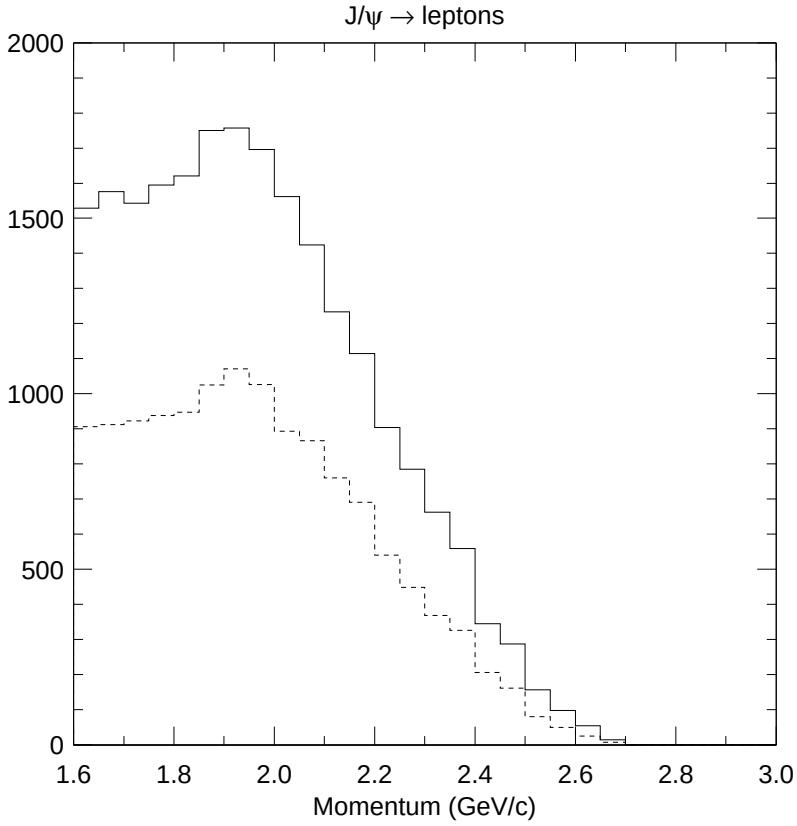

Figure 3.14: Reconstructed momenta of signal-quality leptons from J/ψ decay in generic $B\bar{B}$ Monte Carlo. The solid histogram shows the spectrum of all such leptons. The dashed histogram is the spectrum of leptons actually vetoed.

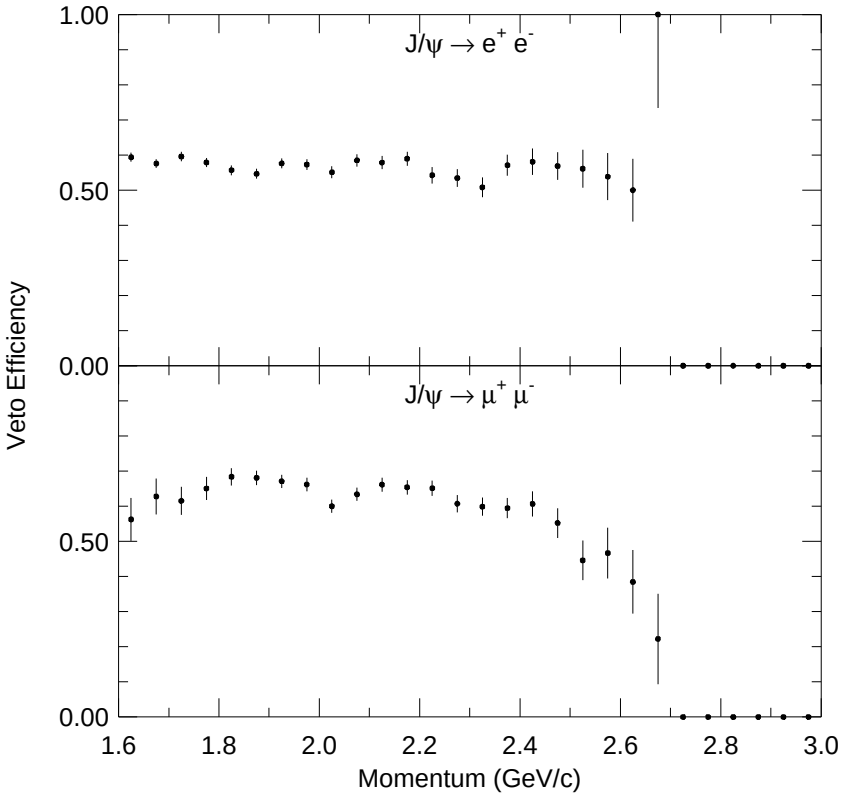

Figure 3.15: J/ψ veto efficiencies versus momentum in generic $B\bar{B}$ Monte Carlo.

efficiencies:

$$\epsilon = \epsilon_{event}\epsilon_{track}\epsilon_{lepid}.$$

We used this approach to explore the effects of our cuts with samples of Monte Carlo and data events. We estimated the limits of our understanding of the effects of each cut and then combined these estimates to compute a systematic uncertainty on our total signal-selection efficiency. Because the CLEO II and II.V detector configurations were different, we performed separate studies for each data set.

3.3.1 Event-Selection Efficiency

We studied the efficiency of our event-selection cuts using samples of about 600,000 CLEO II and 1.1 million CLEO II.V Monte Carlo events with one $B \to X_u \ell \nu$ transition simulated with the ISGW2 model. All four types of B mesons produced at the $\Upsilon(4S)$ were represented in this sample in equal amounts. Efficiencies measured with this sample were binned in generated momentum.

We can factor our event-selection efficiency into the following product:

$$\epsilon_{event} = \epsilon_{evt}\epsilon_{ANN}. \tag{3.11}$$

Here ϵ_{ANN} is the efficiency of the neural-net cut and ϵ_{evt} is the efficiency of the rest of the cuts on event multiplicity, visible energy and the magnitude and direction of the event's missing momentum. Fig. 3.16 shows the measured values of these efficiencies for the CLEO II and II.V data separately. The general event-selection cuts contribute around 9% to our total inefficiency, with slightly better performance in CLEO II.V.

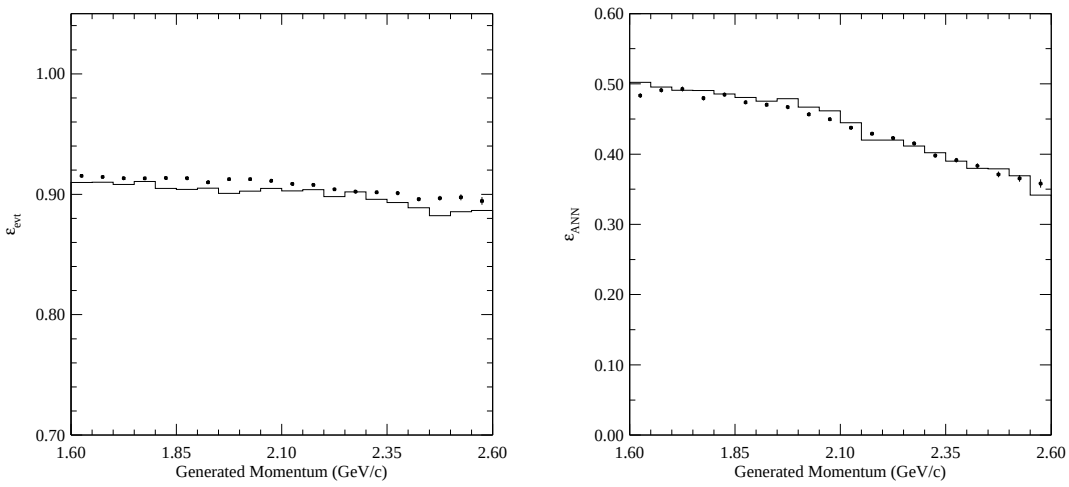

Figure 3.16: Measured efficiencies for general event (left) and neural-net (right) cuts. CLEO II (II.V) efficiencies are shown with solid lines (points). Note the different vertical scales of the two plots.

We conservatively assume that this inefficiency is known to within one third of itself and quote a $\pm 3\%$ systematic error on ϵ_{evt}.

The neural-net-cut efficiency is quite consistent between the two sets of data, and varies from around 50% to 35% for lepton momenta from 1.6 to 2.6 GeV/c. This momentum-dependent structure is not unexpected, since signal events with the most energetic leptons should be the most continuum-like in shape. Given the dependence of the neural-net cut's efficiency on a decay's q^2, we expect that it will contribute a model-dependent systematic error to our total efficiency. We have studied this using various signal Monte Carlos and discuss the results in Sect. 3.3.4.

We checked for an energy-dependent bias in our net's efficiency using CLEO II

continuum Monte Carlo. Separating the sample into ON and OFF components, we found that the efficiency of our cut was constant at the 0.1% level.

3.3.2 Tracking Efficiency

We also used our ISGW2 signal Monte Carlo sample to study the efficiency of the track-selection criteria. We can express the tracking efficiency as the product:

$$\epsilon_{track} = \epsilon_{match}\epsilon_{fid}\epsilon_{sig}. \tag{3.12}$$

Here ϵ_{match} is the efficiency for associating a reconstructed track with a generated lepton, ϵ_{fid} is the efficiency of the fiducial cut on matched tracks, and ϵ_{sig} is the efficiency of our signal track quality cuts on tracks in the good barrel. Fig. 3.17 shows the measured values of the track-matching and fiducial efficiencies. Track-matching performance appears to be slightly better in CLEO II than in CLEO II.V. Both sets of data show an increase in track-matching efficiency starting at momenta around 2.5 GeV/c. This is likely due to the fact that leptons must move along the direction of the B's boost to reach these high momenta. Since Bs are produced with a momentum distribution peaked at high values of $sin^2\theta$, these high-momentum leptons are produced preferentially in the heart of our tracking volume. Overall, track-matching efficiency ranges from around 93% at low momentum to nearly 96% for momenta around 2.6 GeV/c.

Fiducial-cut efficiencies for both sets of data are in good agreement. We selected tracks in the good barrel by requiring that $|\cos\theta| \leq 0.7071$. Therefore, if signal leptons are flatly distributed in $\cos\theta$, we expect ϵ_{fid} to be about 71%. For generated

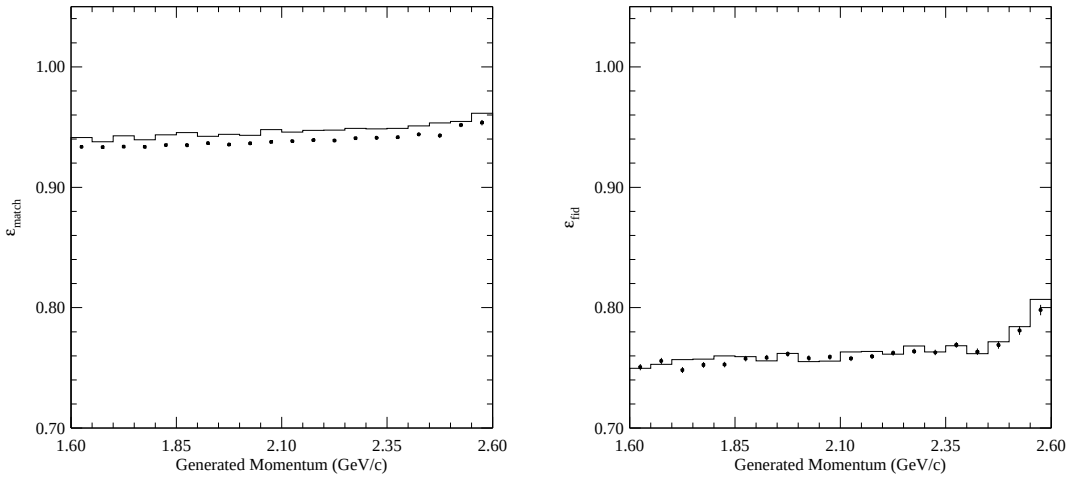

Figure 3.17: Measured efficiencies for track matching (left) and our fiducial cut (right). CLEO II (II.V) efficiencies are shown with solid lines (points).

momenta up to about 2.5 GeV/c it is actually around 75%. This is another consequence of the angular distribution of the leptons' parent Bs, as is the rise of ϵ_{fid} above 2.5 GeV/c.

Fig. 3.18 shows the efficiencies of our signal track quality cuts on matched tracks in the good barrel. Here CLEO II.V shows better performance than CLEO II, with an efficiency that is around 2% higher over most of the momentum interval of interest. This difference is attributable to the different behavior of the gases used in the drift chamber in the CLEO II and II.V experiments. The helium-propane mixture used in CLEO II.V resulted in improved hit efficiency and track-fitting resolutions when compared to the argon-ethane mixture used in CLEO II [50]. Overall, ϵ_{sig} is about 96% in CLEO II and 98% for CLEO II.V.

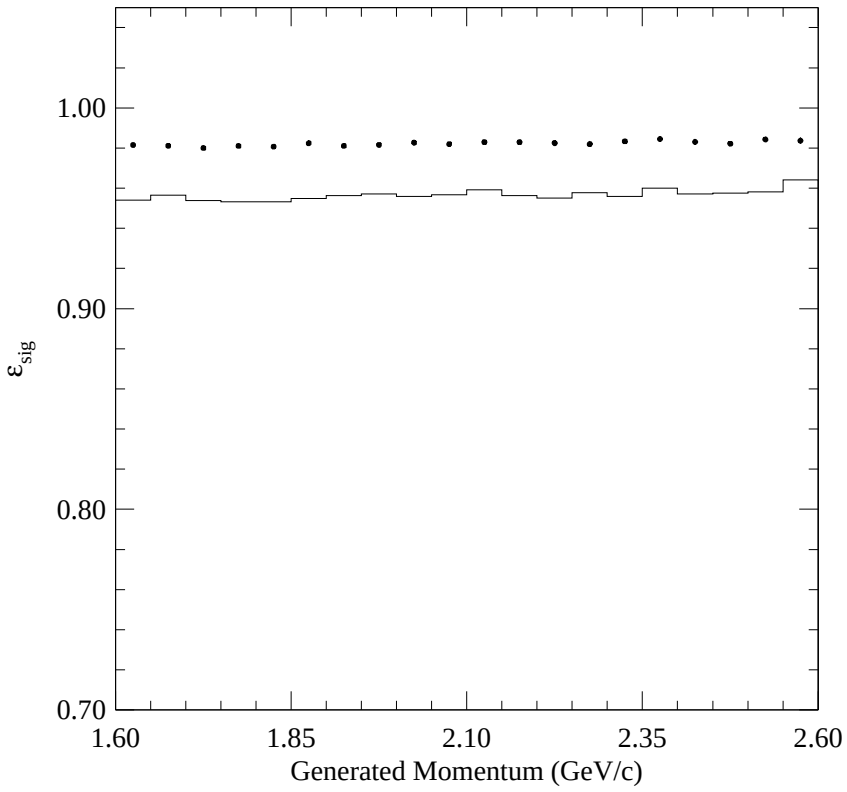

Figure 3.18: The efficiency of our track selection criteria measured using signal Monte Carlo. CLEO II (II.V) efficiencies are shown with solid lines (points).

Studies revealed that some aspects of tracking are not perfectly simulated in our Monte Carlo [72]. To investigate differences between tracking in data and Monte Carlo, we studied samples of radiative Bhabha events (i.e. $e^+e^- \to \gamma e^+e^-$) that were embedded into hadronic events. We used these samples to calculate a momentum-dependent correction factor r to our overall efficiency:

$$r(p) = \frac{\epsilon_{t\_embd}}{\epsilon_{t\_embmc}}. \tag{3.13}$$

Here ϵ_{t_embd} is the tracking efficiency measured with radiative Bhabha events from data that were embedded in hadronic data events. Similarly, ϵ_{t_embmc} is the tracking efficiency found with simulated radiative Bhabha events embedded in simulated hadronic events.

Both embedded samples were generated with radiative Bhabha selection criteria developed at CLEO to study electron-identification efficiencies [73]. For the data samples, $e^+e^- \to \gamma e^+e^-$ events were skimmed from the raw data by requiring that they have exactly two tracks of opposite charge and at least three separate showers with energies of at least 140 MeV. The total energy in the calorimeter was required to be at least 6.0 GeV. Additionally, tracks in candidate events were required to be loosely matched to one of the four biggest showers, and the total energy of the matched showers had to be at least 3.5 GeV. Also, one of the four biggest showers was required not to be matched to either of the tracks. Hadronic target events were selected using the general event-selection criteria described in Sect. 3.2.1. They were also required to contain between 5 and 12 tracks, to have R_2 values no larger than 0.5, and not to contain tracks loosely identified as electrons. Simulated radiative Bhabha

and hadronic events were required to pass the same criteria used in the data skims. For both samples, radiative Bhabha events were embedded into hadronic beds taken near each other in time to ensure that the state of the detector, its calibration, and software versions were compatible.

For track-selection efficiency measurements, we considered good-barrel tracks in the embedded event that were collinear with a pre-embedded radiative Bhabha track to within 8° ($\cos\theta_{open} \geq 0.99$, where θ_{open} is the opening angle between the pre-embedded and embedded tracks). We then applied our signal track quality cuts and calculated the resulting efficiencies. Fig. 3.19 shows plots of measured values of $r(p)$ for embedded CLEO II and II.V events. For both sets of data, the largest effect is at lower track momenta, where the Monte Carlo overestimates the tracking efficiency by about 3% for CLEO II and 5% for CLEO II.V. This effect is less dramatic for the less stringent cuts typically used in other CLEO analyses.

We fitted the CLEO II and II.V $r(p)$ distributions to straight lines over the momentum interval from 1.5 to 2.6 GeV/c. The resulting fit functions are our momentum-dependent corrections to the tracking efficiency estimate. We take half of the maximum deviation of $r(p)$ from 1.0, or 2.5%, as the systematic error on the total tracking efficiency. We also use the fits to $r(p)$ to scale all background spectra taken from Monte Carlo prior to their subtraction.

While factoring out the various components of the signal-selection efficiency gave us insight into the sources of inefficiency and into differences between the two sets of data, we computed the total efficiency by simultaneously applying all cuts to the signal Monte Carlo sample. Fig. 3.20 shows the efficiency of all of the event-selection

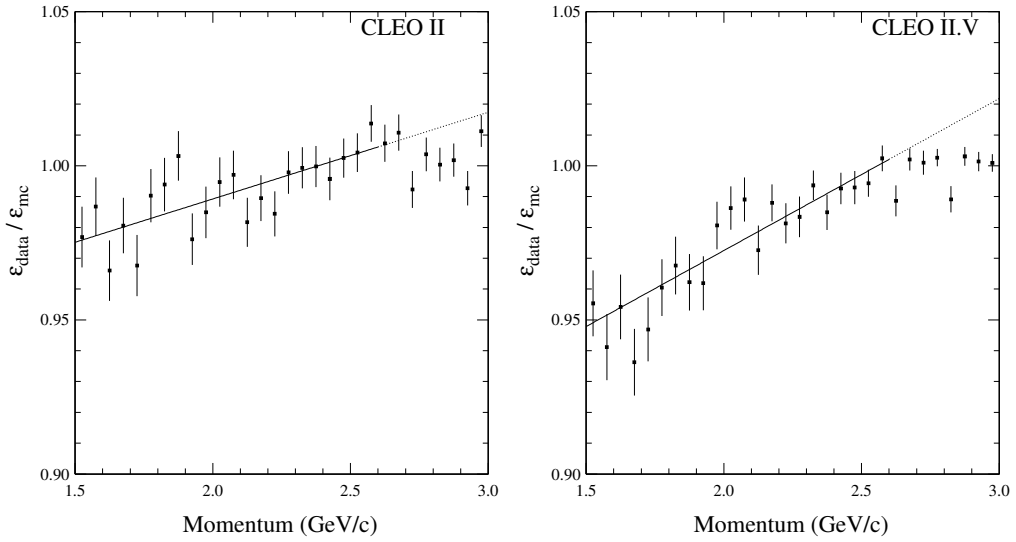

Figure 3.19: Fits to the ratio $r(p)$ of tracking efficiencies measured with embedded data and with Monte Carlo. The CLEO II result is on the left while the CLEO II.V result is on the right.

and track-quality cuts for simulated leptons from $B \to X_u \ell \nu$ decays. Interestingly, the differences in some of the individual cut efficiencies between CLEO II and II.V nearly cancel when all of the cuts are combined. The total efficiency for all of these cuts varies from around 30% near 1.6 GeV/c to about 24% at 2.6 GeV/c. Overall, the efficiency in CLEO II.V is slightly higher than that for CLEO II.

3.3.3 Lepton-Identification Efficiency

We measured our electron identification cut efficiency using tracks stripped from radiative Bhabha events and embedded into hadronic events. For this study Bhabha and hadronic events were selected in much the same way as the samples used for the tracking efficiency study described in Sect. 3.3.2, but in this case single tracks and their associated calorimeter hits were stripped out of the radiative Bhabha events and embedded into the hadronic beds.

Because electron identification relies partially on calorimeter shower shape to discriminate electrons from hadrons, some care was taken to remove Bhabha events in which beam-energy electrons radiate energetic photons in the beam pipe or other material [73]. The directions of photons produced in this way are peaked in the forward direction, along the parent electrons' momenta. For electrons with final momenta between 2.0 and 3.0 GeV/c, the showers in the calorimeter from electron-photon pairs can partially overlap. As a result, the shape of the reconstructed showers matched to the electrons' tracks are not "electron-like," and the electron-identification efficiency measured with such a sample is biased. The strategy employed to avoid this problem involved reconstructing a "vertex momentum," or `PVERTEX`, by using the sum of the

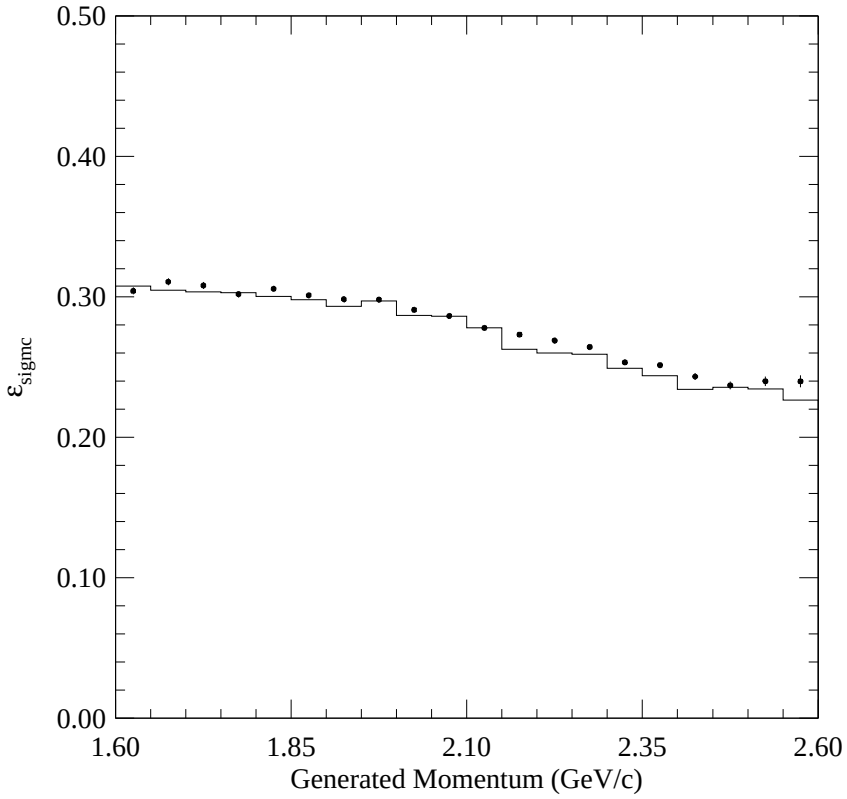

Figure 3.20: The combined efficiency of our event-selection and track-quality cuts measured using signal Monte Carlo. CLEO II (II.V) efficiencies are shown with solid lines (points).

energy of all clusters in the calorimeter matched to a given track as an estimate of the magnitude of the parent electron's momentum. Candidates with values of PVERTEX larger than 3.0 GeV/c were eliminated from the sample [74].

To find the efficiency of our electron-identification cut, we considered embedded tracks that entered the calorimeter barrel, passed our track-quality cuts, and pointed to within 5.1° of the pre-embedded track ($\cos\theta_{open} \geq 0.996$). Fig. 3.21 shows efficiencies measured with all embedded samples for CLEO II and II.V data. A momentum-dependent difference between the two data sets is clearly evident. It begins at around 1.8 GeV/c and grows to around 5% at 2.6 GeV/c, the end point of our signal-electron spectrum. Efficiency measurements made with the samples of embedded radiative Bhabha *events* described in Sect. 3.3.2 show the same effect. Although the PVERTEX cut was applied, it is not clear that it was effective for the CLEO II.V sample. It is likely that some fraction of the difference between the data sets is due to lower-energy electrons radiating photons in the additional material of the silicon detector at small radii in CLEO II.V. Given our uncertainty about the source of the effect, we use separate electron identification efficiency corrections for CLEO II and II.V and quote a 3% systematic error on each of them. This is somewhat larger than one half of the size of the difference in efficiency seen at 2.6 GeV/c, the upper limit of our signal region. We use this larger number since our $B \to X_c \ell \nu$ background fits (Sect. 4.2.5) suggest that the electron/muon ratio in Monte Carlo is slightly wrong.

For Monte Carlo events, the CLEO analysis software mocks up the electron-identification package using log-likelihood distributions measured with embedded electrons binned in momentum and polar angle. Tracks associated with generated

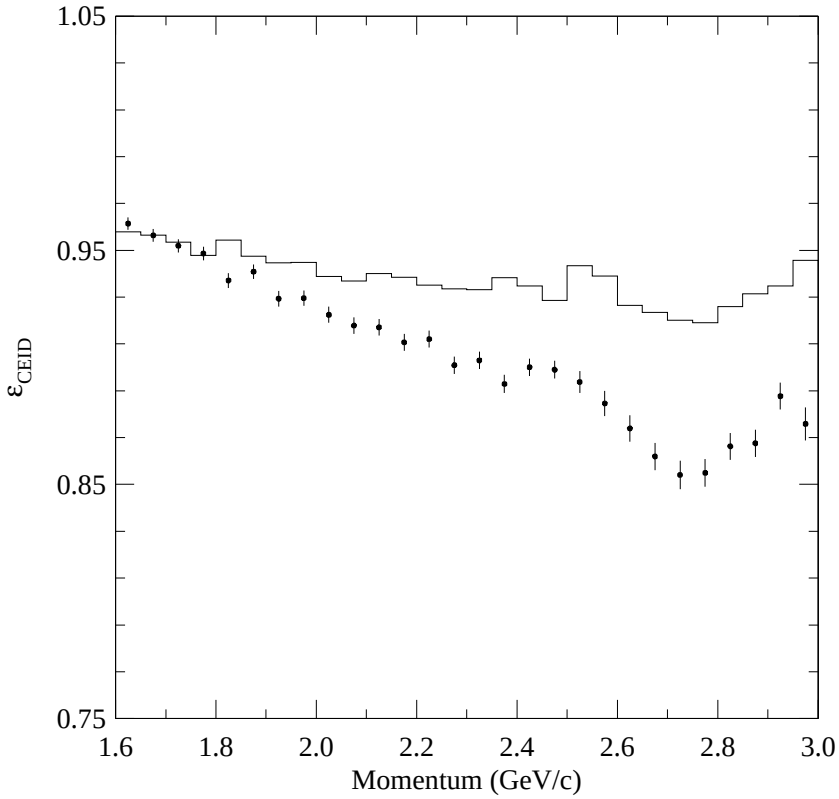

Figure 3.21: The efficiency of our electron-identification cut measured with embedded radiative Bhabha electrons. The CLEO II (II.V) efficiency is shown with solid lines (points). The standard `PVERTEX` ≤ 3.0 cut has been applied to the radiative Bhabha events used for both sets of data.

electrons are randomly assigned a log-likelihood value from the appropriate distribution. We used ISGW2 signal Monte Carlo to measure the simulated electron-identification efficiency that results from this approach. We found the efficiency in Monte Carlo to be flat at ∼92% in the momentum interval from 1.5 to 2.4 GeV/c. Above 2.4 GeV/c the efficiency steps up to nearly 99%. We used the ratio of electron-identification efficiencies measured in data and Monte Carlo to correct our simulated electron-background spectral shapes.

The muon detector has been shown to be well-simulated in Monte Carlo [75, 76]. We therefore decided to measure the efficiency of our muon-identification cut with simulated events. Using samples of CLEO II and II.V generic $B\bar{B}$ and signal $B \to X_u \ell \nu$ Monte Carlo, we considered generated muons matched to reconstructed tracks that passed our signal track quality cuts. For each data set, efficiencies measured with the two Monte Carlo samples are in excellent agreement. ISGW2 signal Monte Carlo provided well-measured efficiencies for momenta out to 2.6 GeV/c. Fig. 3.22 shows our measured muon-identification efficiencies for both CLEO II and II.V. The efficiency is less than 5% for muons with momenta around 1.6 GeV/c and rises with momentum until leveling-off at 85% to 90% at 2.6 GeV/c. It has been customary in the past to quote a systematic error of 2% or less on muon-identifiction efficiencies measured in CLEO II Monte Carlo. We increase this number to 3% to account for the discrepancy between the electron/muon ratios in data and Monte Carlo discussed in Sect. 4.2.5.

Both electrons and muons were subjected to the J/ψ vetoes discussed in Sect. 3.2.7. We studied the inefficiencies due to mistakenly-vetoed signal leptons with Monte

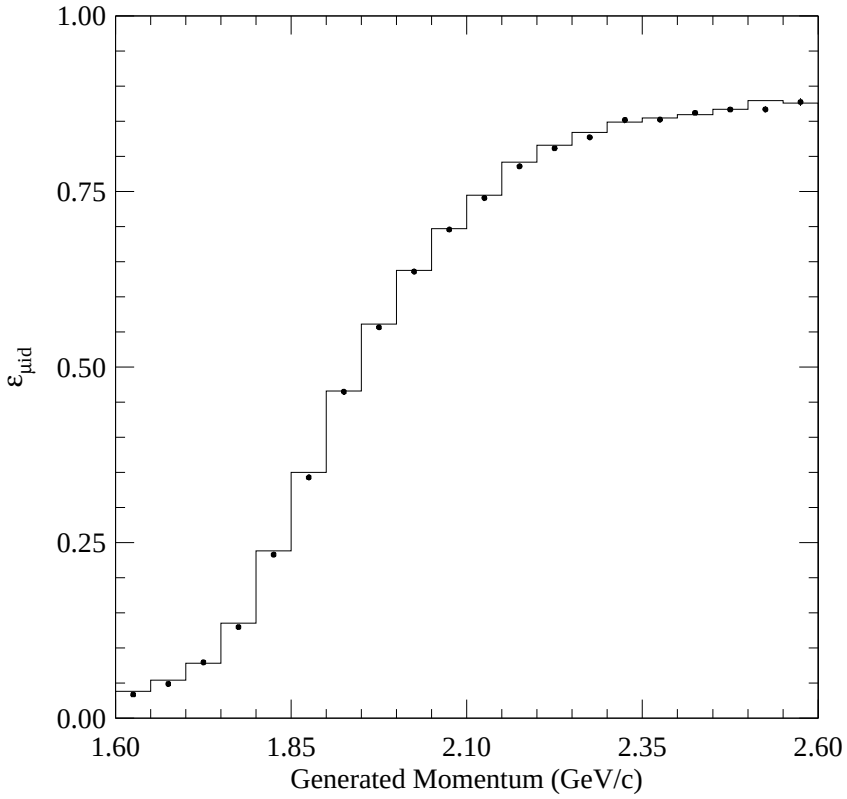

Figure 3.22: The efficiency of our muon-identification cuts measured with ISGW2 signal Monte Carlo. The CLEO II (II.V) efficiency is shown with solid lines (points).

Carlo. We found that in all cases the J/ψ veto introduces an inefficiency of about 0.3% for electrons and muons that pass all other cuts. We conservatively estimate the systematic error in this inefficiency as half of its value, or 0.15%.

Electrons were also subjected to the gamma-conversion veto. Fig. 3.22 shows the resulting inefficiency measured with signal Monte Carlo. This cut is around 98% efficient for signal electrons and has slightly better performance in CLEO II than in CLEO II.V. Once again we take half the inefficiency, or 1%, as a systematic error on its value.

3.3.4 Total Efficiencies

Fig. 3.24 shows the total efficiencies as calculated with ISGW2 signal Monte Carlo for electrons and muons with and without the neural-net cut. Without the net cut, the total efficiency for electrons is approximately 55% and the difference in electron-identification efficiencies between CLEO II and II.V is evident above 2.1 GeV/c. The total efficiency for electrons with the neural-net cut in place varies with momentum from ∼25% to ∼20%, and the difference between CLEO II and II.V electron-identification efficiencies is no longer significant. Total efficiencies for muons rise to about 55% and 22% at 2.6 GeV/c without and with the neural-net cut, respectively. Slightly higher CLEO II.V muon efficiencies are evident in the case without the neural-net cut; this is due to the difference in track-quality-cut efficiencies noted in Sec. 3.3.2.

Averaged over the CLEO II and II.V data sets, and over electrons and muons, the ISGW2-measured efficiency for all cuts in the momentum interval from 2.2 to 2.6

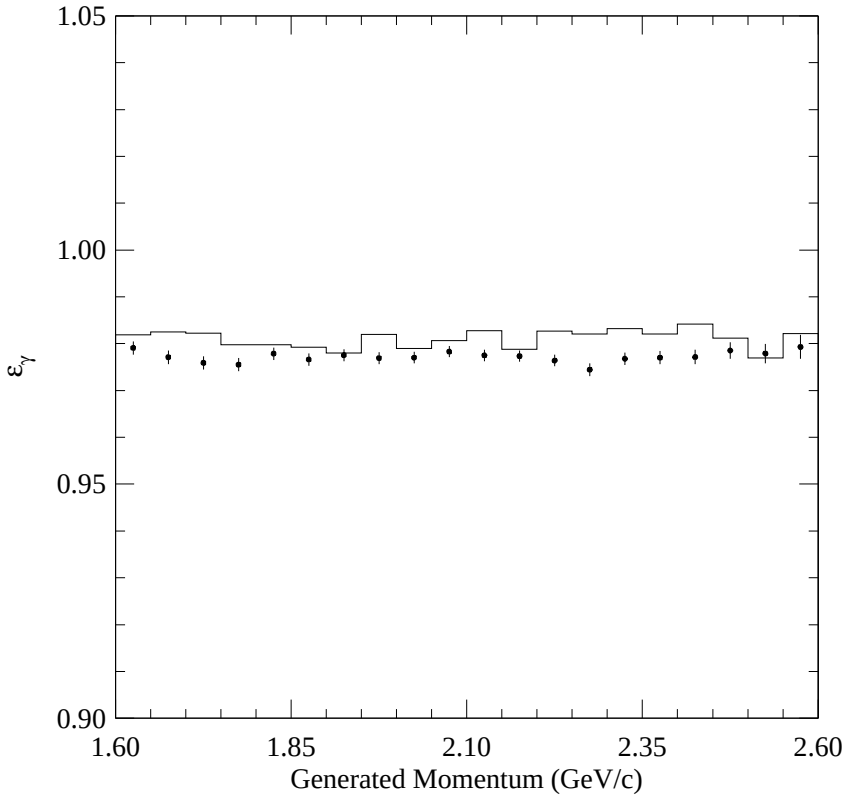

Figure 3.23: The efficiency of our gamma-conversion veto acting on signal electrons in ISGW2 Monte Carlo. The CLEO II (II.V) efficiency is shown with solid lines (points).

GeV/c is 22.7%. The total detector-related systematic error for this interval, averaged in the same way, is 1.1%. This includes a correction factor in the neural-net-cut efficiency that is motivated by the results of the $B \to X_c \ell \nu$ fits discussed in Sec. 4.2.5. Single-parameter fits to spectra measured with the neural-net cut showed that the Monte Carlo overestimates lepton yields by about 2.5%. We therefore corrected the overall efficiency with a factor of $97.5 \pm 1.5\%$, where the systematic error is about one half the size of the observed effect.

To evaluate the model dependence of our total efficiency, we studied the effect of our cuts on signal Monte Carlos generated with alternative models. One of these was the ACCMM model as implemented by Artuso [77] with a Fermi momentum (p_F) of 300 MeV/c and a spectator-quark mass (m_{sp}) of 150 MeV/c^2. These values have been assumed in past studies and have not yet been adequately tested with data. To generate a decay, a Fermi momentum was chosen at random from a distribution of the form described in Eq. 1.22. The b quark was then decayed by the ACCMM prescription, and the daughter and spectator quarks were hadronized according to a fragmentation model tuned to data. The total efficiency calculated with Monte Carlo generated in this way is 21.6%.

We also studied signal Monte Carlo generated with a hybrid of the ISGW2 and ACCMM models. The generator, known as `InclGen`, combines the resonance decays of the ISGW2 model with the ACCMM model's non-resonant final states. This approach begins by using the ACCMM model to generate a B-meson decay with a recoiling hadronic system of mass M_X. Knowledge of the masses of resonances represented in the ISGW2 model is then used to decide between modeling the decay

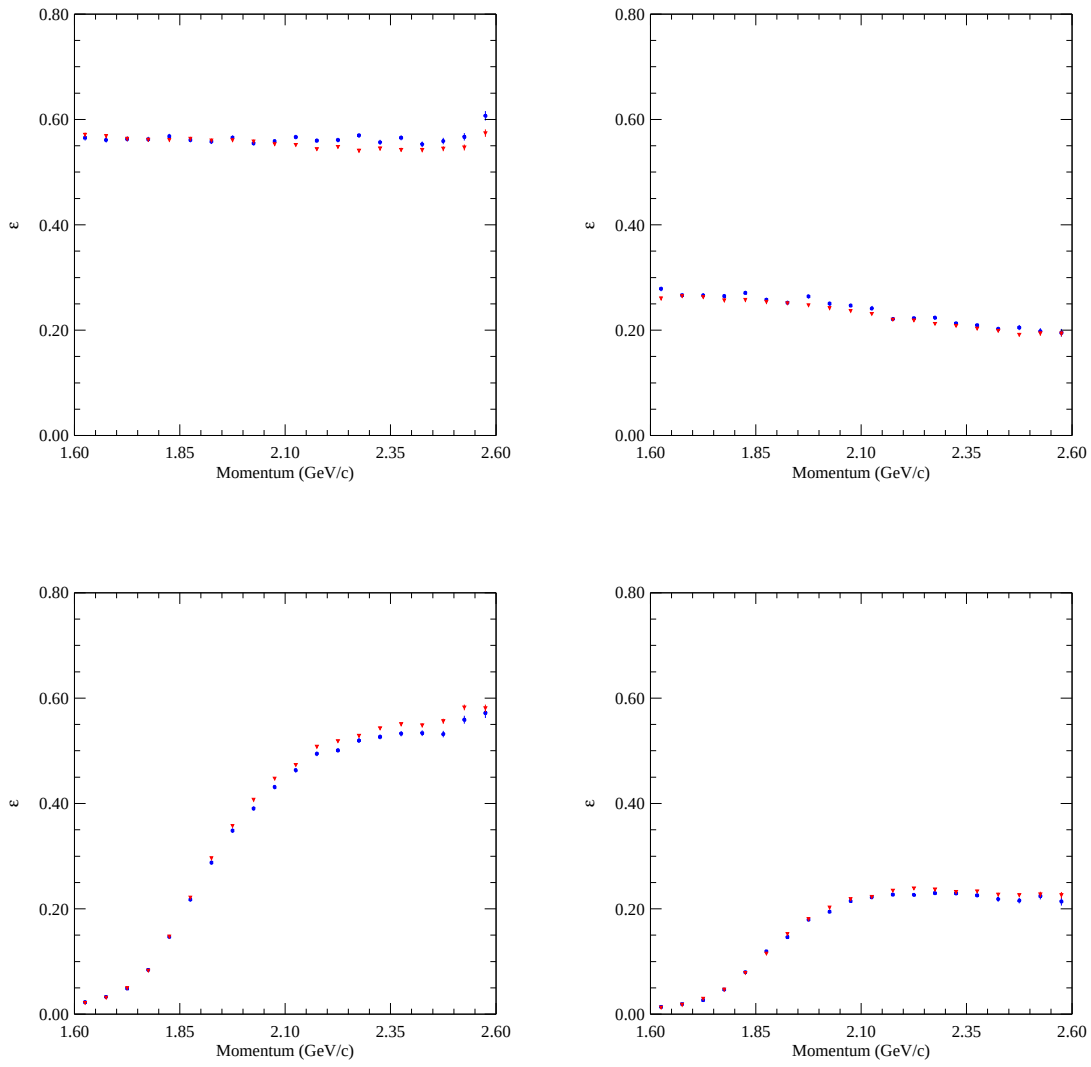

Figure 3.24: Total efficiencies for electrons (top) and muons (bottom). Efficiencies on the right were computed with all cuts, those on the left are for the set of cuts excluding the neural-net cut. CLEO II (II.V) efficiencies are shown with blue circles (red triangles).

inclusively or exclusively. The choice is made randomly, with relative probabilities chosen by comparing the total decay rates for exclusive decays involving resonances with masses near M_X and ACCMM's inclusive rate [78]. Our total efficiency calculated with the `InclGen` Monte Carlo is 21.7%, nearly identical to the ACCMM result.

To test the sensitivity of our efficiency to variation in p_F and m_{sp}, we generated 64 samples of ACCMM Monte Carlo with values of $p_F c$ ($m_{sp}c^2$) varied in 50 MeV steps from 150 MeV to 500 MeV. We then reweighted each spectrum in q^2 using the variation of ϵ_{tot} with q^2 measured with the fully-reconstructed ACCMM sample. We found that, over this wide range of p_F and m_{sp}, the total efficiency varied by 0.8%, slightly less than the 1.0% difference between the ISGW2-simulated efficiency and results from the models including non-resonant decays. We therefore quote a systematic error on our efficiency of $\pm 1\%$ due to uncertainties in modeling $B \to X_u \ell \nu$.

The total efficiencies quoted thus far were calculated by factoring them into several components, each of which received a separate systematic error: basic event-selection, track-quality cuts, the neural-net cut, and lepton identification. We checked this procedure by applying all cuts to the `InclGen` Monte Carlo at once, correcting the resulting spectra for differences between data and Monte Carlo efficiencies, and calculating the total efficiency for one momentum bin from 2.2 to 2.6 GeV/c. The resulting efficiency estimate, 21.4%, is in good agreement with the result of the factored calculation, 21.7%. We take this second, "full-cut" approach as more reliable and use it, along with our estimated detector and model-dependent systematic errors to quote an efficiency from 2.2 to 2.6 GeV/c of $21.4 \pm 1.5\%$.

We have repeated the above efficiency-calculating procedure for the five overlapping momentum intervals used to calculate $|V_{ub}|$ in Chap. 5. Table 3.3 summarizes the results. Our total efficiency decreases as the lower limit of the signal-lepton momentum interval increases, an effect due largely to the momentum dependence of the neural-net cut.

Table 3.3: Total $B \to X_u \ell \nu$ selection efficiencies for five overlapping momentum intervals in the end-point region.

Momentum Interval (GeV/c)	ϵ_{tot} (± 0.015)
$2.0 \leq p_\ell < 2.6$	0.217
$2.1 \leq p_\ell < 2.6$	0.217
$2.2 \leq p_\ell < 2.6$	0.214
$2.3 \leq p_\ell < 2.6$	0.209
$2.4 \leq p_\ell < 2.6$	0.202

CHAPTER 4

The End-Point Lepton Spectrum

4.1 Uncorrected End-Point Lepton Yields

The Lepton yields in the end-point region for the ON and OFF data samples are shown for the analyses with and without continuum suppression in Tables 4.1 and 4.2, respectively. To compensate for the difference in beam energies between ON

Table 4.1: End-point lepton yields without continuum suppression.

Momentum Interval (GeV/c)	CLEO II				CLEO II.V			
	ON		OFF		ON		OFF	
	e	μ	e	μ	e	μ	e	μ
$2.0 \leq p_\ell < 2.1$	16910	14166	1842	1748	30991	27520	3122	3053
$2.1 \leq p_\ell < 2.2$	9476	9743	1500	1746	17215	18716	2674	3095
$2.2 \leq p_\ell < 2.3$	4521	5589	1209	1561	8428	10541	2258	2882
$2.3 \leq p_\ell < 2.4$	2402	3262	981	1480	4777	6474	1829	2607
$2.4 \leq p_\ell < 2.5$	1786	2586	782	1153	3578	5047	1532	2129
$2.5 \leq p_\ell < 2.6$	1487	2049	679	988	2864	4025	1289	1873

Table 4.2: End-point lepton yields with continuum suppression.

Momentum Interval (GeV/c)	CLEO II				CLEO II.V			
	ON		OFF		ON		OFF	
	e	μ	e	μ	e	μ	e	μ
$2.0 \leq p_\ell < 2.1$	6048	4826	103	79	11239	9657	157	145
$2.1 \leq p_\ell < 2.2$	2817	2746	70	70	5252	5443	117	139
$2.2 \leq p_\ell < 2.3$	955	1068	36	53	1715	2026	89	130
$2.3 \leq p_\ell < 2.4$	281	324	34	66	528	652	60	110
$2.4 \leq p_\ell < 2.5$	108	155	36	40	253	346	61	81
$2.5 \leq p_\ell < 2.6$	93	102	41	29	177	184	53	64

and OFF running, track momenta were scaled by the ratio of a nominal ON beam energy of 5.289 GeV to each run's beam energy (`RNENRG`). Combined lepton spectra measured with and without the neural-net cut are plotted in Fig. 4.1 and Fig. 4.2, respectively.

4.2 Background Corrections

4.2.1 Fakes

We estimate the spectra of hadrons misidentified as leptons (fakes) by first computing the charged-hadron spectrum with the following equation [79]:

$$N_h = \frac{n_t - (1 + R_{\mu/e}) \cdot (n_e/\epsilon_{eID})}{1 - (1 + R_{\mu/e}) \cdot (f_e/\epsilon_{eID})}. \tag{4.1}$$

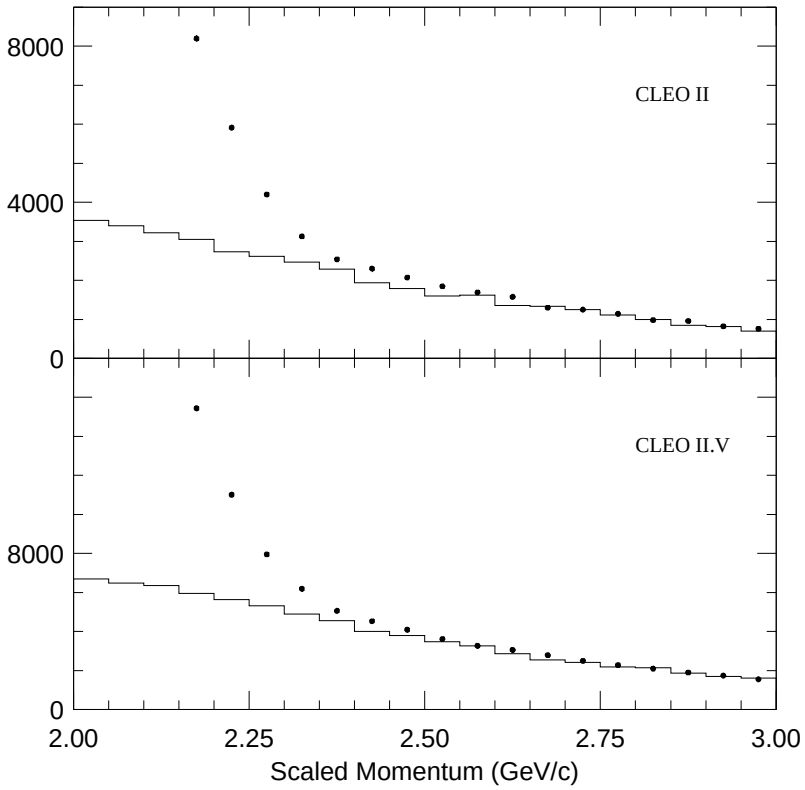

Figure 4.1: The end-point regions of the combined lepton spectra ($e + \mu$) without continuum suppression. The upper plot shows CLEO II data, and the lower plot shows CLEO II.V data. The points are ON data, while the solid histograms are scaled OFF data.

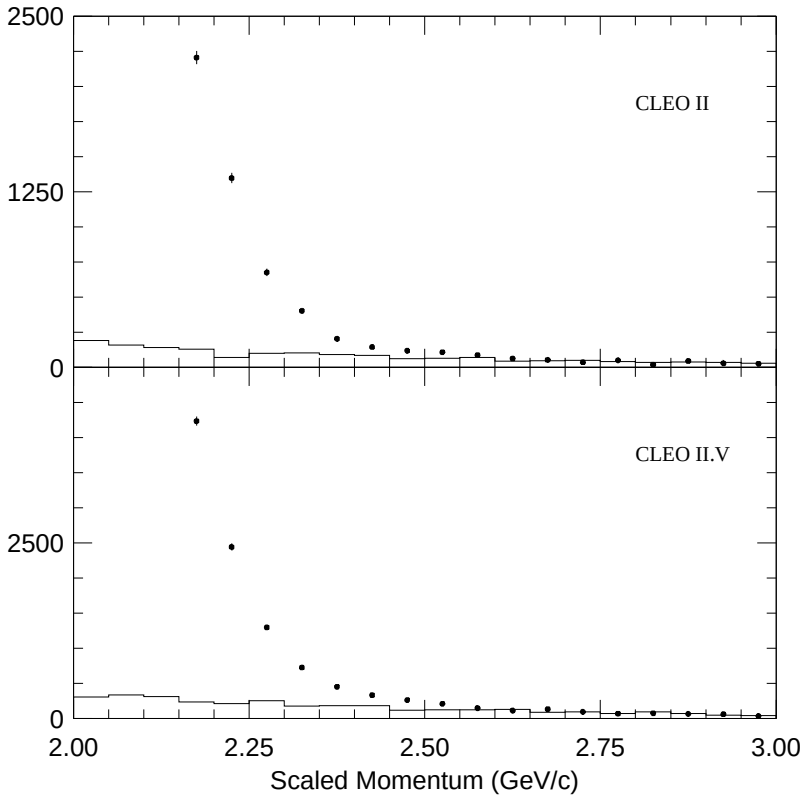

Figure 4.2: The end-point regions of the combined lepton spectra ($e + \mu$) with the neural-net cut applied. The upper plot shows CLEO II data, and the lower plot shows CLEO II.V data. The points are ON data, while the solid histograms are scaled OFF data.

Here n_t is the continuum-subtracted spectrum of all charged tracks passing the same track-quality, event-multiplicity, and continuum-suppression cuts applied to the lepton samples. Because electron and muon candidates must pass different J/ψ vetoes, slightly different track spectra are selected for electron and muon fake calculations. Real leptons are subtracted from n_t in the numerator of Eq. 4.1. Here n_e is the spectrum of detected electrons, ϵ_{eID} is the electron-detection efficiency, and $R_{\mu/e}$ is the ratio of muons to electrons among B-decay products. The denominator of Eq. 4.1 corrects for the fact that some detected electrons are fakes, where f_e is the electron fake rate.

$R_{\mu/e}$ is found using $B\bar{B}$ Monte Carlo. Lepton universality in B decay suggests that this ratio is one for leptons coming from Bs. Additional electron-generating modes among B-daughter decays, however, like Dalitz decays ($\pi^0 \rightarrow e^+e^-$) and photon conversions ($\gamma \rightarrow e^+e^-$), make $R_{\mu/e}$ less than one for momenta below about 1.5 GeV/c. For both electron and muon modes, QED bremsstrahlung lowers the energy of the lepton and changes the shapes of the spectra. The size of the effect depends on the mass of the radiating lepton, so the impact on the electron spectrum is larger than that on the muon spectrum. We used the calculations of Atwood and Marciano [80] to correct our Monte Carlo $R_{\mu/e}$ for this effect. The result is shown in Fig. 4.3.

The hadronic track spectra N_h obtained with Eq. 4.1 are shown in Figs. 4.4 and 4.5. The "bump" around 2.2 GeV/c that appears in all spectra is due to hadronic tracks from two-body B decays.

We calculated fake-lepton spectra by combining N_h with momentum-dependent misidentification probabilities (fake rates) measured with data. In an extension of an

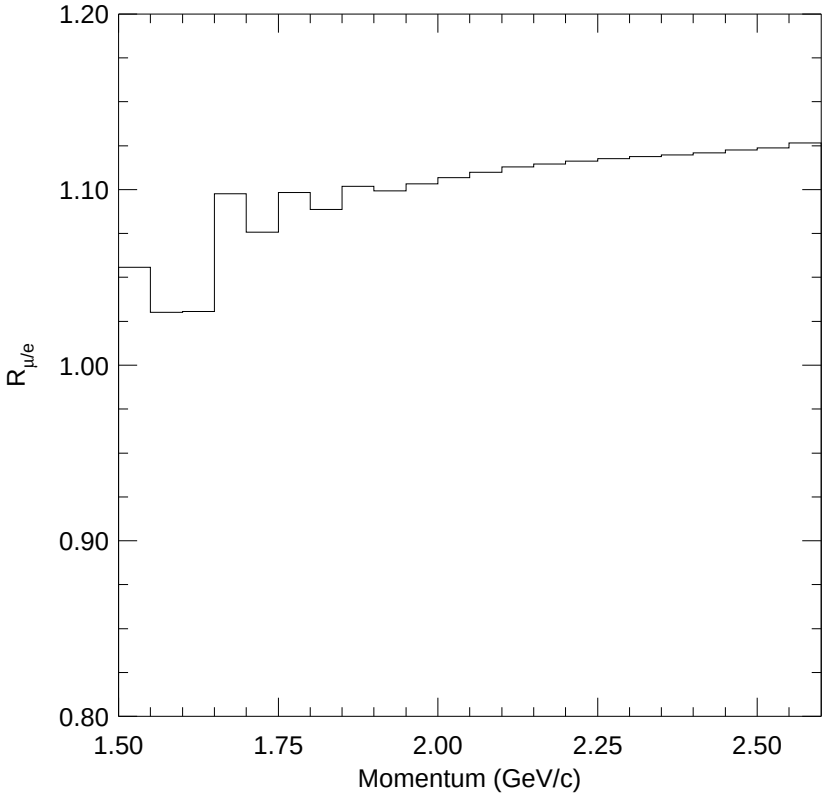

Figure 4.3: Ratio $R_{\mu/e}$ of electron and muon spectra in B decays. Note the suppressed zero on the vertical scale.

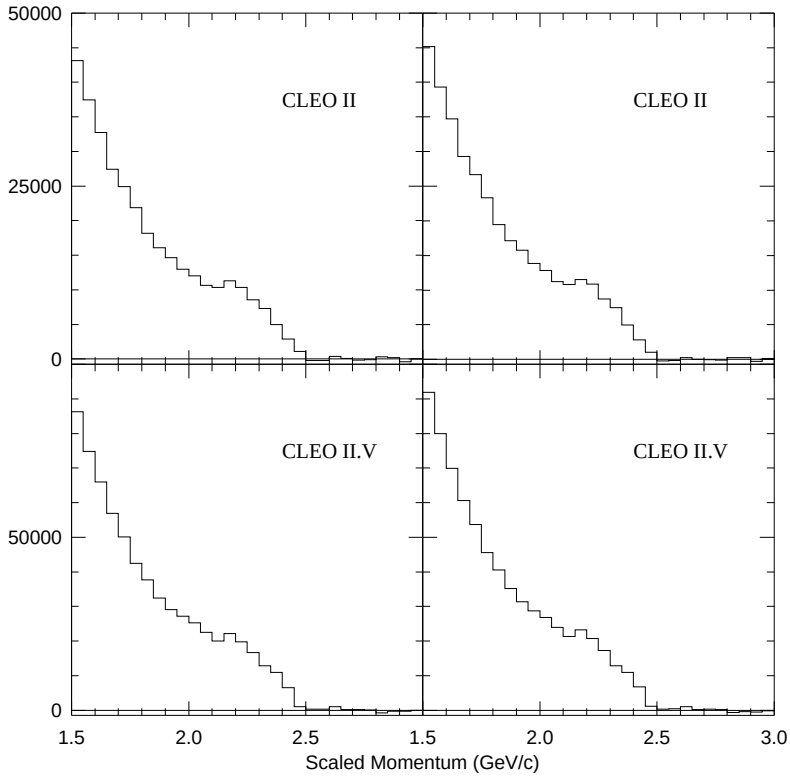

Figure 4.4: Hadronic track spectra without continuum suppression. The upper plots show CLEO II data, and the lower plots show CLEO II.V data. Plots on the left are hadronic tracks passing the electron J/ψ veto, while those on the right pass the veto for muon candidates.

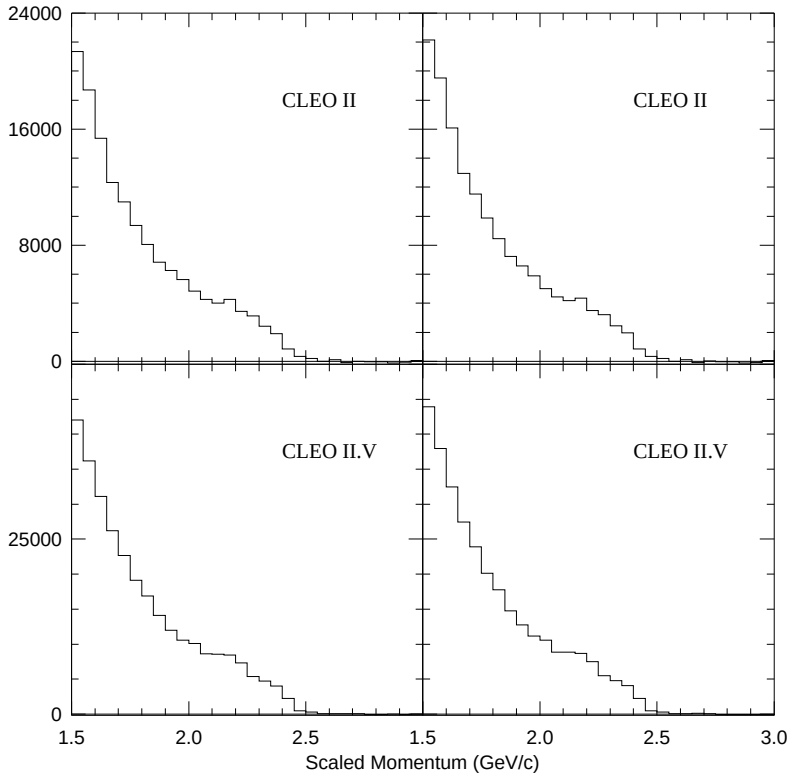

Figure 4.5: Hadronic track spectra with the neural-net cut applied. The upper plot shows CLEO II data, and the lower plot shows CLEO II.V data. Plots on the left are hadronic tracks passing the electron J/ψ veto, while those on the right pass the veto for muon candidates.

earlier analysis [81], measurements over the entire CLEO II and II.V data sets were performed using "tagged" samples of pions, protons and kaons [67]. Pions were taken from the decay ${K^0}_s \to \pi^+\pi^-$. The decay chain $D^{*+} \to D^0\pi^+ \to (K^-\pi^+)\pi^+$ provided a source of kaons and pions. Proton and antiproton samples were obtained from $\Lambda^0 \to p\pi^-$ and $\bar{\Lambda}^0 \to \bar{p}\pi^+$. Samples of each decay process were collected from both ON and OFF data. Backgrounds from leptons and other hadron types were subtracted using sidebands of each of the decay mode's mass plots. Fake rates were then calculated by dividing the number of tagged hadrons passing lepton-identification cuts by the total number of hadrons found. To obtain the total hadronic fake rates for a given lepton identification cut, tagged sample fake rates f_i^ℓ were combined using relative species abundances Y_i taken from $B\bar{B}$ Monte Carlo:

$$f_\ell(\vec{p}) = \sum_{i=p,k,\pi} Y_i(\vec{p}) f_i^\ell(\vec{p}). \tag{4.2}$$

The resulting fake rates are shown in Fig. 4.6. They agree with the results of earlier studies.

Fake spectra calculated with these new fake rates are shown in Figs. 4.7 and 4.8. Fake yields are shown in Tables 4.3 and 4.4. The errors shown in the tables are statistical on the track measurement and fake probabilities. Systematic effects were investigated by comparing fake rates measured with spherical and continuum-like events, ON and OFF samples, and with varying sideband definitions. It was found that a 25% systematic error on fake lepton yields conservatively accounts for biases in this technique.

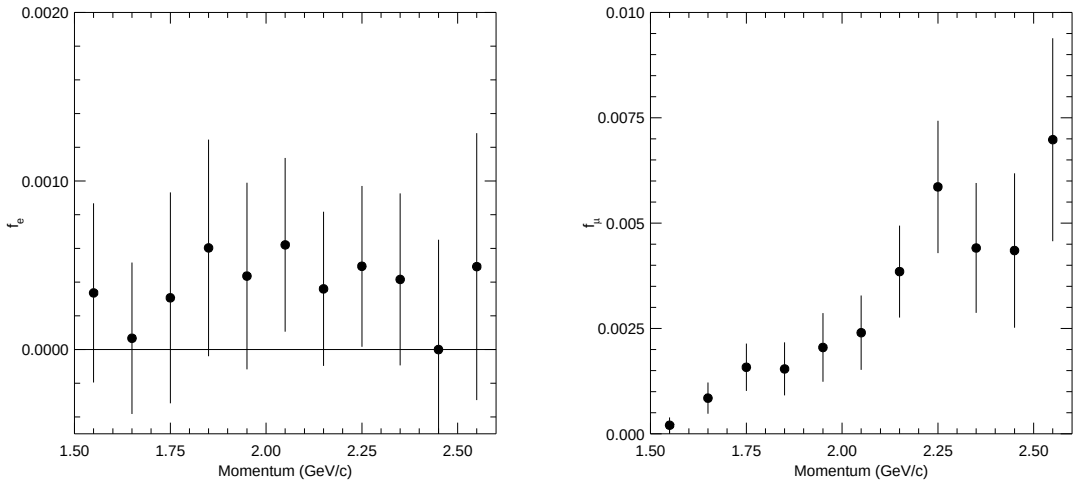

Figure 4.6: Abundance-weighted fake rates for our electron (left) and muon (right) identification criteria. These fake rates were measured using tagged samples for both CLEO II and II.V detector configurations. The errors shown are statistical.

Table 4.3: End-point fake-lepton yields without continuum suppression.

Momentum Interval	CLEO II		CLEO II.V	
(GeV/c)	e	μ	e	μ
$2.0 \leq p_\ell < 2.1$	14.4 ± 8.5	59.1 ± 15.6	29.7 ± 17.4	121.8 ± 31.9
$2.1 \leq p_\ell < 2.2$	7.9 ± 7.1	87.1 ± 17.7	15.1 ± 12.3	171.0 ± 34.6
$2.2 \leq p_\ell < 2.3$	9.4 ± 6.5	115.1 ± 22.4	18.0 ± 12.3	221.5 ± 42.6
$2.3 \leq p_\ell < 2.4$	5.1 ± 4.5	54.8 ± 14.1	9.9 ± 8.6	104.6 ± 26.3
$2.4 \leq p_\ell < 2.5$	0 ± 2.0	16.8 ± 6.1	0 ± 4.2	34.4 ± 13.1
$2.5 \leq p_\ell < 2.6$	-0.2 ± 0.4	-2.6 ± 4.0	0.3 ± 0.5	5.2 ± 5.9

Table 4.4: End-point fake-lepton yields with continuum suppression.

Momentum Interval	CLEO II		CLEO II.V	
(GeV/c)	e	μ	e	μ
$2.0 \leq p_\ell < 2.1$	5.8 ± 3.4	23.3 ± 6.1	11.6 ± 6.8	46.6 ± 12.2
$2.1 \leq p_\ell < 2.2$	3.0 ± 2.7	33.3 ± 6.7	6.1 ± 5.5	67.2 ± 13.5
$2.2 \leq p_\ell < 2.3$	3.3 ± 2.2	39.4 ± 7.6	6.2 ± 4.3	75.6 ± 14.6
$2.3 \leq p_\ell < 2.4$	1.8 ± 1.6	19.5 ± 4.9	3.6 ± 3.1	38.9 ± 9.7
$2.4 \leq p_\ell < 2.5$	0 ± 0.6	5.3 ± 1.8	0 ± 1.5	11.8 ± 4.3
$2.5 \leq p_\ell < 2.6$	0.1 ± 0.2	1.5 ± 1.0	0.2 ± 0.2	2.3 ± 1.1

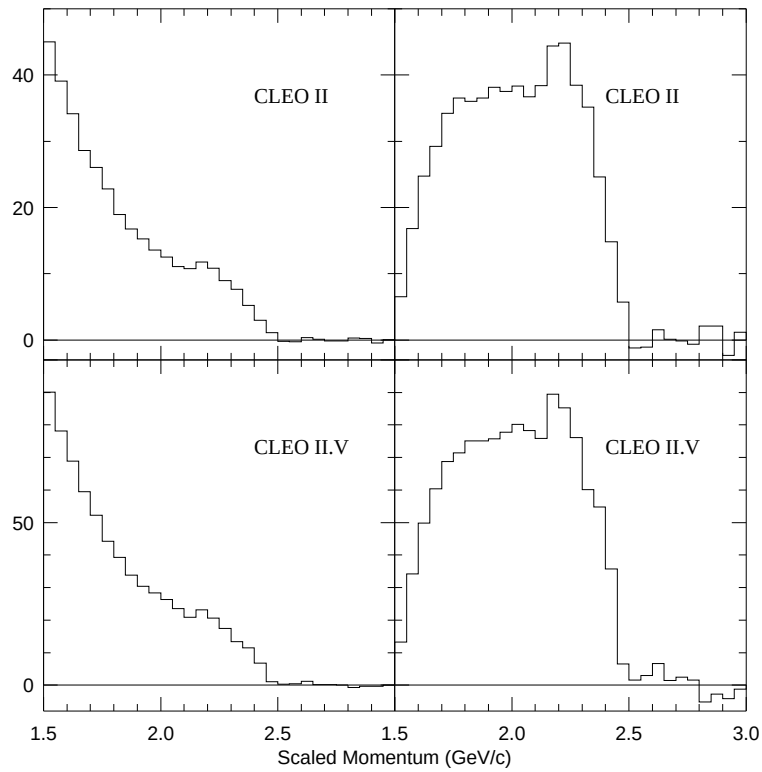

Figure 4.7: Fake-lepton spectra without continuum suppression. The upper plots show CLEO II data, and the lower plots show CLEO II.V data. Plots on the left are fake electrons, while those on the right are fake muons.

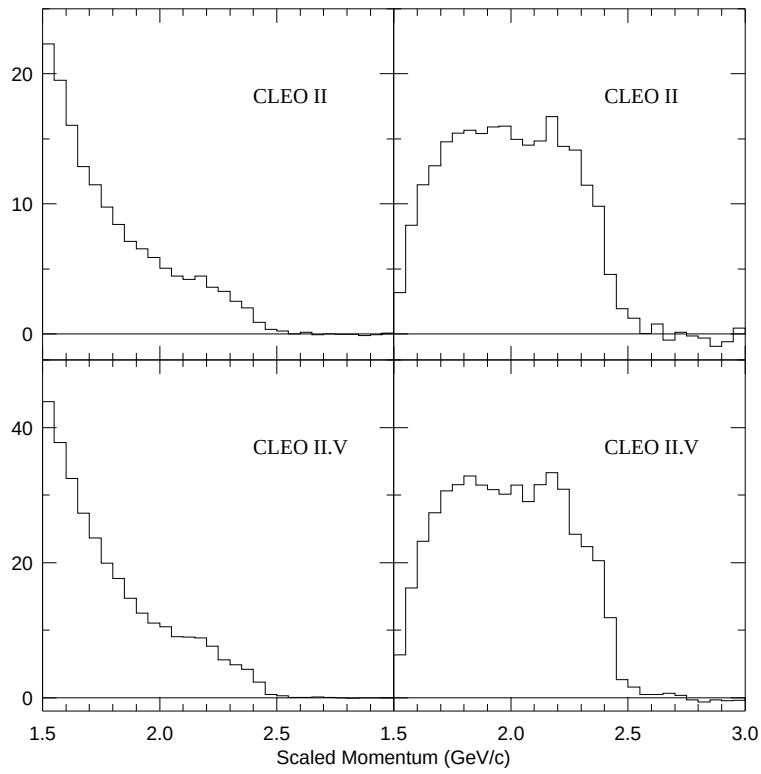

Figure 4.8: Fake-lepton spectra with the neural-net cut applied. The upper plot shows CLEO II data, and the lower plot shows CLEO II.V data. Plots on the left are fake electrons, while those on the right are fake muons.

4.2.2 $J/\psi \to \ell^+\ell^-$ Veto Leakage

We estimated the leakage through our $B \to J/\psi X$ veto using generic $B\bar{B}$ Monte Carlo. To build confidence in the simulation and to extract normalization factors, we fitted spectra of generated leptons from Monte Carlo which were vetoed as coming from J/ψ decay to the corresponding vetoed spectra in data. The neural-net cut was not applied in this study. Prior to fitting, the Monte Carlo electron spectra were corrected for the difference between the simulated electron-identification efficiency and the efficiency measured with data. Simulated electron and muon spectra were both corrected for the difference between the measured tracking efficiencies in data and Monte Carlo. These corrections have a small effect on the shape of the spectra. We obtained reasonable fits in all cases, and the scale factors from the fits are consistent with our expectations based on the numbers of $B\bar{B}$ events in data and Monte Carlo. The fits are shown in Figs. 4.9 and 4.10. The apparent discrepancy in shape at smaller electron momenta has a negligible effect on our end-point measurement. We used the fit normalizations to scale Monte Carlo leptons from J/ψ decay that were not vetoed to estimate the necessary corrections for leakage through the veto. The scaled spectra were also corrected for efficiency differences between data and Monte Carlo. The resulting veto-leakage estimates are shown, along with other backgrounds, in Figs. 4.12, 4.13, 4.14, and 4.15. The decays $B \to J/\psi X$ and $J/\psi \to \ell^+\ell^-$ have been very well-measured, and are well-simulated in our Monte Carlo. We take a 10% systematic error on the estimate of leakage through the J/ψ veto.

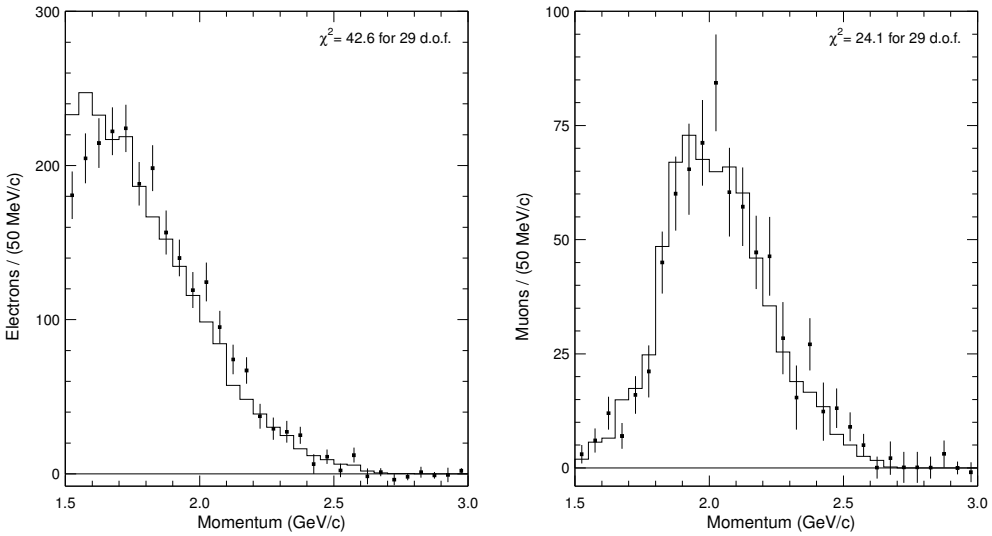

Figure 4.9: Fits of the spectra of leptons vetoed as J/ψ daughters in CLEO II Monte Carlo to those vetoed in data. While there is some evidence for a slight disagreement between the shape of electron spectra in data and Monte Carlo in the $1.5 - 1.7$ GeV/c interval, this has a negligible effect on our end-point measurement.

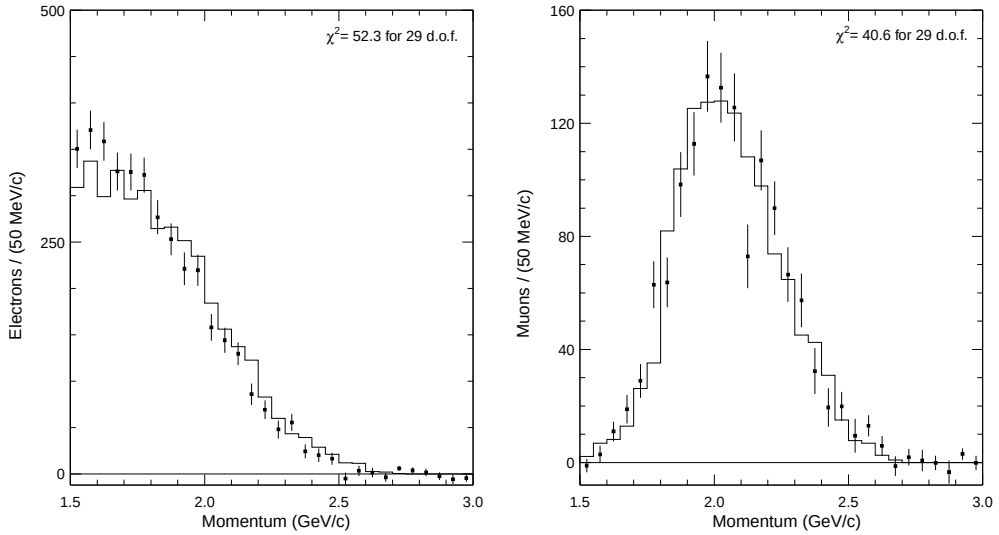

Figure 4.10: Fits of the spectra of leptons vetoed as J/ψ daughters in CLEO II.V Monte Carlo to those vetoed in data. While there is some evidence for a slight disagreement between the shape of electron spectra in data and Monte Carlo in the $1.5 - 1.7$ GeV/c interval, this has a negligible effect on our end-point measurement.

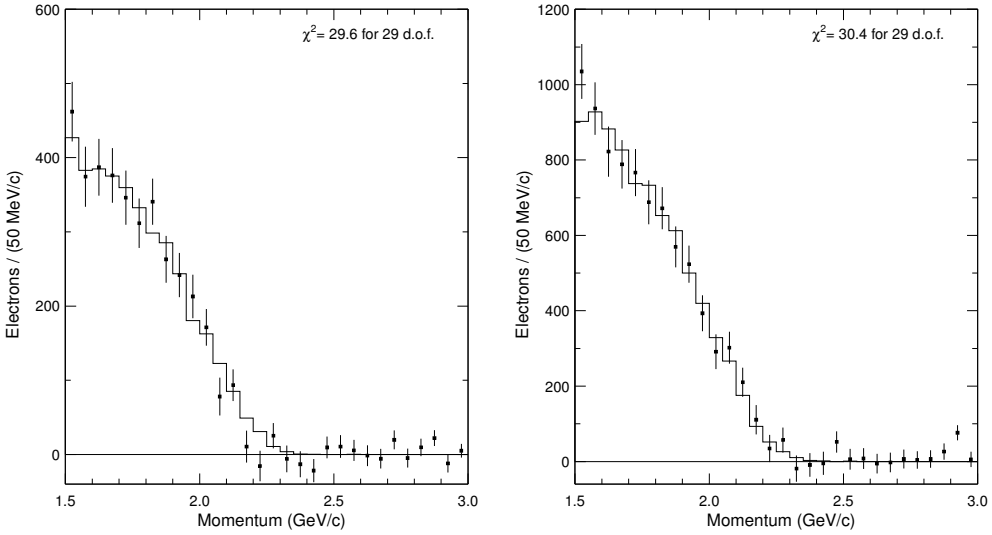

Figure 4.11: Fits of the spectra of electrons vetoed as gamma-conversion daughters in Monte Carlo to those vetoed in data. The fit on the left is for CLEO II, while the CLEO II.V fit is on the right.

4.2.3 $\gamma \to e^+e^-$ Veto Leakage

Leakage through our gamma conversion veto was handled in the same way as the J/ψ veto leakage described above. We fitted the vetoed spectra in Monte Carlo to those seen in data. The fits are shown in Fig. 4.11. The resulting leakage estimates are nearly negligible in the end-point region, and we assign a conservative 25% systematic error on their value.

4.2.4 Secondary $b \to c \to sl\nu$ and Other Physics Backgrounds

We used generic $B\bar{B}$ Monte Carlo to estimate the contributions to the lepton spectra in the end-point region from a number of physics backgrounds. These include π^0 Dalitz decays ($\pi^0 \to e^+e^-\gamma$), leptonic $\psi(2S)$ decays ($\psi(2S) \to \ell^+\ell^-$), semileptonic B decays into τ, and leptonic and semileptonic decays of D and D_s mesons. The resulting spectra were corrected for the difference between data and Monte Carlo electron-identification and tracking efficiencies and then scaled by the ratio of the number of $B\bar{B}$ events in data to the number of Monte Carlo events in the generic $B\bar{B}$ samples. For CLEO II (II.V) this scale factor was 0.20 (0.28). The resulting background estimates are shown in Figs. 4.12, 4.13, 4.14, and 4.15. Electrons from leptonic D_s and π^0 Dalitz decays are too small to be evident in the figures.

In general, these background estimates are small enough that we can use conservative assumptions about how well we understand the physics involved in each of the contributing decays. We assume a 100% systematic error on the π^0 Dalitz decay yields, since they have little impact on the end-point spectra. Branching fractions for the decays $B \to \psi(2S)X$ and $\psi(2S) \to \ell^+\ell^-$ are less well measured than those for $B \to J/\psi X$ and $J/\psi \to \ell^+\ell^-$, so we estimate a 25% systematic error on backgrounds from $\psi(2S)$ decay. We use a 50% systematic error on the yields from D and D_s decays. Production of τ leptons in $B\bar{B}$ is well constrained by lepton universality, and τ decays are well measured, so we conservatively assume a 25% systematic on yields from τ decay.

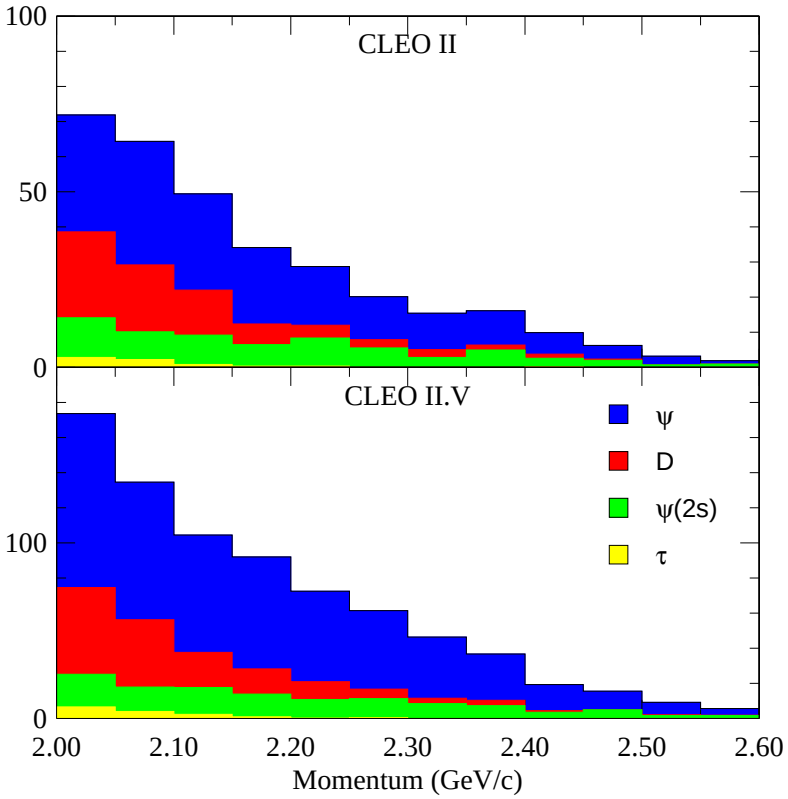

Figure 4.12: Electron backgrounds in the end-point region without continuum suppression. The upper (lower) plot shows CLEO II (CLEO II.V) backgrounds. The key lists the parent type of the electrons in each of the histograms shown.

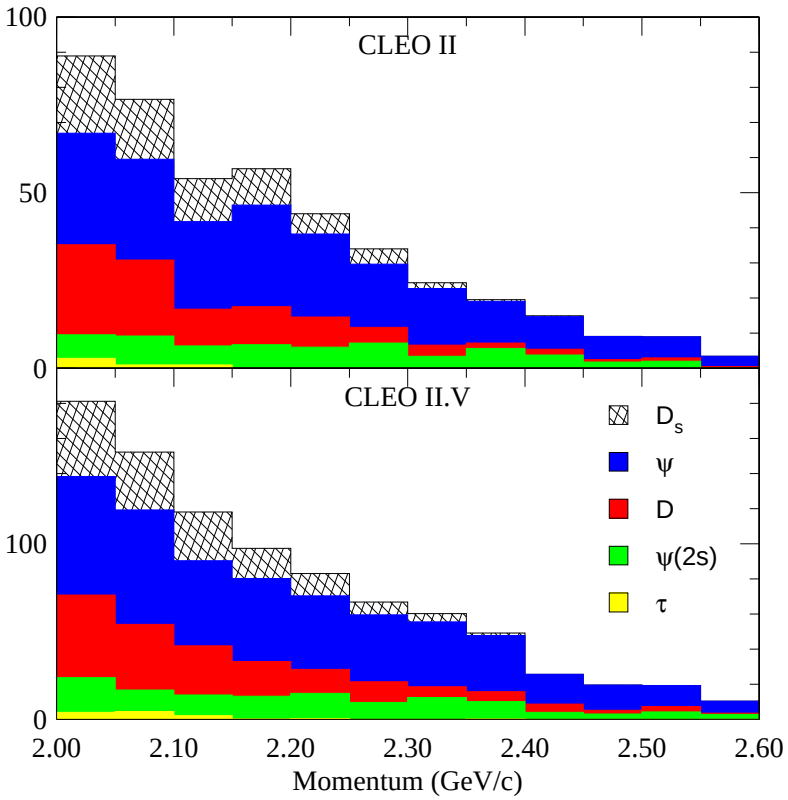

Figure 4.13: Muon backgrounds in the end-point region without continuum suppression. The upper (lower) plot shows CLEO II (CLEO II.V) backgrounds. The key lists the parent type of the electrons in each of the histograms shown.

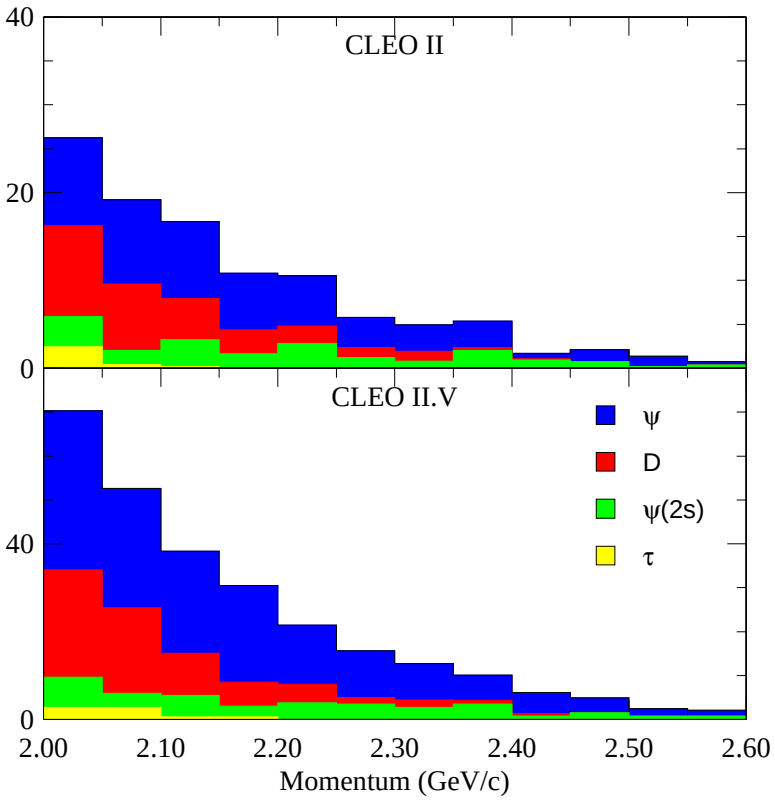

Figure 4.14: Electron backgrounds in the end-point region with continuum suppression. The upper (lower) plot shows CLEO II (CLEO II.V) backgrounds. The key lists the parent type of the electrons in each of the histograms shown.

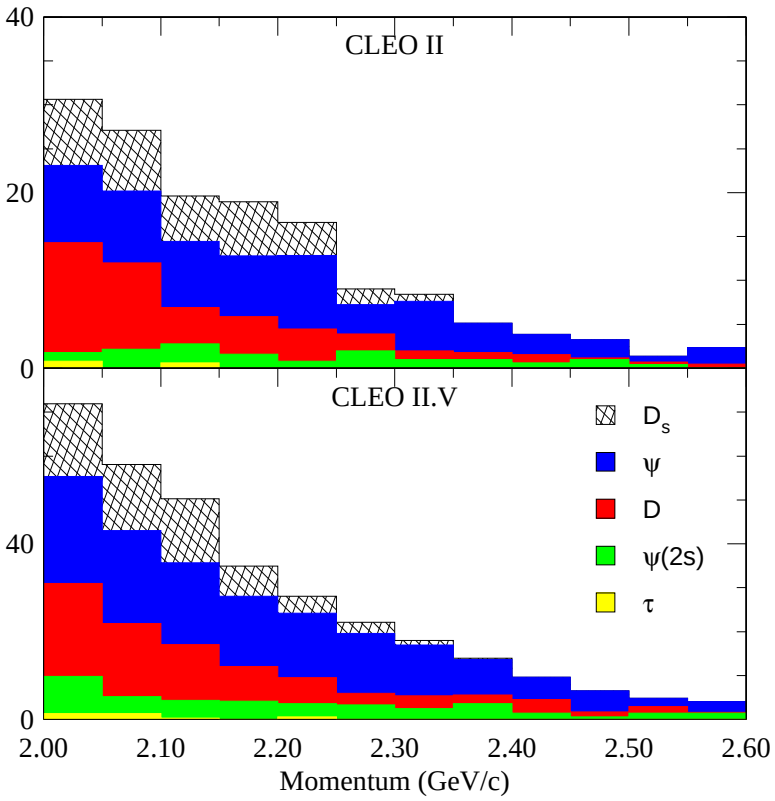

Figure 4.15: Muon backgrounds in the end-point region without continuum suppression. The upper (lower) plot shows CLEO II (CLEO II.V) backgrounds. The key lists the parent type of the electrons in each of the histograms shown.

4.2.5 $B \to X_c \ell \nu$

By far the most severe background to $B \to X_u \ell \nu$ below lepton momenta of 2.4 GeV/c is the dominant semileptonic B-decay process $B \to X_c \ell \nu$. We calculated this by fitting the lepton spectra below the end point to simulated spectra. The estimate is extremely sensitive to the details of the $B \to X_c \ell \nu$ decays. A great deal of effort was invested in getting the pieces right and in determining the range of predictions that are allowed by our spectra and by other available data.

To extract the best possible information about the composition of the $B \to X_c \ell \nu$, we performed fits on combined CLEO II and II.V electron spectra measured without the neural-net cut. The muons were subsequently fitted to the mixture determined by the electron fit. A single overall normalization parameter accounted for possible differences in the detected e/μ ratio between simulation and data. The electron and muon spectra with the neural-net cut applied were each fitted to the electron-determined mixtures, again with only a single normalization parameter. In this case the parameter accounted for possible mis-modeling of the response to the neural-net cut.

We kept our fitting and signal intervals separate by doing three sets of fits with differing upper limits in momentum. For the 2.0-2.6 GeV/c measurement, electrons (muons) were fitted in the 1.5-2.0 (1.8-2.0) GeV/c interval. The upper limit of the fits was moved to 2.1 GeV/c for the 2.1-2.6 GeV/c interval. Fits with an upper limit of 2.2 GeV/c were used for the three remaining intervals. This approach only affected the systematic error estimates, as the central values of the fits' $B \to X_c \ell \nu$ yield estimates agree well.

The $B \to X_c \ell\nu$ components used in the fits were simulated with a modified version of CLEO's $B\bar{B}$ Monte Carlo that included QED radiative corrections as described by the PHOTOS algorithm [82]. PHOTOS allows for the simulation of single-photon emission on an event-by-event basis, and implements a leading-log approximation for the bremsstrahlung matrix element. For the decay $B \to De\nu$, a PHOTOS-simulated electron spectrum has been shown to agree to within better than 10% with the results of an exact $\mathcal{O}(\alpha)$ calculation [83].

There were four components in the standard (STD) fits. We corrected simulated electron spectra for the measured difference between electron-identification efficiency in Monte Carlo and data that was discussed in Sect. 3.3.3. Both e and μ spectra were corrected by the observed ratio of tracking efficiencies in data to those in Monte Carlo (see Sect. 3.3.2). The first component of the fits was a mixture of $B \to D\ell\nu$ (D) and $B \to D^*\ell\nu$ (D^*). The decays $B \to D^*\ell\nu$ were generated with a HQET-based parameterization using CLEO-measured form-factor parameters [35]. $B \to D\ell\nu$ decays were generated with the ISGW2 model. The D/D^* ratio was fixed in the STD fit using measured exclusive branching fractions [3]. The second component, denoted D^{**}, was a mixture of semileptonic decays to higher-mass charmed mesons as described by the ISGW2 model. The third component was nonresonant $B \to D/D^* X\ell\nu$ as described by the model of Goity and Roberts [62]. The final component was ISGW2 $B \to X_u\ell\nu$. Its normalization was fixed by CLEO's 1993 measurement [16] of the $2.3 - 2.6$ GeV/c $B \to X_u\ell\nu$ yield, corrected for the difference in efficiency between then and now. These components provided a very good fit to the electron data (Fig. 4.16). Detailed information about the STD fits is presented in Table 4.5.

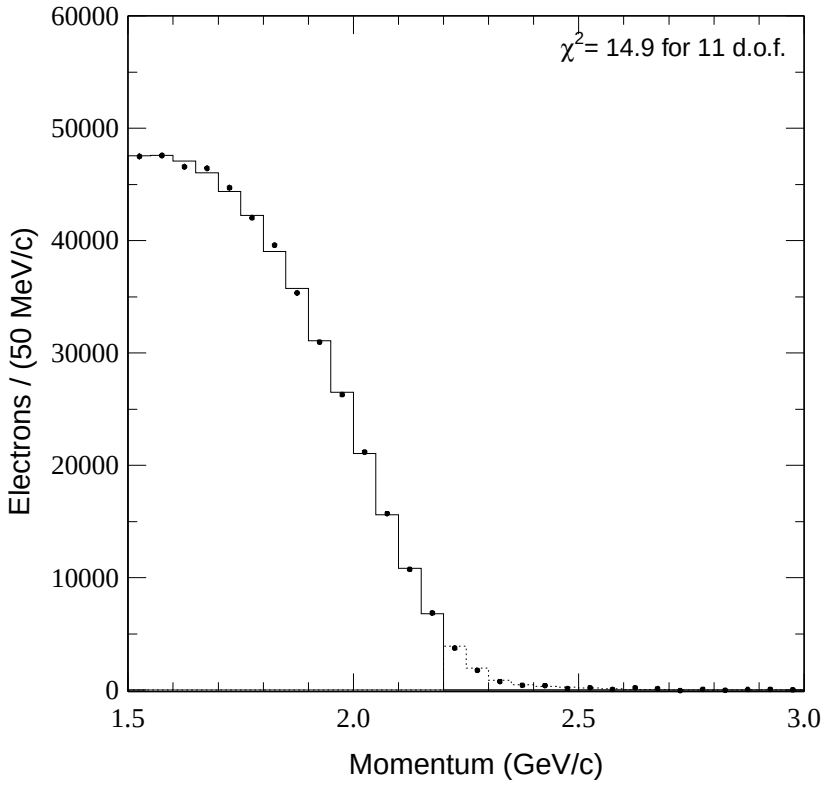

Figure 4.16: The STD fit of the combined CLEO II and II.V electron spectrum that was measured without continuum suppression. The points are data, while the solid (dashed) histogram is the fit result in the momentum interval included in (excluded from) the fits.

The single-parameter STD fit to the muon spectrum without the neural-net cut applied (Fig. 4.17) shows that the Monte Carlo muon spectrum made with the electron-determined mixture must be scaled by a factor of 0.96. This demonstrates that the Monte Carlo does not accurately simulate our detected e/μ ratio. Since we cannot say whether the simulated e efficiency is too high or the μ efficiency is too low, we increased our systematic error estimates for the lepton-identification efficiencies to account for this observation (Sect. 3.3.3).

The fits of the e and μ spectra with the neural-net cut applied (Figs. 4.18 and 4.19) also required scale corrections for Monte Carlo spectra derived using the non-continuum-suppressed fit's mixture ($\sim$0.975). This demonstrates that the Monte Carlo overestimates the neural-net cut's efficiency, and we therefore use the fit's normalization to correct our measured efficiency and add $\pm 1.5\%$ to its systematic error (see Sect. 3.3.4).

We assess the systematic error associated with the $B \to X_c \ell \nu$ subtraction by considering a wide range of variations of the inputs. Details of the resulting fits, including the deviations of their total $B \to X_c \ell \nu$ lepton yields for the $2.2 - 2.6$ GeV/c interval from that of the STD fits, are listed in Tables 4.5, 4.6, 4.7, 4.8, and 4.9. A summary of the systematic error calculations for all momentum intervals in the end-point region is presented in Table 4.10.

For the fits labeled DDSTHI and DDSTLO, we changed the D/D^* proportion up and down by one standard deviation, using the errors on the measured exclusive branching fractions [3]. We also considered more extreme variations in the less-well-known D^{**} and nonresonant components. For the LODDUB fits, we fixed the

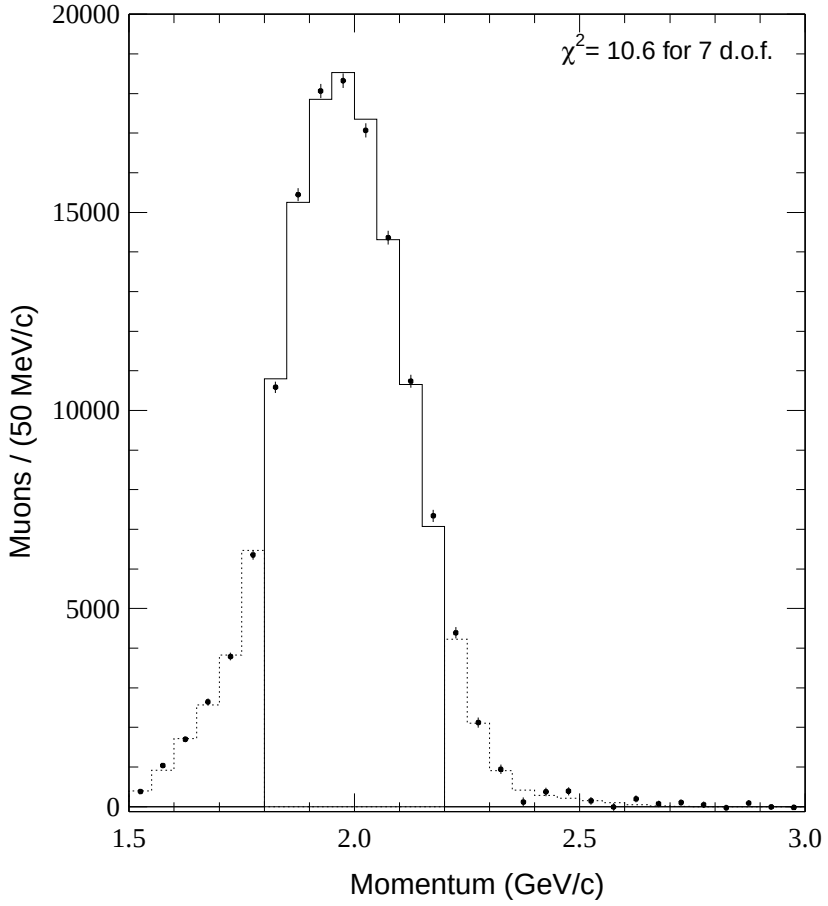

Figure 4.17: The STD fit of the combined CLEO II and II.V muon spectrum that was measured without continuum suppression. The points are data, while the solid (dashed) histogram is the fit result in the momentum interval included in (excluded from) the fits.

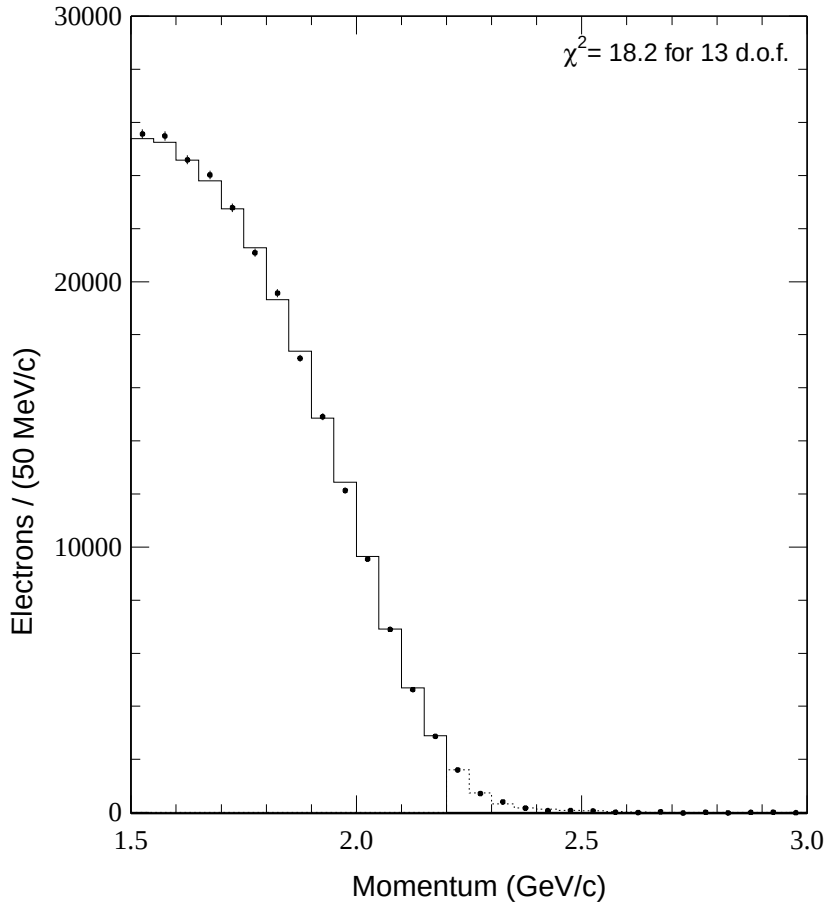

Figure 4.18: The STD fit of the combined CLEO II and II.V electron spectrum that was measured with the neural-net cut. The points are data, while the solid (dashed) histogram is the fit result in the momentum interval included in (excluded from) the fits.

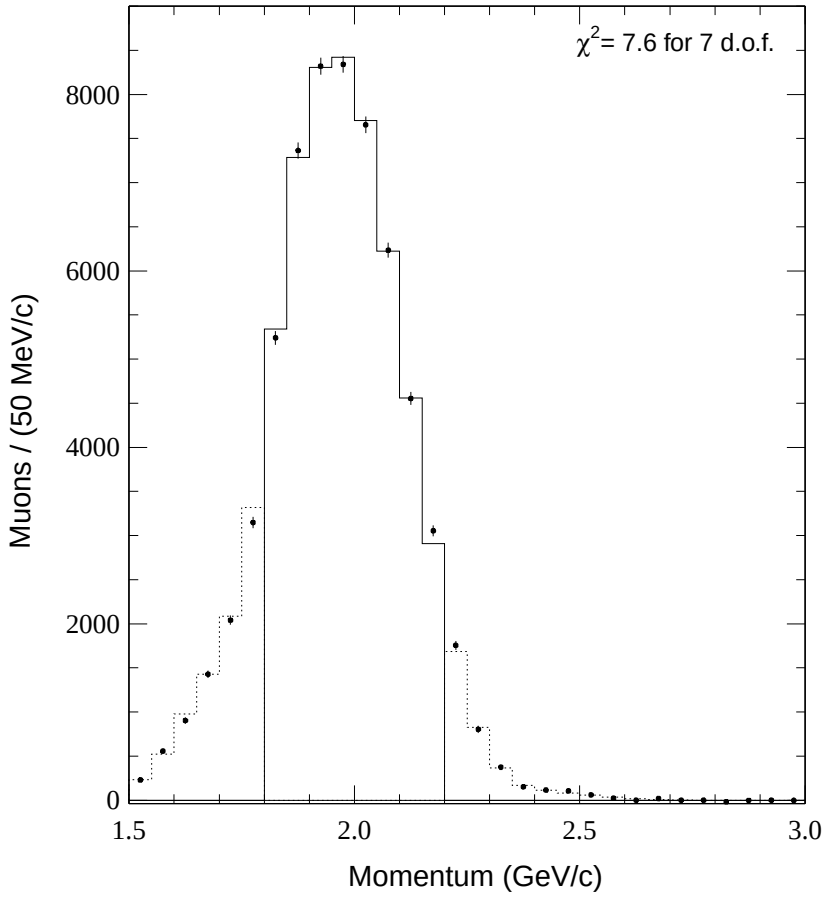

Figure 4.19: The STD fit of the combined CLEO II and II.V muon spectrum that was measured with the neural-net cut. The points are data, while the solid (dashed) histogram is the fit result in the momentum interval included in (excluded from) the fits.

normalization of the D^{**} component to be three standard deviations below the value preferred by the STD fits. The NONR fits were done without any nonresonant component. The results of these fits are negligibly different from the STD fits, so they are not shown in the tables.

To account for uncertainty in the modeling of QED bremsstrahlung corrections to the $B \to X_c \ell \nu$ spectra, we did the NOFSR fits with spectra generated without PHOTOS. This is clearly an overcorrection, so we use one-half of the resulting variation in the lepton yield as an estimate of the QED-associated systematic error.

We also allowed for uncertainty in the B-momentum distribution. Samples of fully-reconstructed Bs were used to measure the charged and neutral B-momentum distributions in data and Monte Carlo [84]. Because charged and neutral Bs differ slightly in mass, their momenta at the $\Upsilon(4S)$ also differ slightly. Measured over the entire CLEO II and II.V data sets, the average charged-B momentum was found to be 0.3168 ± 0.0016 GeV/c in data, and 0.3141 ± 0.0006 GeV/c in Monte Carlo. Thus the average momentum in Monte Carlo was found to be low by 3 ± 2 MeV/c. In data, neutral Bs were found to have an average momentum about 9 MeV/c lower than charged Bs. In Monte Carlo, however, charged and neutral Bs were modeled as having the same mass, and as a result neutral Bs have an average simulated momentum that is too high by about 6 ± 2 MeV/c. Given these considerations, we allowed for an approximately 5 MeV/c variation in the scale of the B momentum used for the boost with the BSTUP and BSTDN fits. We generated the alternative spectra by reweighting our STD spectra in the distribution of generated B-momenta.

We also considered variations in the normalization of the $B \to X_u \ell \nu$ component,

Table 4.5: Results for some of the $B \to X_c \ell \nu$ fits. Entries labeled with a "*" are parameters that were fixed for the fits in question. Explanations of the fit labels in the first row are given in the text. The last row shows the difference in yield between each fit variation and the STD fit in the momentum interval from 2.2 to 2.6 GeV/c.

	STD	DDSTHI	DDSTLO	LODDUB	SECHI	SECLO	NOFSR	BSTDN	BSTUP
e no NN χ^2	14.90	15.50	15.20	15.70	15.20	14.60	12.30	16.90	15.60
d.o.f	11.00	11.00	11.00	12.00	11.00	11.00	11.00	11.00	11.00
$D + D^*$ norm	0.26	0.28	0.25	0.27	0.26	0.26	0.28	0.26	0.26
D^{**} norm	0.25	0.22	0.25	*0.21	0.24	0.25	0.43	0.27	0.28
NR norm	0.00	0.00	0.04	0.06	0.00	0.00	0.05	0.00	0.00
$b \to u$ norm	*1.0	*1.0	*1.0	*1.0	*1.0	*1.0	*1.0	*1.0	*1.0
e w/NN χ^2	18.20	18.50	17.40	17.90	18.30	18.20	13.40	16.50	17.80
d.o.f.	13.00	13.00	13.00	13.00	13.00	13.00	13.00	13.00	13.00
norm	0.99	0.99	0.98	0.99	0.99	0.99	0.98	0.99	0.99
μ no NN χ^2	10.60	9.90	11.50	10.40	10.60	10.70	14.10	19.40	12.10
d.o.f.	7.00	7.00	7.00	3.00	7.00	7.00	7.00	7.00	7.00
norm	0.96	0.96	0.96	0.96	0.96	0.96	1.02	0.94	0.95
μ w/NN χ^2	7.60	6.60	8.60	7.00	7.40	7.80	19.70	16.50	10.00
d.o.f.	7.00	7.00	7.00	7.00	7.00	7.00	7.00	7.00	7.00
norm	0.96	0.97	0.96	0.96	0.96	0.96	0.96	0.96	0.96
Diff (2.2-2.6)	0.00	80.61	-70.23	20.00	2.63	-2.67	155.82	-260.21	144.83

Table 4.6: Results for some of the $B \to X_c \ell \nu$ fits. Entries labeled with a "*" are parameters that were fixed for the fits in question. Explanations of the fit labels in the first row are given in the text. The last row shows the difference in yield between each fit variation and the STD fit in the momentum interval from 2.2 to 2.6 GeV/c.

	STD	FLATEID	B2UHI	B2ULO	EHIFW	ELOFW	NCL	ALT
e no NN χ^2	14.90	15.10	14.90	15.60	14.80	14.50	14.90	14.70
d.o.f	11.00	11.00	11.00	11.00	9.00	9.00	11.00	11.00
$D + D^*$ norm	0.26	0.26	0.26	0.27	0.26	0.26	0.26	0.26
D^{**} norm	0.25	0.34	0.26	0.23	0.25	0.25	0.25	0.26
NR norm	0.00	0.01	0.00	0.02	0.00	0.00	0.00	0.00
$b \to u$ norm	*1.0	*1.0	*1.25	*0.75	*1.0	*1.0	*1.0	*1.0
e w/NN χ^2	18.20	17.20	17.80	18.70	14.80	17.80	18.50	18.90
d.o.f.	13.00	13.00	13.00	13.00	11.00	11.00	13.00	13.00
norm	0.99	0.99	0.99	0.99	0.98	0.99	0.99	0.99
μ no NN χ^2	10.60	16.50	9.30	12.10	10.70	10.60	10.40	9.10
d.o.f.	7.00	7.00	7.00	7.00	7.00	7.00	7.00	7.00
norm	0.96	0.95	0.96	0.96	0.96	0.96	0.96	0.96
μ w/NN χ^2	7.60	14.00	6.10	9.20	7.70	7.60	7.40	5.90
d.o.f.	7.00	7.00	7.00	7.00	7.00	7.00	7.00	7.00
norm	0.96	0.96	0.96	0.96	0.96	0.96	0.96	0.96
Diff (2.2-2.6)	0.00	-45.33	-37.69	41.83	-7.73	1.59	-8.66	-47.34

which was fixed in any given fit. We varied the normalization by $\pm 1\sigma$, using the combined statistical and systematic uncertainty in the 1993 result. These fits are labeled B2UHI and B2ULO in the tables. For the NCL and ALT fits, we substituted $B \to X_u \ell \nu$ spectra generated using the ACCMM-based and `InclGen` generators for the default ISGW2 spectrum.

We also tried changing the lower and upper limits of the electron fits for each fit interval. In each case two alternative sets of fits were performed: one with a lower electron momentum limit of 1.6 GeV/c (ELOFW), and the other having an upper limit that is 0.1 GeV/c smaller that the standard fit's upper limit (EHIFW). For example, alternative intervals of $1.6 - 2.0$ and $1.5 - 1.9$ GeV/c were used for the $2.0 - 2.6$ GeV/c measurement.

Given our uncertainty about the source of the momentum-dependent structure in electron-identification efficiencies observed in Sect. 3.3.3, we have included a set of fits, labeled FLATEID in Table 4.6, in which simulated e spectra were corrected assuming a flat electron-identification efficiency. To be consistent, we corrected Monte-Carlo-estimated background e spectra from other physics processes in the same way before subtracting them from the spectra used in this set of fits.

Our last set of fit variations concerns uncertainties in the measured form factors for $B \to D \ell \nu$ and $B \to D^* \ell \nu$. We accounted for these by reweighting our default Monte Carlo to be consistent with varied values of the respective form factors for these processes.

Because our default $B \to D \ell \nu$ is simulated using the ISGW2 model, we had to reweight it to be consistent with the description using HQET-based form factors

described in Sect. 1.3.3. We reweighted our STD $B \to D\ell\nu$ spectra in q^2 using the ratios of normalized q^2 distributions from the ISGW2 and the HQET descriptions. Results of the fits corresponding to the HQET spectrum with the central value of ρ^2 are labeled DCENT in Table 4.7. We also reweighted to HQET with ρ_D^2 increased by one sigma (DRHO2UP).

To properly account for the uncertainties of the three measured $B \to D^*\ell\nu$ form-factor parameters R_1, R_2, and $\rho_{A_1}^2$, we used reweighted spectra to estimate the partial derivative of the yield with respect to each of the form-factor parameters at their central values. Weight tables were made with Monte Carlo studies for three sets of parameters: $(R_1 + 0.5\sigma, R_2, \rho_{A_1}^2)$, $(R_1, R_2 + 0.5\sigma, \rho_{A_1}^2)$, and $(R_1, R_2, \rho_{A_1}^2 + 0.5\sigma)$. The results of fits with the corresponding sets of reweighted Monte Carlo spectra are shown in Table 4.8. We combined the resulting partial derivative estimates with the form-factor parameter errors and their correlations to estimate the systematic error due to $B \to D^*\ell\nu$ HQET form-factor uncertainties. This was done separately for each of the five momentum intervals considered in our $|V_{ub}|$ calculations. For the 2.2 to 2.6 GeV/c interval, the resulting error estimate is ± 139. As a check, we generated three additional weight tables corresponding to independent -1σ variations in each of the form-factor parameters. The details of the resulting fits are presented in Table 4.9. A calculation using these fits gives an error ± 117 for the interval from 2.2 to 2.6 GeV/c. We note that this result is quite consistent with that obtained with the $+0.5\sigma$ variations, and take the latter as a more conservative estimate of this systematic error.

To compute the total systematic error for the $B \to X_c\ell\nu$ lepton yields in each

Table 4.7: Results for $B \to X_c \ell\nu$ fits with reweighted $B \to D\ell\nu$ spectra. Explanations of the fit labels in the first row are given in the text. The last row shows the difference between each fit variation and the STD fit in the momentum interval from 2.2 to 2.6 GeV/c.

	STD	DCENT	DRHO2UP
e no NN χ^2	14.90	15.20	15.50
d.o.f	11.00	11.00	11.00
$D + D^*$	0.26	0.27	0.27
D^{**}	0.25	0.22	0.18
NR	0.00	0.02	0.05
$b \to u$	*1.0	*1.0	*1.0
e w/NN χ^2	18.20	16.30	14.90
d.o.f.	13.00	13.00	13.00
norm	0.99	0.98	0.98
μ no NN χ^2	10.60	11.70	12.30
d.o.f.	7.00	7.00	7.00
norm	0.96	0.96	0.96
μ w/NN χ^2	7.60	9.00	9.90
d.o.f.	7.00	7.00	7.00
norm	0.96	0.96	0.96
Diff (2.2-2.6)	0.00	-69.10	-114.85

Table 4.8: Results for $B \to X_c \ell\nu$ fits with reweighted $B \to D^* \ell\nu$ spectra corresponding to $+0.5\sigma$ varations in the HQET form factors. Explanations of the fit labels in the first row are given in the text. The last row shows the difference between each fit variation and the STD fit in the momentum interval from 2.2 to 2.6 GeV/c.

	STD	$R_1 + 0.5\sigma$	$R_2 + 0.5\sigma$	$\rho^2_{A_1} + 0.5\sigma$
e no NN χ^2	14.90	12.70	12.60	12.30
d.o.f	11.00	11.00	11.00	11.00
$D + D^*$	0.26	0.25	0.25	0.27
D^{**}	0.25	0.31	0.25	0.07
NR	0.00	0.05	0.09	0.20
$b \to u$	*1.0	*1.0	*1.0	*1.0
e w/NN χ^2	18.20	19.60	15.90	14.30
d.o.f.	13.00	13.00	13.00	13.00
norm	0.99	0.99	0.98	0.98
μ no NN χ^2	10.60	12.00	12.50	14.50
d.o.f.	7.00	7.00	7.00	7.00
norm	0.96	0.96	0.96	0.96
μ w/NN χ^2	7.60	8.70	9.50	11.60
d.o.f.	7.00	7.00	7.00	7.00
norm	0.96	0.96	0.96	0.96
Diff (2.2-2.6)	0.00	-29.85	-47.97	-86.63

Table 4.9: Results for $B \to X_c \ell\nu$ fits with reweighted $B \to D^* \ell\nu$ spectra corresponding to -1σ varations in the HQET form factors. Explanations of the fit labels in the first row are given in the text. The last row shows the difference between each fit variation and the STD fit in the momentum interval from 2.2 to 2.6 GeV/c.

	STD	$R_1 - 1\sigma$	$R_2 - 1\sigma$	$\rho^2_{A_1} - 1\sigma$
e no NN χ^2	14.90	14.30	13.10	16.40
d.o.f	11.00	11.00	11.00	11.00
$D + D^*$	0.26	0.29	0.28	0.27
D^{**}	0.25	0.10	0.18	0.28
NR	0.00	0.00	0.00	0.00
$b \to u$	*1.0	*1.0	*1.0	*1.0
e w/NN χ^2	18.20	15.80	19.30	21.60
d.o.f.	13.00	13.00	13.00	13.00
norm	0.99	0.98	0.99	0.99
μ no NN χ^2	10.60	12.30	11.80	11.40
d.o.f.	7.00	7.00	7.00	7.00
norm	0.96	0.96	0.96	0.96
μ w/NN χ^2	7.60	8.20	7.80	7.40
d.o.f.	7.00	7.00	7.00	7.00
norm	0.96	0.96	0.97	0.97
Diff (2.2-2.6)	0.00	32.50	80.62	156.52

momentum interval, we take the average value of the "symmetric" sets of variations DDSTHI/DDSTLO, SECHI/SECLO, BSTUP/BSTDN, and B2UHI/B2ULO. These averages are then added in quadrature with the LODDUB, NONR, NOFSR, FLATEID, and DRHO2UP variations, as well as the largest member of the EHIFW/ELOFW and NCL/ALT pairs and our estimate of the variation due to uncertainty in the $B \to D^* \ell\nu$ HQET form factors. Table 4.10 summarizes this calculation for the five momentum intervals used in computing $|V_{ub}|$.

In general, the largest contributors to the $B \to X_c \ell\nu$ systematic error are the form-factor uncertainties for $B \to D^* \ell\nu$ and $B \to D \ell\nu$. Variation in the mean B momentum has a significant effect on all intervals. The forced reduction of the D^{**} component is particularly important for the $2.0 - 2.6$ GeV/c interval since the difference between the $B \to D^{**} \ell\nu$ and nonresonant spectra is mostly above 2.0 GeV/c.

4.3 Corrected End-Point Lepton Yields

The yields of leptons for five overlapping momentum intervals in the end-point region are summarized in Tables 4.11-4.15. For all intervals beginning below 2.4 GeV/c, the $B \to X_c \ell\nu$ background estimate makes the largest contribution to the systematic error of the subtracted lepton yield. The total error for the two highest momentum intervals is dominated by the statistical uncertainty of the subtracted OFF data. When statistical and systematic errors are combined, the best-measured yields, those for the intervals starting at 2.2 and 2.3 GeV/c, have fractional errors of $\sim$15%. The

Table 4.10: Results of $B \to X_c \ell \nu$ yield systematic error calculations for five momentum intervals in the end-point region. Differences in yield due to each of the fit variations are presented in rows, with the last row containing the total estimated systematic errors for each momentum interval.

Variation	2.0-2.6	2.1-2.6	2.2-2.6	2.3-2.6	2.4-2.6
DDSTHI	396.7	205.4	80.	20.9	0.7
DDSTLO	-397.2	-166.8	-70.2	-20.0	-0.7
SECHI	40.7	12.3	2.6	0.3	0.0
SECLO	-41.3	-12.4	-2.7	-0.3	0.0
BSTUP	21.9	78.9	72.4	19.4	0.5
BSTDN	-392.9	-277.0	-130.1	-27.0	-0.4
B2UHI	-232.8	-119.2	-37.7	-3.7	0.0
B2ULO	232.7	119.1	41.8	4.1	0.1
LODDUB	707.3	95.1	20.0	2.0	0.0
NONR	-3.7	-1.3	-0.3	0.0	0.0
NOFSR	-295.7	-43.5	77.9	16.2	0.4
FLATEID	-564.2	-225.9	-45.3	-3.7	0.2
DRHO2UP	-536.0	-259.5	-114.9	-30.3	-0.9
DSTFF	644.1	291.7	138.6	16.2	0.4
EHIFW	-168.0	-34.3	-7.7	-0.7	0.0
ELOFW	352.6	-70.9	1.6	0.1	0.0
NCL	-61.1	-31.3	-8.7	-0.8	0.0
ALT	-372.0	-168.4	-47.3	-4.6	-0.1
Total	1458.6	573.0	246.5	49.6	1.4

largest interval, from 2.0 to 2.6 GeV/c, has the largest total error of ∼24%.

Table 4.11: Lepton yields in the momentum interval $2.0 - 2.6$ GeV/c.

	e	μ	Sum
N_{ON}	29466	27529	56995
N_{OFF}	857	1006	1863
Excess	$27703 \pm 182 \pm 18$	$25451 \pm 178 \pm 21$	$53154 \pm 255 \pm 38$
Fakes	$42 \pm 12 \pm 10$	$365 \pm 18 \pm 108$	$406 \pm 29 \pm 109$
J/ψ	$211 \pm 8 \pm 21$	$201 \pm 7 \pm 20$	$413 \pm 10 \pm 41$
Other Backgrounds	$163 \pm 10 \pm 53$	$267 \pm 9 \pm 79$	$430 \pm 13 \pm 132$
$B \to X_c \ell \nu$	$25346 \pm 79 \pm 764$	$23020 \pm 73 \pm 694$	$48367 \pm 107 \pm 1459$
$B \to X_u \ell \nu$	$1940 \pm 199 \pm 767$	$1598 \pm 221 \pm 700$	$3538 \pm 279 \pm 1470$

4.3.1 Electron-Muon Yield Comparisons

We calculated corrected electron and muon yields separately for 100 MeV/c intervals from 2.0 to 2.6 GeV/c. For this purpose, the efficiency- and background-calculating procedures discussed in Chaps. 3 and 4 were repeated separately for electrons and muons. In addition, the QED-radiative corrections discussed in Sect. 5.3 were also computed separately for each type of lepton. The resulting yields are presented in Table 4.16. For this comparison, errors are separated into components that are correlated and uncorrelated between electrons and muons. Yield errors that are correlated

Table 4.12: Lepton yields in the momentum interval $2.1 - 2.6$ GeV/c.

	e	μ	Sum
N_{ON}	12179	13046	25225
N_{OFF}	597	782	1379
Excess	$10949 \pm 121 \pm 12$	$11430 \pm 128 \pm 16$	$22380 \pm 176 \pm 28$
Fakes	$24 \pm 9 \pm 6$	$295 \pm 16 \pm 85$	$319 \pm 24 \pm 85$
J/ψ	$128 \pm 6 \pm 13$	$139 \pm 6 \pm 14$	$267 \pm 8 \pm 27$
Other Backgrounds	$76 \pm 9 \pm 22$	$142 \pm 7 \pm 41$	$218 \pm 11 \pm 62$
$B \to X_c \ell \nu$	$9318 \pm 48 \pm 284$	$9506 \pm 47 \pm 289$	$18824 \pm 67 \pm 573$
$B \to X_u \ell \nu$	$1403 \pm 131 \pm 285$	$1348 \pm 161 \pm 293$	$2751 \pm 191 \pm 584$

Table 4.13: Lepton yields in the momentum interval $2.2 - 2.6$ GeV/c.

	e	μ	Sum
N_{ON}	4110	4857	8967
N_{OFF}	410	573	983
Excess	$3265 \pm 77 \pm 8$	$3673 \pm 85 \pm 12$	$6938 \pm 115 \pm 20$
Fakes	$15 \pm 6 \pm 4$	$194 \pm 13 \pm 58$	$209 \pm 19 \pm 58$
J/ψ	$68 \pm 4 \pm 7$	$90 \pm 5 \pm 9$	$158 \pm 6 \pm 16$
Other Backgrounds	$40 \pm 8 \pm 10$	$67 \pm 6 \pm 18$	$107 \pm 10 \pm 29$
$B \to X_c \ell \nu$	$2147 \pm 23 \pm 116$	$2415 \pm 24 \pm 130$	$4562 \pm 33 \pm 246$
$B \to X_u \ell \nu$	$995 \pm 81 \pm 117$	$906 \pm 106 \pm 133$	$1901 \pm 122 \pm 256$

Table 4.14: Lepton yields in the momentum interval $2.3 - 2.6$ GeV/c.

	e	μ	Sum
N_{ON}	1440	1763	3203
N_{OFF}	285	390	675
Excess	$855 \pm 51 \pm 6$	$958 \pm 59 \pm 8$	$1813 \pm 78 \pm 14$
Fakes	$6 \pm 4 \pm 1$	$79 \pm 8 \pm 27$	$85 \pm 11 \pm 27$
J/ψ	$35 \pm 3 \pm 3$	$50 \pm 4 \pm 5$	$85 \pm 5 \pm 8$
Other Backgrounds	$20 \pm 6 \pm 5$	$32 \pm 5 \pm 9$	$52 \pm 8 \pm 14$
$B \to X_c \ell \nu$	$191 \pm 7 \pm 22$	$249 \pm 8 \pm 28$	$440 \pm 11 \pm 50$
$B \to X_u \ell \nu$	$603 \pm 52 \pm 23$	$549 \pm 65 \pm 32$	$1152 \pm 80 \pm 61$

Table 4.15: Lepton yields in the momentum interval $2.4 - 2.6$ GeV/c.

	e	μ	Sum
N_{ON}	631	787	1418
N_{OFF}	191	214	405
Excess	$239 \pm 38 \pm 4$	$344 \pm 41 \pm 4$	$584 \pm 56 \pm 8$
Fakes	$0 \pm 2 \pm 0$	$21 \pm 3 \pm 9$	$21 \pm 4 \pm 9$
J/ψ	$15 \pm 2 \pm 1$	$21 \pm 2 \pm 2$	$36 \pm 3 \pm 4$
Other Backgrounds	$7 \pm 5 \pm 2$	$15 \pm 5 \pm 5$	$21 \pm 7 \pm 6$
$B \to X_c \ell \nu$	$3 \pm 2 \pm 1$	$3 \pm 2 \pm 1$	$6 \pm 3 \pm 1$
$B \to X_u \ell \nu$	$215 \pm 38 \pm 5$	$285 \pm 43 \pm 7$	$499 \pm 57 \pm 14$

between the two lepton types include the systematic errors on continuum subtractions and all background estimates, and the statistical error on calculated fake leptons. Uncorrelated errors include the statistical errors on the continuum subtractions and backgrounds, and the systematic errors on the fakes. The uncertainties in our efficiency estimates are almost completely correlated between electrons and muons. The only uncorrelated errors are those for the lepton-identification cuts. The fourth column in Table 4.16 contains the differences between the e and μ yields in each bin. The last column presents the significance of each difference in units of its uncertainty. Overall, e and μ yields are in reasonable agreement.

Table 4.16: A comparison of e and μ yields for 100 MeV/c bins in the end-point region. The first (second) error presented on each yield is uncorrelated (correlated) between the two lepton types. The last column presents the significance of the difference between the two yields in each interval.

Momentum Interval (GeV/c)	Electron Yield	Muon Yield	Difference	Significance (σ)
$2.0 \leq p_\ell < 2.1$	$2134 \pm 648 \pm 1589$	$1157 \pm 737 \pm 1653$	-977 ± 981	-1.00
$2.1 \leq p_\ell < 2.2$	$1784 \pm 450 \pm 1174$	$2097 \pm 516 \pm 1291$	313 ± 685	0.46
$2.2 \leq p_\ell < 2.3$	$1840 \pm 287 \pm 581$	$1676 \pm 342 \pm 641$	-164 ± 447	-0.37
$2.3 \leq p_\ell < 2.4$	$1952 \pm 180 \pm 184$	$1278 \pm 224 \pm 177$	-674 ± 287	-2.35
$2.4 \leq p_\ell < 2.5$	$827 \pm 162 \pm 70$	$1012 \pm 160 \pm 78$	185 ± 227	0.81
$2.5 \leq p_\ell < 2.6$	$413 \pm 152 \pm 36$	$361 \pm 124 \pm 29$	-52 ± 196	-0.26

4.4 Corrected End-Point Lepton Spectrum

Fig. 4.20(a) shows the total ON spectrum measured in data and our total background estimate, including the scaled OFF data. Fig. 4.20(b) shows a background-subtracted, efficiency-corrected spectrum over the same interval. For the purposes of making this plot, the efficiency and systematic error calculations discussed above were repeated separately for each 50 MeV/c bin, and statistical and systematic uncertainties were combined in quadrature. Below 2.3 GeV/c, the $B \to X_c \ell \nu$ subtraction dominates the uncertainties, which are strongly correlated from bin to bin. The overlaid theoretical spectrum in Fig. 4.20(b) is a prediction based on fits to the $B \to X_s \gamma$ photon-energy spectrum (Sect. 5.2). It is normalized to the signal yield in the momentum interval $2.2 - 2.6$ GeV/c.

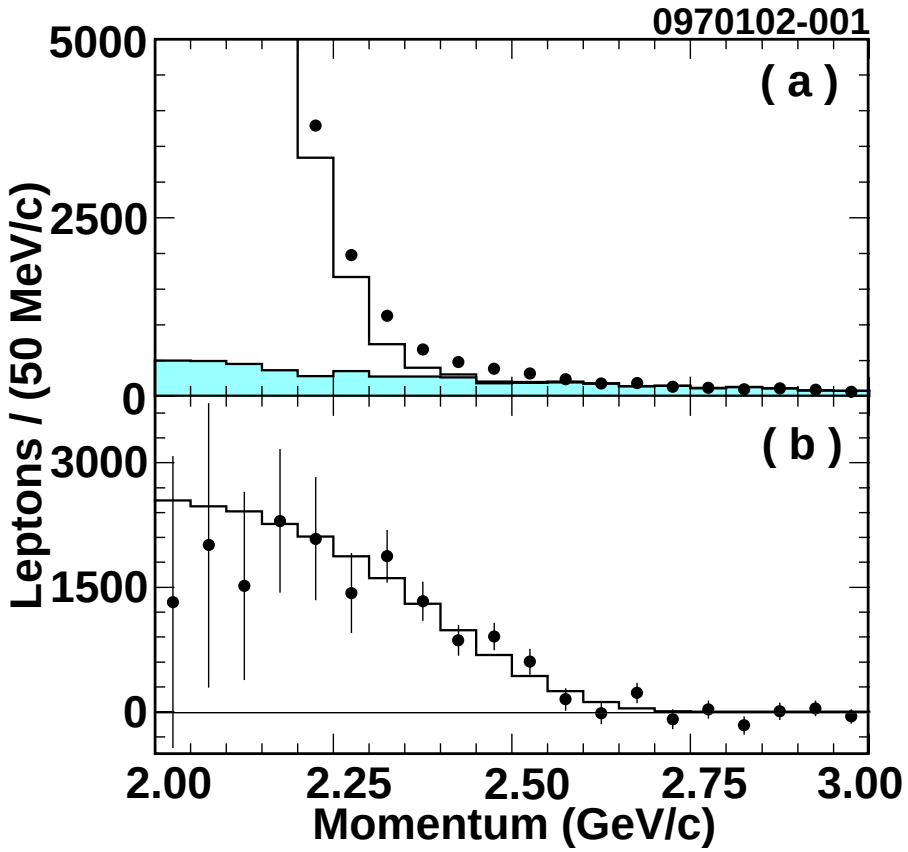

Figure 4.20: (a) Lepton spectra for ON (filled circles) and scaled OFF (shaded histogram) data with the neural-net continuum suppression applied. The solid histogram is the sum of the scaled OFF and B-decay backgrounds. (b) Background-subtracted, efficiency-corrected lepton spectrum attributed to $B \to X_u \ell \nu$. The error bars represent combined statistical and systematic uncertainties. The curve gives the $B \to X_u \ell \nu$ predicted with the measured $B \to X_s \gamma$ spectrum, as is described in the text.

CHAPTER 5

Calculating $|V_{ub}|$

5.1 Partial Branching Fractions

The partial branching fraction for $B \to X_u \ell\nu$ ($\ell = e$ **or** μ) in a given momentum interval Δp is given by

$$\Delta\mathcal{B}_u(\Delta p) = \frac{N_\ell(\Delta p)}{2N_{B\bar{B}}\epsilon(\Delta p)}, \tag{5.1}$$

where $\epsilon(\Delta p)$ is the total efficiency for detecting leptons in the momentum range (Chap. 3), and $N_\ell(\Delta p)$ is half of the total yield of electrons and muons (Chap. 4). $N_{B\bar{B}}$ is the number of $B\bar{B}$ events in our sample, which was calculated from the hadronic-event yield [85] and the measured integrated luminosity [86].

Hadronic events were counted run by run, where a run corresponded to a single fill of CESR. For this purpose, all events passing the general event criteria described in Sect. 3.2 were classified as hadronic. The contributions of events other than e^+e^- interactions, including beam-wall and beam-gas collisions, were estimated using events that passed all of the event-selection criteria except for the event z-vertex cut. The background-subtracted hadronic-event yields were then divided by luminosity measurements made with well-understood QED events ($e^+e^- \to e^+e^-$, $e^+e^- \to \mu^+\mu^-$ and $e^+e^- \to \gamma\gamma$) to obtain the cross section. The resulting hadronic cross sections were

grouped according to time periods during which CLEO and CESR configurations were stable. Average hadronic cross sections were computed for ON and OFF runs, and the difference between these was taken to be the $\Upsilon(4S)$ cross section, which was combined with the total ON integrated luminositiy to get $N_{B\bar{B}}$. For the entire CLEO II and II.V data sample, we found

$$N_{B\bar{B}} = (9.665 \pm 0.174) \times 10^6. \tag{5.2}$$

Using Eq. 5.1 to combine the lepton yields in Tables 4.11-4.15, the efficiencies in Table 3.3 and the $B\bar{B}$ count in Eq. 5.2 leads to the partial branching fractions listed in Table 5.1.

Table 5.1: Partial branching fractions for five overlapping momentum intervals in the end-point region. The first errors are statistical, the second are systematic.

Momentum Interval (GeV/c)	$\Delta\mathcal{B}_u(10^{-4})$
$2.0 \leq p_\ell < 2.6$	$4.22 \pm 0.33 \pm 1.78$
$2.1 \leq p_\ell < 2.6$	$3.37 \pm 0.23 \pm 0.74$
$2.2 \leq p_\ell < 2.6$	$2.33 \pm 0.15 \pm 0.35$
$2.3 \leq p_\ell < 2.6$	$1.43 \pm 0.10 \pm 0.13$
$2.4 \leq p_\ell < 2.6$	$0.64 \pm 0.07 \pm 0.05$

5.2 The Spectral Fractions f_u

In order to calculate $|V_{ub}|$ using Eq. 1.36, we must determine the fraction of the $B \to X_u \ell \nu$ lepton spectrum f_u in each of the momentum intervals in Table 5.1. For a given momentum interval Δp, the total branching fraction is given by

$$\mathcal{B}_u(\Delta p) = \frac{\Delta \mathcal{B}_u(\Delta p)}{f_u(\Delta p)} \tag{5.3}$$

Determination of f_u was previously done with theoretical models and is the source of much of the model dependence in earlier inclusive determinations of $|V_{ub}|$. For this thesis we replace models with the relationship between the $B \to X_s \gamma$ photon-energy spectrum and the lepton-momentum spectrum from $B \to X_u \ell \nu$ discussed in Sect. 1.3.2. Before detailing the fits to the E_γ spectrum that lead to f_u estimates, we briefly review the experimental methods used to measure the spectrum.

5.2.1 $B \to X_s \gamma$ Inclusive E_γ Spectrum Measurement

At the $\Upsilon(4S)$, the $B \to X_s \gamma$ photon-energy spectrum extends from around 2.0 to 2.7 GeV. The inclusive measurement of this spectrum at CLEO [27, 87] is very similar to the lepton-spectrum measurement described in Chapter 3 of this thesis. For the majority of photon energies, the dominant background is continuum production of photons through initial-state radiation and π^0 and η decays. Continuum suppression therefore plays a central role in the analysis. Non-signal-mode production of photons in B decays is a smaller background, but it is difficult to estimate and is an important limitation on the measurement near the lower end of the spectrum.

Continuum suppression was achieved partly through the consideration of event shape, in a manner very similar to the approach described in Sect. 3.2.5. Shape variables, including R_2 and the energy flow into cones opening about the photon's direction, were combined into a single variable r with a neural net.

In addition to this, each event was searched for a reconstructable $B \to X_s\gamma$ decay. X_s candidates were constructed from kaons, either charged tracks consistent with being $K_s \to \pi^+\pi^-$ or $K^\pm$, and one to four pions, of which at most one could be a π^0. A B candidate's energy E and momentum $\vec{p}$ were then formed by combining the X_s and photon momenta. A "beam-constrained mass" was computed from $\vec{p}$ and the beam energy E_{beam}:

$$M = \sqrt{E_{beam}^2 - |\vec{p}|^2}. \tag{5.4}$$

Candidate B decays were evaluated using a chi-squared defined as

$$\chi_B^2 = \left(\frac{E - E_{beam}}{\sigma_E}\right)^2 + \left(\frac{M - M_B}{\sigma_M}\right)^2, \tag{5.5}$$

where $\sigma_E = 40$ MeV and $\sigma_M = 4.0$ MeV were determined with Monte Carlo studies. Candidates were considered acceptable if $\chi_B^2 < 20$. If an event had multiple acceptable candidates, the one with the smallest χ_B^2 was used. The thrust axis [88] of the candidate B was also calculated and used to compute $|\cos\theta_{tt}|$, where θ_{tt} is the angle between the B's thrust axis and the thrust axis of the rest of the event. This quantity is expected to be flat for signal and peaked near one for continuum background.

Finally, if an event contained an electron or muon, both the magnitude of its momentum (P_ℓ) and the angle between its direction and that of photon ($\theta_{\ell\gamma}$) were added to the list of continuum-suppression variables. Events were divided into the

following four categories:

1. Those having both a reconstructable $B \to X_s\gamma$ decay and a lepton.

2. Those having only a reconstructable $B \to X_s\gamma$ decay.

3. Those having only a lepton.

4. Those having neither a reconstructable $B \to X_s\gamma$ decay nor a lepton.

For each event category, a separate neural net was used to combine the following variables:

1. r, χ^2_B, $|\cos\theta_{tt}|$, P_ℓ, and $\theta_{\ell\gamma}$.

2. r, χ^2_B, and $|\cos\theta_{tt}|$.

3. r, P_ℓ, and $\theta_{\ell\gamma}$.

4. r.

Each net was trained using signal and background Monte Carlo samples.

Rather than cutting on the net output of each of the nets, r_j, statistics were maintained by converting the outputs into *weights* $w_j = s(r_j)/[s(r_j) + (1+\alpha)b(r_j)]$, where $s(r_j)$ and $b(r_j)$ are the expected yields, calculated with Monte Carlo, of signal and continuum background for a particular net output r_j. The quantity α is the luminosity scale factor between the ON and OFF samples. Weights so defined were summed over ON and OFF data and a continuum subtraction was performed.

Remaining backgrounds from other B-decay processes were investigated using $B\bar{B}$ Monte Carlo. The largest sources of background were π^0 and η decays, and

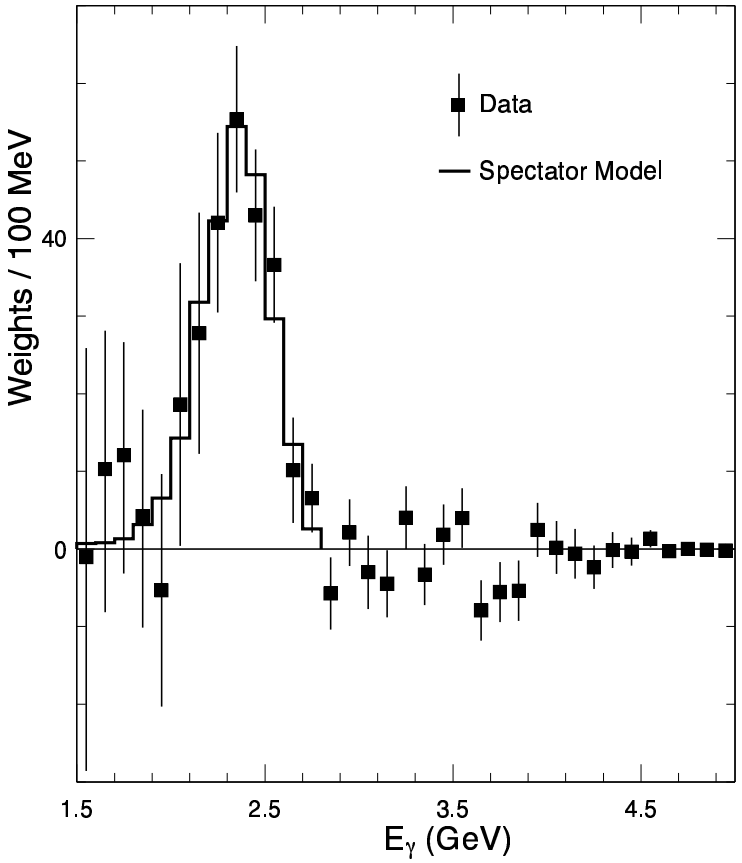

Figure 5.1: Continuum- and background-subtracted photon-energy spectrum for $B \to X_s\gamma$. The histogram represents a spectator-model fit to the data.

data was used to tune Monte Carlo π^0 and η yields, as well as those for ω and η'. Backgrounds from K_L decays and $\bar{n}$ interactions were determined by fits of calorimeter shower-shape distributions in Monte Carlo to those in data. Backgrounds from other B-decay processes thus determined were subtracted from the continuum-subtracted weight distribution, and the resulting spectrum, along with a fit to the Monte Carlo spectrum generated using the spectator model of Ali and Greub [89], is shown in Fig. 5.1.

5.2.2 Fitting the E_γ Spectrum

The $B \to X_s\gamma$ photon-energy distribution was fitted over the E_γ range $1.5 - 2.8$ GeV [28]. This was done by first generating a $B \to X_s\gamma$ hadronic-mass spectrum with a parton-level calculation [26], a particular choice for the values of the HQ-expansion parameters λ_1 and $\bar{\Lambda}$, and one of the three shape functions, as discussed in Sect. 1.3.2. This spectrum was used to reweight fully-simulated $B \to X_s\gamma$ Monte Carlo in M_{X_s}, giving an E_γ spectrum in the lab frame correctly including efficiency and resolution effects. This was then fitted to the data spectrum in Fig. 5.1. Only the normalization of the simulated spectrum was allowed to float in the fit, and the resulting χ^2 measured how well the shapes of the two spectra agreed. The same shape function and λ_1-$\bar{\Lambda}$ pair were used, along with a parton-level calculation of the lepton-momentum spectrum [24], to generate a $B \to X_u\ell\nu$ spectrum from which the fractions f_u were directly calculable.

The E_γ-fitting procedure and f_u calculations were repeated for a wide range of λ_1-$\bar{\Lambda}$ pairs until the best-fit function was found. This, along with a set of pairs that formed a 1σ error ellipse in the λ_1-$\bar{\Lambda}$ plane, was used to estimate f_u with statistical errors. Fig. 5.2 shows the best-fit result and error ellipse in the λ_1-$\bar{\Lambda}$ plane for the fits done with the exponential shape function of Ref. [26]. The fitting procedure was repeated for each of the three shape-function parameterizations, and resulting f_u estimates were averaged. The results are shown in Table 5.2.

Several different sources of systematic error on f_u were considered. The effect of uncertainty in the $B\bar{B}$-background estimation was explored by varying the size of the subtracted background spectrum by $\pm 1\sigma$ and determining the λ_1-$\bar{\Lambda}$ pair that best

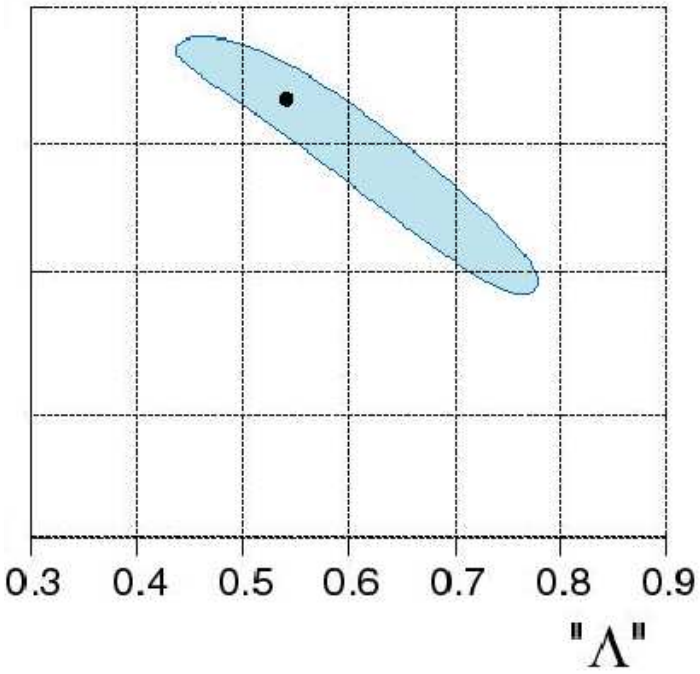

Figure 5.2: The central value (point) and 1σ error ellipse in the λ_1-$\bar{\Lambda}$ plane from fits to the measured $B \to X_s\gamma$ photon-energy spectrum. The fits were done with theoretical spectra generated using the exponential shape function.

Table 5.2: Fractions of the $B \to X_u \ell \nu$ momentum spectrum in five overlapping intervals in the end-point region, as determined from fits to the $B \to X_s \gamma$ photon-energy spectrum. The first error is statistical. The second error reflects differences among the shape functions, uncertainties in subtracting B-decay backgrounds from the photon spectrum and the scale for evaluating α_s. The third error is associated with the theoretical assumption that the same shape funcion $F(k_+)$ can be used for both decays.

Momentum Interval (GeV/c)	f_u
$2.0 \leq p_\ell < 2.6$	$0.278 \pm 0.043 \pm 0.025 \pm 0.017$
$2.1 \leq p_\ell < 2.6$	$0.207 \pm 0.037 \pm 0.020 \pm 0.017$
$2.2 \leq p_\ell < 2.6$	$0.137 \pm 0.025 \pm 0.016 \pm 0.016$
$2.3 \leq p_\ell < 2.6$	$0.078 \pm 0.015 \pm 0.009 \pm 0.013$
$2.4 \leq p_\ell < 2.6$	$0.039 \pm 0.008 \pm 0.003 \pm 0.009$

fitted the new spectrum. The difference between the f_u values obtained with these best fits was used to estimate the resulting systematic error. Perturbative corrections to the predicted spectrum were also varied by changing the scale at which the strong coupling constant α_s was evaluated. The nominal scale μ used in evaluating the strong coupling constant was m_b. Alternative sets of fits were done for values of α_s evaluated at $\mu = m_b/2$ and $\mu = 2m_b$. The resulting systematic error was obtained by using the difference between the spectral fractions obtained with the best-fit shape functions for the alternative α_s points. This error is quite small, as variation from α_s changes was largely compensated by the variation in λ_1 and $\bar{\Lambda}$ required to obtain the best fit in each case. Table 5.2 shows the total systematic error due to variation in the shape-function parameterization, $B\bar{B}$-background subtraction, and perturbative corrections.

We also estimated the theoretical error in f_u due to the HQ-theory assumption that the photon-energy spectrum from $B \to X_s\gamma$ can be used to compute the lepton-momentum spectrum from $B \to X_u\ell\nu$. This is of order Λ_{QCD}/M_B for intervals beginning close to the $B \to X_u\ell\nu$ end point and changes to order $(\Lambda_{QCD}/M_B)^2$ when more of the spectrum is included [90]. Although there is at present no rigorous recipe for evaluating this uncertainty, we followed a suggestion from Neubert that it could be estimated by varying the shape-function parameters by $\pm 10\%$. The resulting variations in f_u are presented as the third error in Table 5.2. While the adequacy of this estimate of the uncertainty remains to be determined, it is encouraging that these uncertainties are overshadowed by statistical errors in all but the smallest momentum intervals. We are hopeful that continued theoretical work will clarify the status of

this approach and lead to a better estimation of both this uncertainty and that due to the duality assumption, which remains unquantified.

5.3 Branching Fraction Measurements

The prescription for computing the $B \to X_u \ell \nu$ spectrum and f_u in Ref. [24] does not include the effect of QED-radiative corrections. These slightly reduce the yield of leptons in the measured momentum ranges. We have estimated this effect by comparing lepton yields in ISGW2 signal Monte Carlo generated with and without PHOTOS [82]. We divided our partial branching fractions by the resulting "efficiencies," which are shown in Table 5.3. We include an uncertainty of ± 0.02 (one third to one half of the observed effect), a conservative assumption considering that the PHOTOS algorithm has been observed to agree to better than 10% with analytic calculations of the effects of QED radiation in other processes (see Sect. 4.2.5).

We combine the partial braching fractions in Table 5.1, the spectral fractions in Table 5.2, and the QED-radiative corrections in Table 5.3 to get the branching fractions shown in Table 5.4. Each result is quoted with three errors. The first is from the combined statistical and systematic error on the yield measurement for each interval. The second is derived from the combination of the statistical error on f_u and the systematic errors due to the difference between shape-function parameterizations, $B\bar{B}$ subtraction uncertainty and the perturbative corrections. The third uncertainty comes from the error on f_u due to the non-universality of the shape function, which we choose to keep separate because of the preliminary nature of its evaluation.

Table 5.3: Ratios of the amounts, in a given momentum interval, of simulated $b \to u\ell\nu$ events generated with PHOTOS to those made without QED-radiative corrections.

Momentum Interval (GeV/c)	ϵ_{IB} ($\pm$0.02)
$2.0 \leq p_\ell < 2.6$	0.96
$2.1 \leq p_\ell < 2.6$	0.96
$2.2 \leq p_\ell < 2.6$	0.95
$2.3 \leq p_\ell < 2.6$	0.94
$2.4 \leq p_\ell < 2.6$	0.94

Table 5.4: $B \to X_u\ell\nu$ branching fractions for five overlapping momentum intervals in the end-point region. The first errors are from the yield measurements for each interval. The second are derived from the f_u estimations, excluding the uncertainties due to the non-universality of the shape function, which are presented as the third errors.

Momentum Interval (GeV/c)	$\mathcal{B}_u(10^{-3})$
$2.0 \leq p_\ell < 2.6$	$1.59 \pm 0.68 \pm 0.28 \pm 0.10$
$2.1 \leq p_\ell < 2.6$	$1.66 \pm 0.39 \pm 0.34 \pm 0.13$
$2.2 \leq p_\ell < 2.6$	$1.77 \pm 0.29 \pm 0.38 \pm 0.21$
$2.3 \leq p_\ell < 2.6$	$1.94 \pm 0.22 \pm 0.43 \pm 0.31$
$2.4 \leq p_\ell < 2.6$	$1.74 \pm 0.24 \pm 0.38 \pm 0.38$

5.4 $|V_{ub}|$ Calculation

We use Eq. 1.36 to calculate $|V_{ub}|$ from the branching fractions in Table 5.4. We average the charged and neutral B lifetimes and use $\tau_B = 1.60 \pm 0.02$ ps [3] in the calculations. Table 5.5 contains the results. Each value of $|V_{ub}|$ is quoted with four errors. The first three come from the branching-fraction errors in Table 5.4. The fourth reflects the uncertainty in Eq. 1.36, both in its theoretical derivation and in τ_B.

Fig. 5.3 shows our values of $|V_{ub}|$ and their combined quoted errors versus lower-lepton-momentum cut-off. There is an approximately 10% variation in $|V_{ub}|$ as the cut-off momentum is changed from 2.0 to 2.4 GeV/c, with a trend toward smaller values at lower cut-offs. The total quoted error is fairly consistent among the intervals, and easily contains the spread in the central values of $|V_{ub}|$. Table 5.5 clearly shows how, as the cut-off is lowered, competing trends in the different sources of error compensate for one another. There is essentially no $B \to X_c \ell \nu$ background above 2.4 GeV/c, and here the error due to our $\Delta\mathcal{B}$ measurement is the smallest. The error due to f_u is largest for this interval, however, since it is difficult to precisely determine this small spectral fraction. The largest interval, beginning at 2.0 GeV/c, has the largest error due to uncertainty in $\Delta\mathcal{B}$ since the $b \to c$ subtraction is enormous here. The spectral fraction, on the other hand, is the largest and best-determined for this interval. We decided in advance to use the 2.2 to 2.6 GeV/c number as our final result for $|V_{ub}|$, since it falls in the middle of these two trends. We therefore quote

Table 5.5: Values of $|V_{ub}|$ computed for five overlapping momentum intervals in the end-point region. The first error quoted on each of the values is from the uncertainty of the partial branching fraction measurement, the second is from the combination of the statistical error on f_u and its systematic errors due to the difference between shape-function parameterizations, $B\bar{B}$-subtraction uncertainty and perturbative corrections. The third uncertainty comes from the error on f_u due to the non-universality of the shape function, and the fourth error reflects the uncertainty in Eq. 1.36, both in its theoretical derivation and in the B lifetime used in its evaluation.

Momentum Interval (GeV/c)	$V_{ub}(10^{-3})$
$2.0 \leq p_\ell < 2.6$	$3.87 \pm 0.83 \pm 0.35 \pm 0.12 \pm 0.15$
$2.1 \leq p_\ell < 2.6$	$3.95 \pm 0.46 \pm 0.40 \pm 0.16 \pm 0.16$
$2.2 \leq p_\ell < 2.6$	$4.08 \pm 0.34 \pm 0.44 \pm 0.24 \pm 0.16$
$2.3 \leq p_\ell < 2.6$	$4.27 \pm 0.24 \pm 0.47 \pm 0.34 \pm 0.17$
$2.4 \leq p_\ell < 2.6$	$4.05 \pm 0.28 \pm 0.45 \pm 0.45 \pm 0.16$

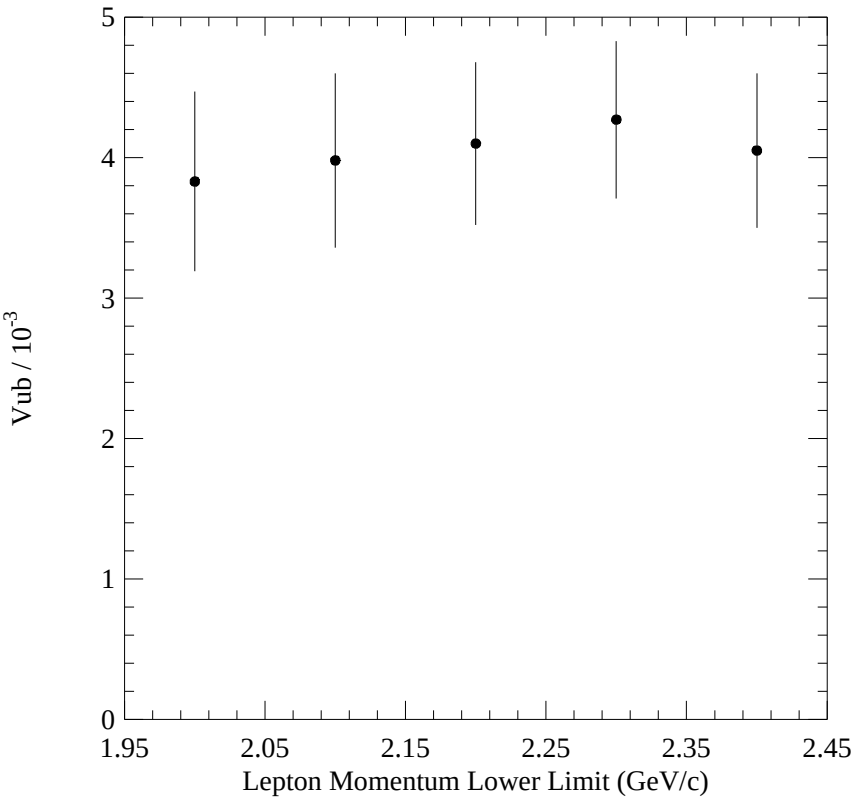

Figure 5.3: $|V_{ub}|$ versus lower-lepton-momentum cut-off. The error bars reflect the combination in quadrature of the errors listed in Table 5.5.

$$|V_{ub}| = (4.08 \pm 0.34 \pm 0.44 \pm 0.24 \pm 0.16) \times 10^{-3}. \quad (5.6)$$

Contributions to the uncertainty in the $|V_{ub}|$ determination are summarized in Table 5.6. The error on f_u is broken into three components: (1) the statistical error from the $B \to X_s\gamma$ fits; (2) the systematic error due to the differences among the different shape functions used, the uncertainty in the $B\bar{B}$-background subtraction, and the choice of scale for evaluation of α_s (Systematic A); and (3) the error due to the Heavy Quark theoretical uncertainty (Systematic B). Statistical uncertainty on f_u is the largest contributor to our total error, while next largest components, the systematic errors on f_u and on the $B \to X_c\ell\nu$ subtraction, are all about the same size.

5.4.1 Model-Based Calculations

For comparison, we calculated the spectral fraction for the $2.2 - 2.6$ GeV/c interval using both the ISGW2 and ACCMM models. We used values for the ACCMM parameters that were assumed in past studies: a spectator mass (m_{sp}) of 150 MeV/c^2 and a Fermi momentum (p_F) of 300 MeV/c. Both models led to $|V_{ub}|$ values that were $\sim$20% lower than our result. This indicates that the inclusive spectrum is softer than previous expectations. We also tried using a set of ACCMM-parameter values obtained with a fit of the Ali and Greub spectator model to the $B \to X_s\gamma$ photon spectrum: $m_{sp} \simeq$230 MeV/c^2 and $p_F \simeq$440 MeV/c. The result was a $|V_{ub}|$ value that was only 5% lower than the result given in Sect. 5.4.

Table 5.6: Sources of systematic uncertainty in the measurement of $|V_{ub}|$, in units of 10^{-3}. Details regarding the three f_u errors are given in the text.

Source	Contribution
Yield Statistical	± 0.131
$B \to X_c \ell \nu$ Systematic	± 0.264
Other Backgounds Systematic	± 0.075
Efficiency - Detector Systematic	± 0.107
Efficiency - $B \to X_u \ell \nu$ Systematic	± 0.097
Uncertainty in Eq. 1.36	± 0.162
f_u Statistical	± 0.372
f_u Systematic A	± 0.233
f_u Systematic B	± 0.245
Overall	± 0.63

5.5 Conclusions

We have presented a new measurement of the CKM parameter $|V_{ub}|$ made with an observation of the inclusive spectrum of electrons and muons from charmless semileptonic B decays at the $\Upsilon(4S)$. We made the first use of Heavy Quark theory to combine the observed lepton yield in the momentum interval $2.2 - 2.6$ GeV/c and CLEO's recent measurement of the $B \to X_s\gamma$ photon-energy spectrum to determine $|V_{ub}|$ without relying on phenomenological models. The result,

$$|V_{ub}| = (4.08 \pm 0.63) \times 10^{-3}, \tag{5.7}$$

has a combined fractional uncertainty ($\sim$15%) that is smaller than those of previous measurements. We repeated the calculation for intervals having lower lepton-momentum limits as large as 2.4 GeV/c and as small as 2.0 GeV/c. We found that our result is stable with respect to these variations in end-point interval, an observation that helps to validate our overall approach.

5.5.1 Comparisons With Previous Measurements

In comparing our new result with those of the past, we begin with CLEO's previous inclusive measurement [16]. The most direct comparison that can be made here is for $\Delta\mathcal{B}_u$. The new measurement for $2.3 \leq p_l \leq 2.6$ GeV/c, $(1.43 \pm 0.10 \pm 0.13) \times 10^{-4}$, can be compared with the previous result for this interval, $(1.21 \pm 0.17 \pm 0.15) \times 10^{-4}$. Although the results are consistent, some caution is appropriate in comparing the errors. For the previous measurement, the continuum was subtracted using fits to the OFF spectrum. We no longer use this method but instead do a more straightforward

direct subtraction. Thus, the statistical error of the new result is reduced by less than the factor of 3 expected on the basis of statistics. The systematic error of the previous result included a sizable contribution due to variation among the functional forms used in the continuum fits, but it certainly underestimated the error in the $B \to X_c \ell \nu$ subtraction, since it did not account for the form-factor uncertainties and other sources of error that we now recognize as quite significant.

Fig. 5.4 shows a graphical comparison of CLEO and other $|V_{ub}|$ measurements from the last decade. For this purpose, the 1993 CLEO inclusive result $|V_{ub}|/|V_{cb}| = 0.08 \pm 0.02$ was converted to $|V_{ub}|$ by using a value for $|V_{cb}|$ of $(40.4 \pm 1.3 \pm 0.9) \times 10^{-3}$, an average of LEP and CLEO results used by the CKMFitter group [91] in December of 2001 [92].

Fig. 5.4 also shows the results of two exclusive measurements made by CLEO. The first, from 1996 [93], was made with observations of semileptonic B decays to $\pi^{\pm}$, π^0, $\rho^{\pm}$, and ρ^0. The analysis technique used strict event-selection requirements that enabled the "reconstruction" of the neutrino in each decay from the event's missing energy and momentum. The neutrino's momentum was then combined with those of the lepton and the candidate hadron to make a signal B candidate. Extraction of $|V_{ub}|$ from the measured signal-mode branching fractions required knowledge of each decay's form factors, and it was the theoretical uncertainty in these that limited the approach. In 2000 an updated $B \to \rho \ell \nu$ measurement was made with somewhat looser event requirements and roughly one third more data [94]. The result was combined with the 1996 measurement to obtain the value shown in Fig. 5.4.

In addition to the CLEO $|V_{ub}|$ measurements shown in Fig. 5.4, there are four

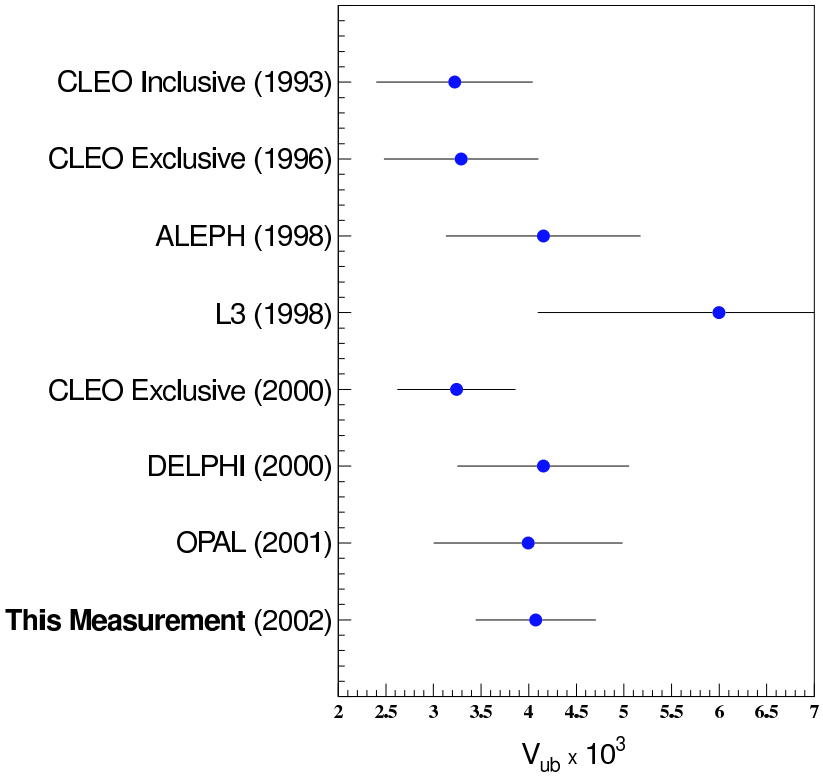

Figure 5.4: A comparison of measured values of $|V_{ub}|$ from the last decade. The horizontal axis is in units of 10^{-3}. The values labeled "CLEO Inclusive (1993)" and "DELPHI (2000)" have been converted from measurements of the ratio $|V_{ub}|/|V_{cb}|$ with the value of $|V_{cb}|$ listed in Table 5.7.

results from the LEP experiments: ALEPH [95], L3 [96], DELPHI [97], and OPAL [98]. (DELPHI measured the ratio $|V_{ub}|/|V_{cb}|$. The corresponding $|V_{ub}|$ constraint was computed with the same value of $|V_{cb}|$ used for the early CLEO inclusive measurement just discussed.) Although the details of the individual analyses differ somewhat, they are all inclusive measurements performed using $e^+e^- \to b\bar{b}$ interactions at the Z^0. At these energies, b hadrons are formed in jets that are back-to-back in the center-of-mass frame. This separation allows the estimation of the neutrino momentum in a semileptonic decay using a jet's missing momentum. Isolating semileptonic B decays is challenging, however, because not all of the available energy in an event is carried by the b hadrons. On average, about 30% of a b jet's energy is carried by fragmentation products, diluting the signal. All four experiments used particles' momenta and relative proximity to the candidate lepton and the event's primary vertex to reject fragmentation products and form hadronic systems X in their $B \to X\ell\nu$ candidates. Of course, removing $B \to X_c\ell\nu$ was a significant challenge. Each experiment used kinematic constraints to reject charmed final states as much as possible, and estimated the significant remaining background using Monte Carlo. Models used for this purpose included ACCMM and, in some cases, form-factor calculations like ISGW2. Systematic error estimates of this background did not include effects, such as HQET form-factor variations, that we now know to be significant. Although each experiment retained efficiency across most of the lepton spectrum, the criteria they used did not have acceptances that were uniform over phase space. Signal efficiencies were estimated using models, including the ACCMM model with internal parameters that we now understand to be incorrect.

Very different analysis procedures and event environments are represented in the eight measurements shown in Fig. 5.4. Their good agreement reinforces the notion that we know the value of $|V_{ub}|$ to within $\sim$15%.

5.5.2 Implications of the Measurement

Our new value of $|V_{ub}|$ constrains the position of the upper vertex of the unitarity triangle in Fig. 1.3. In the Wolfenstein parameterization of the CKM matrix (Eq. 1.7), the ratio $|V_{ub}|/|V_{cb}|$ is given by

$$\begin{aligned} \frac{|V_{ub}|}{|V_{cb}|} &= \frac{A\lambda^3|(\rho - i\eta)|}{A\lambda^2} \\ &= \lambda(\rho^2 + \eta^2)^{1/2}. \end{aligned} \tag{5.8}$$

Since $\lambda = 0.22$, values of $|V_{ub}|$ and $|V_{cb}|$ together provide a circular constraint in the ρ-η plane.

To determine how our new measurement of $|V_{ub}|$ fits in with other experimental constraints on the unitarity triangle, we used the global fitting package developed and maintained by the CKMFitter group [91]. This software takes as its inputs experimental constraints on CKM matrix elements and performs a global fit in the $\bar{\rho}$-$\bar{\eta}$ plane to constrain the location of the upper vertex of the unitarity triangle. (The parameters $\bar{\rho}$ and $\bar{\eta}$ are forms of Wolfenstein's parameters ρ and η that have been rescaled to account for $\mathcal{O}(\lambda^4)$ corrections.) We obtained a copy of the package that included values of experimental constraints from the summer of 2001 [92], replaced its $|V_{ub}|$ value with our new result, and performed a fit. All other inputs to the fit were kept to the values listed in Ref [92].

Fig. 5.5 shows a set of individual constraints on the position of the unitarity triangle's upper vertex. The lines in Fig. 5.5 labeled "$|V_{ub}/V_{cb}|$," "Δm_d," "$\Delta m_s/\Delta m_d$," and "$|\epsilon_K|$" bound 95% confidence intervals from these constraints. Experimental inputs used in their calculation are presented in Table 5.7. The precision of our $|V_{ub}|$ result dominates the width of the $|V_{ub}|/|V_{cb}|$ constraint, an annulus centered on the point $(0, 0)$. The quantity Δm_d is the B_d-$\bar{B}_d$ mass difference derived from B_d-$\bar{B}_d$ mixing observations. It constrains $|V_{td}|$ and gives rise to an annulus centered on the point $(0, 1)$. The experimental lower limit on the B_s-$\bar{B}_s$ mass difference Δm_s can be combined with Δm_d to generate a more stringent upper limit on $|V_{td}|$, which gives rise to the line labeled "$\Delta m_s/\Delta m_d$," in the figure. The CP-violating parameter ϵ_K in the neutral K system gives rise to the figure's hyperbolic bounds. Finally, the shaded wedges originating at $(0, 1)$ represent 1σ and 2σ contours coming from the world average experimental value of $\sin 2\beta$. The average used here is dominated by the BaBar and BELLE experiments' observation of a CP-violating asymmetry in the neutral B system.

All constraints clearly overlap in the upper-right-hand quadrant of the $\bar{\rho}$-$\bar{\eta}$ plane, showing that the Standard Model remains quite adequate in its treatment of the CP-violating sector of weak decays. The irregular contours in the region of overlap are the 5% and 95% contours for the combined fit done with the CKMFitter package. They should be taken only as further evidence that current experimental constraints are consistent with the Standard Model, and we leave a detailed analysis of the fit results to the CKMFitter group.

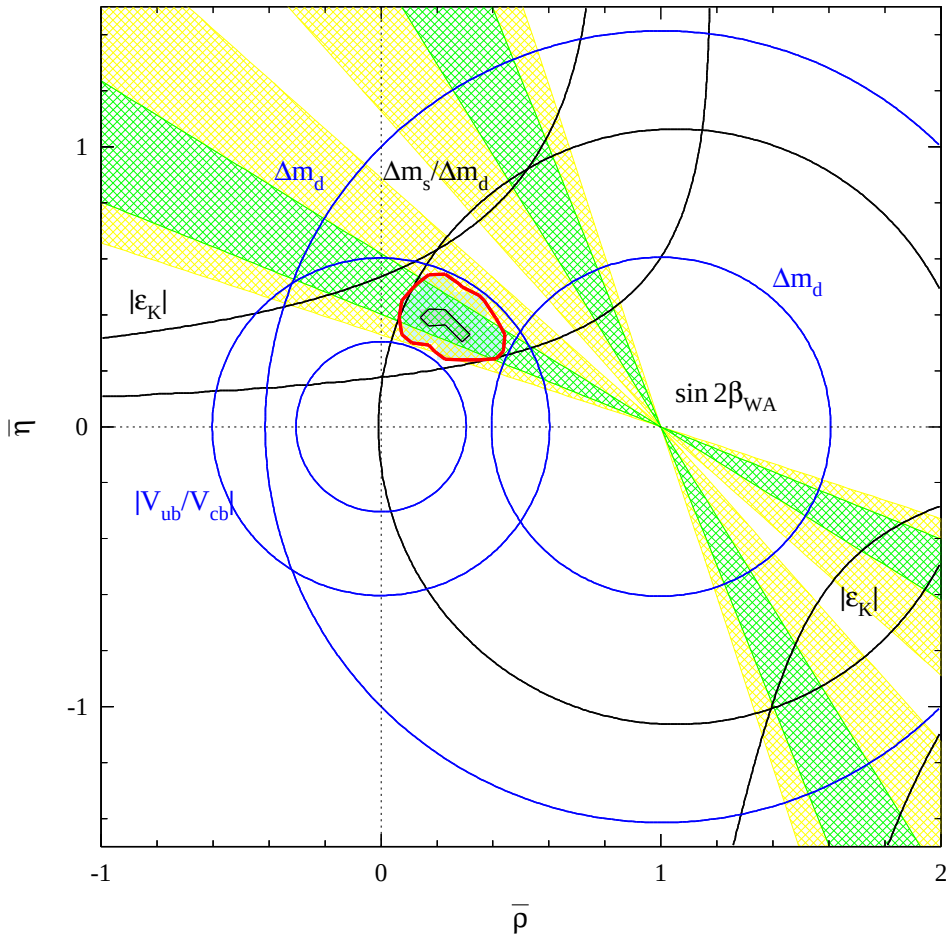

Figure 5.5: Constraints in the $\bar{\rho}$-$\bar{\eta}$ plane from the experimental inputs to the CKMFitter. Shown are 5% confidence levels from indivual constraints labeled as $|V_{ub}/V_{cb}|$, Δm_d, $\Delta m_s/\Delta m_d$, and $|\epsilon_K|$. The shaded wedges represent 1σ and 2σ contours on the angle β. Our new measurement of $|V_{ub}|$ was used to derive the $|V_{ub}/V_{cb}|$ contour shown. The irregular contours represent the 5% and 95% CLs for the global fit done with the CKMFitter package.

Table 5.7: Inputs to the CKMFitter

Input Parameter	Value
$\|V_{ub}\|$	$(4.08 \pm 0.63) \times 10^{-}3$
$\|V_{cb}\|$	$(40.4 \pm 1.3 \pm 0.9) \times 10^{-3}$
Δm_d	$(0.489 \pm 0.008) ps^{-1}$
Δm_s	$> 15.0 ps^{-1}$ at 95% C.L.
$\|\epsilon_K\|$	$(2.271 \pm 0.017) \times 10^{-3}$
$\sin 2\beta$	0.793 ± 0.102

5.5.3 Outlook for $|V_{ub}|$ Measurements

There are good prospects for further improvement in $|V_{ub}|$ measurements made with the inclusive-end-point approach used in this thesis. Most of the errors that dominate our overall uncertainty should improve as the large data sets of the B factories BELLE and BaBar continue to be exploited. The largest uncertainty in Table 5.6 comes from the variation in f_u allowed by the statistical uncertainty in the $B \to X_s\gamma$ photon-energy spectrum. Therefore, a higher-statistics measurement of the E_γ spectrum should allow for reduction in this error. It may also be possible to improve experimental constraints on the $B\bar{B}$ backgrounds to radiative B decay, included in "f_u Systematic A" in Table 5.6. The largest systematic uncertainty in the end-point yield measurement, that due to the estimate of the $B \to X_c\ell\nu$ background, has a large component from the uncertainties in the $B \to D^{(*)}\ell\nu$ form factors. Current measurements of these factors are statistics-limited and will be improved upon with

the larger data samples available to the B factories.

With their big data samples and boosted centers-of-mass, the B factories will be able to employ alternative inclusive approaches to isolating $B \to X_u \ell \nu$ decays. For example, in several years they will have large samples of $B\bar{B}$ events with one fully-reconstructed B meson. Such events will provide new kinematic constraints, improved neutrino-momentum resolutions, and increasingly precise measurements of the hadronic-recoil-mass (M_X) spectrum. It has been suggested that the use of combined cuts on q^2 and M_X to reject $B \to X_c \ell \nu$ could lead to a measurement of $|V_{ub}|$ with calculable errors at the 5 to 10% level [99].

Exclusive approaches to $|V_{ub}|$ measurement, in which specific hadronic final states are selected, remain limited by theoretical uncertainties in form-factor calculations. High statistics data samples may help by allowing the measurement of differential decay distributions that could discriminate among decay models. Improved Lattice QCD calculations tuned with, among other things, D-decay measurements made with the upcoming CLEO-c experiment [100] should provide significantly improved understanding of exclusive form factors and probably the best measurement of $|V_{ub}|$.

BIBLIOGRAPHY

[1] D. Griffiths. *Introduction to Elementary Particles.* John Wiley & Sons, New York (1987).

[2] P. Renton. *Electroweak Interactions: An Intronduction to the Physics of Quarks and Leptons.* Cambridge University Press, Cambridge (1990).

[3] D. E. Groom *et al.* (Particle Data Group). Eur. Phys. J. C **15**, 1 (2000).

[4] M. Kobayashi and T. Maskawa. Prog. Theor. Phys. **49**, 652 (1973).

[5] Y. Fukuda *et al.* (Super-Kamiokande). Phys. Rev. Lett. **81**, 1562 (1998). `hep-ex/9807003`.

[6] Q. R. Ahmad *et al.* (SNO). Phys. Rev. Lett. **87**, 071301 (2001). `nucl-ex/0106015`.

[7] C. S. Wu *et al.* Phys. Rev. **105**, 1413 (1957).

[8] J. H. Christenson, J. W. Cronin, V. L. Fitch, and R. Turlay. Phys. Rev. Lett. **13**, 138 (1964).

[9] B. Aubert *et al.* (BABAR). Phys. Rev. Lett. **87**, 091801 (2001). `hep-ex/0107013`.

[10] K. Abe *et al.* (Belle). Phys. Rev. Lett. **87**, 091802 (2001). `hep-ex/0107061`.

[11] L. Wolfenstein. Phys. Rev. Lett. **51**, 1945 (1983).

[12] J. D. Richman and P. R. Burchat. Rev. Mod. Phys. **67**, 893 (1995). `hep-ph/9508250`.

[13] A. Ali. Zeit. Phys. C **1**, 25 (1979).

[14] R. Fulton *et al.* (CLEO). Phys. Rev. Lett. **64**, 16 (1990).

[15] H. Albrecht *et al.* (ARGUS). Phys. Lett. B **249**, 359 (1990).

[16] J. Bartelt *et al.* (CLEO). Phys. Rev. Lett. **71**, 4111 (1993).

[17] G. Corbo. Nucl. Phys. **B212**, 99 (1983).

[18] M. Jezabek and J. H. Kuhn. Nucl. Phys. **B320**, 20 (1989).

[19] G. Altarelli, N. Cabibbo, G. Corbo, L. Maiani, and G. Martinelli. Nucl. Phys. **B208**, 365 (1982).

[20] I. I. Y. Bigi, M. A. Shifman, N. Uraltsev, and A. I. Vainshtein. Phys. Lett. B **328**, 431 (1994). hep-ph/9402225.

[21] I. I. Y. Bigi, M. A. Shifman, N. G. Uraltsev, and A. I. Vainshtein. Phys. Rev. Lett. **71**, 496 (1993). hep-ph/9304225.

[22] M. Neubert. Phys. Rev. D **49**, 3392 (1994). hep-ph/9311325.

[23] I. I. Y. Bigi, M. A. Shifman, N. G. Uraltsev, and A. I. Vainshtein. Int. J. Mod. Phys. A **9**, 2467 (1994). hep-ph/9312359.

[24] F. De Fazio and M. Neubert. JHEP **06**, 017 (1999). hep-ph/9905351.

[25] M. S. Alam *et al.* (CLEO). Phys. Rev. Lett. **74**, 2885 (1995).

[26] A. L. Kagan and M. Neubert. Eur. Phys. J. C **7**, 5 (1999). hep-ph/9805303.

[27] S. Chen *et al.* (CLEO). Phys. Rev. Lett. **87**, 251807 (2001). hep-ex/0108032.

[28] D. Cronin-Hennessy, A. Lyon, J. Ernst, J. Thayer, and E. Thorndike. CLEO Internal Note CBX 01-59.

[29] T. Mannel and M. Neubert. Phys. Rev. D **50**, 2037 (1994). hep-ph/9402288.

[30] F. J. Gilman and R. L. Singleton. Phys. Rev. D **41**, 142 (1990).

[31] D. Scora and N. Isgur. Phys. Rev. D **52**, 2783 (1995). hep-ph/9503486.

[32] N. Isgur, D. Scora, B. Grinstein, and M. B. Wise. Phys. Rev. D **39**, 799 (1989).

[33] Z. Ligeti, Y. Nir, and M. Neubert. Phys. Rev. D **49**, 1302 (1994). hep-ph/9305304.

[34] M. Athanas *et al.* (CLEO). Phys. Rev. Lett. **79**, 2208 (1997). hep-ex/9705019.

[35] J. E. Duboscq *et al.* (CLEO). Phys. Rev. Lett. **76**, 3898 (1996).

[36] I. I. Y. Bigi, N. G. Uraltsev, and A. I. Vainshtein. Phys. Lett. B **293**, 430 (1992). hep-ph/9207214.

[37] A. V. Manohar and M. B. Wise. Phys. Rev. D **49**, 1310 (1994). hep-ph/9308246.

[38] M. E. Luke, M. J. Savage, and M. B. Wise. Phys. Lett. B **343**, 329 (1995). hep-ph/9409287.

[39] A. F. Falk, M. E. Luke, and M. J. Savage. Phys. Rev. D **53**, 6316 (1996). hep-ph/9511454.

[40] A. F. Falk (2000). hep-ph/0007339.

[41] A. H. Hoang, Z. Ligeti, and A. V. Manohar. Phys. Rev. D **59**, 074017 (1999). hep-ph/9811239.

[42] N. Uraltsev. Int. J. Mod. Phys. A **14**, 4641 (1999). hep-ph/9905520.

[43] I. I. Y. Bigi and N. Uraltsev. Int. J. Mod. Phys. A **16**, 5201 (2001). hep-ph/0106346.

[44] M. Tigner. IEEE Trans. Nucl. Sci. **24**, 1849 (1977).

[45] S. B. Peck and D. L. Rubin Contributed to IEEE Particle Accelerator Conference (PAC 99), New York, 29 Mar - 2 Apr 1999.

[46] E. Rice *et al.* (CUSB). Phys. Rev. Lett. **48**, 906 (1982).

[47] R. Giles *et al.* (CLEO). Phys. Rev. D **29**, 1285 (1984).

[48] D. Besson *et al.* (CLEO). Phys. Rev. Lett. **54**, 381 (1985).

[49] Y. Kubota *et al.* (CLEO). Nucl. Instrum. Meth. A **320**, 66 (1992).

[50] R. Briere Presented at 7th International Symposium on Heavy Flavor Physics, Santa Barbara, CA, 7-11 Jul 1997.

[51] T. S. Hill. Nucl. Instrum. Meth. A **418**, 32 (1998).

[52] G. Charpak and F. Sauli. Nucl. Instrum. Meth. **162**, 405 (1979).

[53] D. G. Cassel *et al.* Nucl. Instrum. Meth. A **252**, 325 (1986).

[54] E. Blucher *et al.* IEEE Trans. Nucl. Sci. **32**, 716 (1985).

[55] C. Bebek *et al.* Nucl. Instrum. Meth. A **302**, 261 (1991).

[56] K. Kinoshita. Nucl. Instrum. Meth. A **276**, 242 (1989).

[57] D. G. Cassel and H. Kowalski. Nucl. Instr. Meth. **185**, 235 (1981).

[58] R. Kutschke and A. Ryd. CLEO Internal Note CBX 96-20.

[59] S. Roberts, L. Gibbons, and E. Thorndike. CLEO Internal Note CBX 96-103.

[60] R. Brun *et al.* GEANT 3.15 (1987). `CERN Report No. DD/EE/84-1`.

[61] V. Boisvert. CLEO Internal Note CBX 98-70.

[62] J. L. Goity and W. Roberts. Phys. Rev. D **51**, 3459 (1995). `hep-ph/9406236`.

[63] T. Sjostrand (1995). `hep-ph/9508391`.

[64] S. Jadach and Z. Wąs. Comput. Phys. Commun. **64**, 267 (1991).

[65] F. Muheim, J. Nelson, and R. Poling. CLEO Internal Note CBX 93-36.

[66] A. Weinstein. CLEO Internal Note CBX 96-347.

[67] R. Poling, B. Rancourt, T. Riehle, A. Sander, and J. Sankey. CLEO Internal Note (in preparation).

[68] J. Alexander, K. Lingel, S. Playfer, A. Sadoff, J. Smith, and F. Wurthwein. CLEO Internal Note CBX 93-31.

[69] C. Peterson, T. Rognvaldsson, and L. Lonnblad. Comput. Phys. Commun. **81**, 185 (1994).

[70] G. C. Fox and S. Wolfram. Phys. Rev. Lett. **41**, 1581 (1978).

[71] H. Kroha. CLEO Internal Note CBX 91-53.

[72] J. Urheim. CLEO Internal Note CBX 99-53.

[73] B. Gittelman. CLEO Internal Note CBX 93-115.

[74] M. Palmer. Personal communication.

[75] T. Skwarnicki, R. Stroynowski, and G. Wei. CLEO Internal Note CBX 94-72.

[76] M. Artuso and C. Boulahouche. CLEO Internal Note CBX 00-39.

[77] M. Artuso. Phys. Lett. B **311**, 307 (1993).

[78] T. Meyer. Personal communication.

[79] R. Wang. Ph.D. thesis, University of Minnesota (1994).

[80] D. Atwood and W. J. Marciano. Phys. Rev. D **41**, 1736 (1990).

[81] F. Muheim. CLEO Internal Note CBX 92-104.

[82] E. Barberio and Z. Wąs. Comput. Phys. Commun. **79**, 291 (1994).

[83] E. Richter-Wąs. Phys. Lett. B **303**, 163 (1993).

[84] V. Fadeyev. CLEO Internal Note CBX 00-43.

[85] D. Besson. CLEO Internal Note CBX 92-75.

[86] B. Heltsley. CLEO Internal Note CBX 93-95.

[87] J. B. Thayer. Ph.D. thesis, The Ohio State University (2002).

[88] E. Farhi. Phys. Rev. Lett. **39**, 1587 (1977).

[89] A. Ali and C. Greub. Phys. Lett. B **259**, 182 (1991).

[90] M. Neubert. Personal communication.

[91] A. Hocker, H. Lacker, S. Laplace, and F. Le Diberder. Eur. Phys. J. C **21**, 225 (2001). `hep-ph/0104062`.

[92] A. Hocker, H. Lacker, S. Laplace, and F. Le Diberder (2001). `hep-ph/0112295`.

[93] J. P. Alexander *et al.* (CLEO). Phys. Rev. Lett. **77**, 5000 (1996).

[94] B. H. Behrens *et al.* (CLEO). Phys. Rev. D **61**, 052001 (2000). `hep-ex/9905056`.

[95] R. Barate *et al.* (ALEPH). Eur. Phys. J. C **6**, 555 (1999).

[96] M. Acciarri *et al.* (L3). Phys. Lett. B **436**, 174 (1998).

[97] P. Abreu *et al.* (DELPHI). Phys. Lett. B **478**, 14 (2000). `hep-ex/0105054`.

[98] G. Abbiendi *et al.* (OPAL). Eur. Phys. J. C **21**, 399 (2001). `hep-ex/0107016`.

[99] C. W. Bauer, Z. Ligeti, and M. Luke (2001). `hep-ph/0111387`.

[100] R. A. Briere *et al.* CLNS-01-1742.